Technische Universität München
Institut für Energietechnik

Lehrstuhl für Thermodynamik

Influence of the Injector Geometry on Mixing and Lift-Off of Premixed Jet Flames in Hot Cross Flow

Michael Kolb

Vollständiger Abdruck der von der Fakultät für Maschinenwesen der Technischen Universität München zur Erlangung des akademischen Grades eines

DOKTOR – INGENIEURS

genehmigten Dissertation.

Vorsitzender:
Univ.-Prof. Dr.-Ing. Spliethoff
Prüfer der Dissertation:
1. Univ.-Prof. Dr.-Ing. Thomas Sattelmayer
2. Univ.-Prof. Dr.-Ing. Manfred Aigner

Die Dissertation wurde am 29.04.2015 bei der Technischen Universität München eingereicht und durch die Fakultät für Maschinenwesen am 09.02.2016 angenommen.

Preface

This thesis was produced during my time as research assistant at the Chair of Thermodynamics at the Technical University of Munich. The work was funded by General Electric, Power & Water.

My special thanks goes to Professor Thomas Sattelmayer for the supervision of my thesis. Additionally, I would like to thank him for his trust and the scientific discussions.

I also want to thank Professor Aigner for being my second examiner and Professor Spliethoff for being the chair of the examining committee.

I thank my colleagues for the scientific assistance and the friendly atmosphere at the chair. I will cherish memories of my long term office spouse Denise Ahrens. A special thanks also to the coworkers Stefan Bauer, Balbina Hampel, Vera Hoferichter, Kathrin Johé, Rene Quist, Mathias Utschick and Johannes Weinzierl for enhancing of my scientific work through our discussions. I particularly want to thank Rohit Kulkarni, because one of our discussions led to the essential idea for the lift-off model. Senior engineer Christoph Hirsch helped through various discussions to further develop these ideas. Worth mentioning is the support I received from the chair's administration employees Mrs. Bassett, Mrs. Hirsch and Mrs. Schulz-Reichwald to navigate the university's bureaucracy.

I also want to thank the electrical workshop with Mr. Strobl and Mr. Schleußner as well as the mechanical workshop with Mr. Giel, Mr. Hümmer, Mr. Dorrer, Mr. Wimmer and the apprentices who contributed significantly to the building and maintenance of the experimental setup. I also would like to thank the students and research assistants for their commitment and active support in alphabetical order: Andreas Bauer, Peter Brüderle, Julien Brunel, Andreas Dinzinger, Vera Hoferichter, Babak Mohajer, Mathias Möller, Peter Müller, Cristina Jose Oliveira, Tobias Petersen, Sebastian Pletzer, Matthew Reno, Moritz Rödel, Nizar Ben Salah, Johannes Schäfer, Pierre Schuman, Michael Steinmetz, Andreas Velte, Martin Wolff und Ariel Yaniv. Their work has helped with the development of parts of this work.

Particularly noteworthy is also the industry partner General Electric, Power & Water, who financed the doctorate period. Especially the cooperation with Hasan Karim, Mark Hadley and Sven Bethke was very fruitful and fun.

Finally, I would like to thank my family with all my heart for many years of support.

Garching, 26.02.2016 Michael Kolb

Zusammenfassung

Im Bereich der stationären Gasturbinen mit einstufiger Verbrennung sind magere Vormischflammen Stand der Technik, um niedrige Abgasemissionen zu erzielen. Der Einsatz von vorgemischten Jets in mehrstufigen Verbrennungsprozessen ist vielversprechend, um die Stickoxidemissionen weiter zu senken und das Teillastverhalten der Gasturbinen zu verbessern. In dieser Arbeit werden die Einmischung und die Abhebehöhe von Jets in Cross Flow experimentell untersucht. Die Einmischung wird durch Variation der Jet Düsengeometrie optimiert und mit Korrelationen beschrieben. Die Einflussgrößen der Abhebehöhe der Jetflamme werden mit Hilfe einer Parameterstudie ermittelt. Abschließend wird ein neues Modell entwickelt, das die Abhebehöhe von Jetflammen in einer heißen Querströmung vorhersagen kann.

Abstract

Lean premixed single-stage combustion is state of the art for low pollution combustion in heavy-duty gas turbines with gaseous fuels. The application of premixed jets in multi-stage combustion is a promising approach to lower nitric oxide emissions and to enhance turn-down ratio. In this work mixing and jet flame lift-off heights are investigated experimentally. Mixing is optimized by varying jet nozzle geometries and described with correlations. A parameter study is conducted to identify the influencing variables of flame lift-off. Finally, a new model is developed to predict the lift-off height of premixed jet flames in hot cross flow.

Contents

List of Figures

List of Tables

Nomenclature

Latin Letters

a	Thermal diffusivity	$[m^2/s]$
a_{ell}	Ellipse semi-major axis	[m]
A	Model constant	[-]
A_{circle}	Area of circle	$[m^2]$
A_{ell}	Area of ellipse	$[m^2]$
A_{fl}	Flame surface area	$[m^2]$
A_l	Laminar flame surface area	$[m^2]$
$A_{fl,min}$	Minimum flame surface area	$[m^2]$
$A_{fl,norm}$	Normalized flame surface area	$[m^2]$
$A_{fl,pro}$	Projected flame area	$[m^2]$
A_t	Mean turbulent flame area	$[m^2]$
A_x	Cross section of cross flow	$[m^2]$
b	Model constant	[-]
b_{ell}	Ellipse semi-minor axis	[m]
B_c	Model constant	[-]
B	Drag-entrainment coefficient	[-]
C	Model constant	[-]
C_D	Drag coefficient	[-]
$C_{D,solid}$	Drag coefficient of solid body	[-]
C_{uu}	Eddy size correlation	[-]
c_{ej}	Entrainment coefficient	[-]
c_p	Specific thermal capacity	[J/kg K]
d_1	Diameter at end of potential core	[m]
d_c	Mean width of jet	[m]
d_P	Diameter of seeding particle	[m]
D_j	Jet diameter	[m]
f	Jet mixture fraction	[-]

g	Model constant	[-]
h_j	Enthalpy of jet fluid	[J/kg]
h_{mix}	Enthalpy of mixture	[J/kg]
h_x	Enthalpy of cross flow fluid	[J/kg]
h_0	Width of jet nozzle	[m]
$h_{al,ign}$	Auto ignition length	[m]
I	Intensity	[-]
I_{ref}	Reference intensity	[-]
$\dot{I}$	Jet momentum	[kg m/s^2]
J	Momentum flux ratio	[-]
J_ϕ	Reacting momentum flux ratio	[-]
K	Model konstant	[-]
l_{min}	Minimal air requirements	[-]
l_{PC}	Length of potential core	[m]
$l_{PC,0}$	Reference length of potential core	[m]
l_η	Kolmogorov length scale	[m]
l_t	Integral length scale	[m]
LO	Lift-off height	[-]
$\dot{m}$	Mass flow	[kg/s]
$\dot{m}_1$	Mass flow at end of potential core	[kg/s]
$\dot{m}_j$	Mass flow of jet	[kg/s]
$\dot{m}_x$	Mass flow of cross flow	[kg/s]
$\dot{m}_{reac}$	Reacting mass flow	[kg/s]
p	Pressure	[bar]
p_{exp}	Pressure in experiment	[bar]
p_{eng}	Pressure in engine	[bar]
r	Radial coordinate	[m]
r_0	Outer radius of jet shear region	[m]
r_{fl}	Flame radius	[m]
r_ϕ	Momentum flux scaling factor	[-]
R_j	Velocity ratio	[-]
s	Perimeter factor	[-]
$\bar{S}$	Mean shear rate	[m/s^2]
$\bar{S}_{ext}$	Extended mean shear rate	[m/s^2]
S_l	Laminar flame speed	[m/s]
$S_{l,norm}$	Normalized laminar flame speed	[m/s]

$S_{l,min}$	Minimum laminar flame speed	[m/s]
S_t	Turbulent flame speed	[m/s]
$t_{l_{PC}}$	Time to reach end of potential core	[s]
T_0	Temperature of reactants	[K]
T_{ref}	Reference temperature	[K]
T_1	Temporary Temperature	[K]
T_{ad}	Adiabatic flame temperature	[K]
T_∞	Ambient temperature	[K]
T_j	Temperature of Jet	[K]
T_n	Normalized temperature	[-]
T_x	Temperature cross flow	[K]
u	Velocity	[m/s]
u, v, w	Velocities in x,y,z directions	[m/s]
$\bar{u}$	Mean velocity	[m/s]
u_1	Velocity at end of potential core	[m/s]
u_c	Velocity on centerline	[m/s]
u_j	Velocity jet	[m/s]
u_{prod}	Velocity of products	[m/s]
u_η	Velocity of Kolmogorov scales	[m/s]
u_t'	Velocity fluctuation	[m/s]
u_x	Velocity of cross flow	[m/s]
U_{circ}	Perimeter of a circle	[m]
U_{ell}	Perimeter of an ellipse	[m]
v_{min}	Minimal amount of exhaust	[-]
$v_{min,dry}$	Minimal amount of dry exhaust	[-]
w_0	Width of jet at nozzle	[m]
w_1	Width of jet at end of potential core	[m]
x,y,z	Cartesian coordinates	[m]

Greek Letters

α_1	Angle of inner shear layer	[°]
δ_l	Laminar flame thickness	[m]
ϵ	Dissipation rate	[m^2/s^3]
η_F	Dynamic viscosity of flow	[Ns/m^2]
η, ξ, ζ	Coordinates of jet trajectory	[m]

ϕ	Equivalence ratio	[-]
ϕ_{j}	Equivalence ratio of jet	[-]
$\phi_{0.66}$	Equivalence ratio for 15% O_2 in exhaust	[-]
ν	Kinematic viscosity	[m^2/s]
ν_{j}	Kinematic viscosity of jet fluid	[m^2/s]
ν_{t}	Turbulent viscosity	[m^2/s]
ρ_{prod}	Density of products	[kg/m^3]
ρ_{P}	Density of seeding particle	[kg/m^3]
ρ_{reac}	Density of reactants	[kg/m^3]
ρ_{ref}	Reference density	[kg/m^3]
ρ_{j}	Density of jet	[kg/m^3]
ρ_{x}	Density of cross flow	[kg/m^3]
$\bar{\tau}$	Mean shear stress tensor	[N/m^2]
τ_{c}	Chemical timescale	[s]
τ_{F}	Fluid timescale	[s]
τ_{ign}	Ignition delay	[s]
$\tau_{\mathrm{ign,eng}}$	Ignition delay in engine	[s]
$\tau_{\mathrm{ign,exp}}$	Ignition delay in experiment	[s]
τ_{P}	Particle timescale	[s]
τ_{t}	Turbulent timescale	[s]
τ_{η}	Kolmogorov timescale	[s]
$\bar{\dot{\omega}}$	Mean reaction rate	[kg/m^3s]
Ψ	Characteristic value	[-]

Dimensionless Numbers

$\mathrm{Da}_{\mathrm{ign}}$	Ignition delay Damköhler number
Da_{t}	Turbulent Damköhler number
Ka	Karloviz number
Ka_{j}	Jet Karloviz number
$\mathrm{Ka}_{\mathrm{mix}}$	Mixture Karloviz number
Pr	Prandtl number
Re	Reynolds number
Re_{j}	Jet Reynolds number
Re_{t}	Turbulent Reynolds number
Sc_{t}	Turbulent Schmidt number
St	Stokes number

St_t	Stokes number for macro scales
St_η	Stokes number for Kolmogorov scales

Acronyms and abbreviations

AFS	Axial fuel staging
BG	Background
CO	Carbon monoxide
CVP	Counter rotating vortex pair
GE	General Electric
MRMF	Most reactive mixture fraction
NO	Nitrogen oxide
NG	Natural gas
LES	Large eddy simulation
LS	Laser sheet
P	Circular nozzle
RANS	Reynolds-averaged Navier-Stokes
S1	Slot nozzle aligned parallel to the cross flow
S2	Slot nozzle aligned perpendicular to the cross flow
T1	Triangle nozzle with an edge pointing upstream
T2	Triangle nozzle with an edge pointing downstream
UHC	Unburnt hydrocarbon

1 Introduction

It is expected that the world's power demand will further increase in the coming decades. In spite of strong efforts to increase the share of power from renewable sources projections show that fossil fuel based power generation will continue to be the back bone of electrical power systems. In this scenario the cost of fossil fuel based power is anticipated to rise due to the decrease of fossil fuel reserves as well as due to carbon taxes which will be introduced to control global warming. A further increase of the efficiency of gas turbines addresses both challenges as it reduces the fuel consumption as well as the the carbon emission.

Gas turbine cycle efficiency directly relates to the turbine inlet temperature which is closely connected with the adiabatic flame temperature of the combustor. In lean premixed combustion the formation rate of nitrogen oxide (NO) which is the main pollutant component in gas turbine exhaust depends strongly on adiabatic flame temperature. For a fixed combustor design an increase of turbine inlet temperature will therefore be accompanied with an over proportional rise of the NO emission of the combustor. Additionally to the adiabatic flame temperature, the NO emissions depend on the residence time of the burnt gas at high temperature between the main flame zone and the turbine inlet which is called post-flame residence time. A reduction of the combustor length and of post-flame residence time could be used to counterbalance the increased NO formation rate due to higher turbine inlet temperature. This is reasonable since the time required for carbon monoxide(CO)-equilibrium is also reduced with increasing temperature and therefore the CO burn-out is not affected. However to achieve the required operation window of the engine combustor residence times must also be sufficient for CO burnout at part load operation where combustor temperature is low.

Axial fuel staging provides a way out of this dilemma. The first stage has a sufficient residence time for burnout in low part load operation. The first stage

nominal flame temperature is chosen such that post flame NO formation will be acceptable in spite of the higher residence time. At full load operation the second combustion stage raises the hot gas temperature from the first stage level to the required turbine inlet temperature. With a much shorter post flame residence time of the second stage the NO emission due to the high temperature can be controlled. Like this the operational flexibility as well as the cycle efficiency can be increased while maintaining low pollutant emissions.

In 1978 S.M. DeCorso [24] applied for a patent for a gas turbine combustion system with premixed axial fuel staging using a diffusion flame pilot stage and a multitude of premixed jet in cross flow injections downstream.

In their 1994 issued patent Toon et al. [114] describe axially staged combustion which was subsequently realized in the Rolls Royce Trent industrial gas turbine. The combustor has three combustion stages. The first stage is similar to swirl combustors with an integrated pilot and main stage while the second and third stages are realized as jets in cross flow. As pointed out in Lechner et al. [66] the second and third stages can burn lean mixtures beyond the blow-off limit to enhance the NO control.

The concept of premixed axial fuel staging has been outlined in detail in the 1990 patent publication by N. D. Joshi and F. E. Moreno [53]. They show the network of a sequence of stirred reactor and plug flow reactors to approximate the combustion process.

In the 2011 issued patent W. Cai [18] presents a general concept of axially staged premixed combustion and shows qualitative NO_x formation curves for different axial stage locations. He points out the importance of providing premixed reactants at the staged injection points: "The inventor has discovered that there must be adequate fuel-air mixing at each axial stage of a multi-stage axial system, otherwise the amount of NOx generated can actually be greater than the NOx generated by a standard full burn in the head end system with no axial staging."

The first realization of axial staging in heavy-duty gas turbines was presented by General Electric (GE) with the axial fuel staging system (AFS) in the 7HA.01 and 7HA.02 gas turbines [42, 116]. Higher efficiencies and turn-down ratios at

constant NO and CO emissions are reported.

Apart from the above patent publications the current literature search has not yielded further details on these particular combustion systems. Though the body of literature on non-premixed fuel jets and non-reacting jets in cross flow is extensive[1] publications on staged combustion using premixed jets in cross flow are also scarce and only date from recent years.

Galeazzo et al. [30–33] published studies on a premixed jet in hot cross flow. They were able to stabilize a lifted flame in the test rig and to model the flame using LES with a presumed PDF model.

A similar experiment was set up by Lamont et al. [62–64]. They found out that it is possible to get higher turbine inlet temperatures while maintaining the emissions of NO_x, UHC and CO constant at elevated pressure. Aida and Adachi [3, 6, 7] also showed a NO reduction potential in staged combustion for small scale gas turbines. Ahrens et al. [4, 5] discussed the NO reduction potential of staged combustion using kinetic modeling.

Summarizing the previous findings it can be stated that though the concept of axial fuel staging appears strikingly simple its transformation into combustor technology faces some difficulties before the benefit regarding the emissions of the second stage is realized. The reason is that the amount of air admitted in the second stage is smaller than that required for the second stage fuel flow rate because a part of the combustion air is already delivered with the first stage hot gas flow. Premixing of secondary fuel and secondary air alone gives a significantly richer mixture than that required for the turbine inlet temperature and would cause higher NO-formation rates. Therefore the mixing between the first stage flow and the second stage mixture prior to the onset of reaction plays a crucial role in the design of axial staged combustion.

1.1 Thesis Overview

The goal of this thesis is to provide design models for the mixing process and the flame stabilization in the second stage of combustors with fuel staging. To

[1] Survey in chapter 2.4.1

develop the models an experiment was designed to realize a premixed reacting jet in hot cross flow on laboratory scale. Measurements of velocity, mixture and emissions were performed for a range of operating conditions similar to engine conditions. The data obtained is on the one hand used to develop a model for the mixing process depending on the jet nozzle geometry. On the other hand a model which predicts the lift-off height of jet flames due auto-ignition and flame propagation is derived.

The basics of turbulent flows, combustion regimes, flame propagation, flame lift-off, and emission formation are introduced in chapter 2. In chapter 3, scaling and design of the combustion experiment are shown. Chapter 4 outlines the applied measurement methods. The results and discussion section is divided into two parts. Chapter 5 is focused on the influence of jet nozzle geometries on mixing and reaction. After presenting the details of non-reacting experimental results, turbulent free jet theory is used to derive a model for the velocity and mixing field close to the jet nozzle for jets in cross flow. From the comparison of non-reacting and reacting results it is presented how NO emissions correlate with non-reacting mixture measurements. The analysis of the experimental data in chapter 6 reveals that for the investigated experiment existing lift-off theories do not apply. Therefore, a lift-off model of reacting premixed jets in hot cross flow is developed. The proposed model combines existing lift-off theory from literature based on flame propagation or auto-ignition to describe premixed jets in vitiated cross flow. Finally, the findings of the thesis are summarized in chapter 7.

2 Fundamentals

2.1 Turbulence

The flow in gas turbine combustors is highly turbulent. The high intensity of turbulence is needed to provide the required fuel-air mixing rates and the reaction rate densities necessary to achieve complete lean premixed combustion of hundreds of megawatts fuel power within residence times of the order of 10-30ms.

The main characteristic of turbulent flow is its three dimensional, unsteady vortical structure which is able to distribute enthalpy, species, and momentum very efficiently in space. The high shear rates that accompany the vortex motion create interfacial area between unmixed quantities and increase their spatial gradients which enhances molecular mixing.

The largest vortical structures of turbulence are generated by the non-linear growth of quasi-inviscid shear layer instabilities. As they create the largest fluctuations of velocity seen in a time resolved velocity measurement signal, a characteristic velocity scale u'_t for them can be defined by the root mean square (RMS) value:

$$u'_t(t,x) = u(t,x) - \bar{u}(x) \tag{2.1}$$

$$\overline{u'^2_t}(x) = \frac{1}{T}\int_0^T (u'_t(x,t))^2\,dt \tag{2.2}$$

$$u'_t(x) = \sqrt{\overline{u'^2_t}}. \tag{2.3}$$

In eqn. 2.1 $u(t,x)$ is the local momentary velocity and $\bar{u}(x)$ is the local time

mean velocity given by:

$$\bar{u}(x) = \frac{1}{T}\int_0^T u(t,x)\,dt. \tag{2.4}$$

The size of the large turbulent vortices can be estimated using an integral length scale $l_t(x)$ based on the correlation between the velocity fluctuations in space:

$$l_t(x) = \int_0^\infty C_{uu}(x,\Delta x)\,d(\Delta x) \tag{2.5}$$

$$C_{uu} = \frac{\overline{u'(x)\cdot u'(x+\Delta x)}}{\sqrt{\overline{u_t'^2}(x)}\cdot\sqrt{\overline{u_t'^2}(x+\Delta x)}}. \tag{2.6}$$

In eqn 2.6 the overline indicates time averaging as introduced in eqn 2.4.

These large vortices with a characteristic velocity scale of $u_t'(x)$ and characteristic size of $l_t(x)$ become unstable themselves and break up into smaller vortices. In a process of quasi-inviscid vortex stretching and further break up called the vortex cascade the kinetic energy of the larger vortices is transferred to smaller vortices [112]. The transferred kinetic energy per unit mass is called the dissipation rate ε. Based on the observation that the average lifetime of a largest vortex class is given by the turbulent timescale:

$$\tau_t = \frac{l_t}{u_t'}. \tag{2.7}$$

The dissipation rate is estimated by:

$$\varepsilon = \frac{du_t'^2}{dt} \approx \frac{u_t'^2}{\tau_t} = \frac{u_t'^3}{l_t} = \frac{u_n'^3}{l_n}. \tag{2.8}$$

Cornerstone of this theory is the so called Taylor hypothesis which states that this dissipation rate is constant for all classes in the vortex cascade. The velocity and length scales: $u_n'^3$ and l_n refer to the n-th class of smaller vortices of the vortex cascade. The quasi-inviscid character of turbulence is seen from the

fact that the estimate of the dissipation rate does not involve molecular viscosity. As the vortices become smaller the interfacial area generated increases with the spatial gradients until molecular diffusion becomes strong enough to dissipate the kinetic energy of the vortex motion into internal energy of the fluid. To estimate the size of these vortices we can assume that the vortex cascade is inviscid until the smallest vortex scales are reached. The dissipation rate must equal the product of the molecular viscosity ν and the square of the velocity gradient created by this vortex class:

$$\varepsilon = \frac{u_\eta'^3}{l_\eta} = 2\nu\left(\frac{du_\eta'}{dr}\right)^2 \approx \nu\frac{u_\eta'^2}{l_\eta^2}. \tag{2.9}$$

This order of magnitude estimate gives the classical scaling rules to calculate the smallest scales of turbulence u_η, l_η from u_t' and l_t. The smallest ones are called Kolmogorov scales and the largest ones integral scales. Since the macro scales determine the vortex cascade they are used to calculate the characteristic measure for the extent of the vortex cascade, the turbulent Reynolds Number Re_t, which is proportional the system Re number with the characteristic length D_j:

$$Re_t = \frac{u_t' l_t}{\nu} \sim Re = \frac{\bar{u} D_j}{\nu}. \tag{2.10}$$

Figure 2.1 demonstrates the influence of Re_t on the structure of a turbulent jet in cross flow. As the Re_t is increased smaller structures appear whereas the large scale structure of the flow remains the same:

$$\frac{l_\eta}{l_t} = Re_t^{-3/4} \tag{2.11}$$

$$\frac{u_\eta}{u_t'} = Re_t^{-1/4}. \tag{2.12}$$

Furthermore, the Kolmogorov timescale τ_η can be determined:

$$\tau_\eta = \frac{l_\eta}{u_\eta}. \tag{2.13}$$

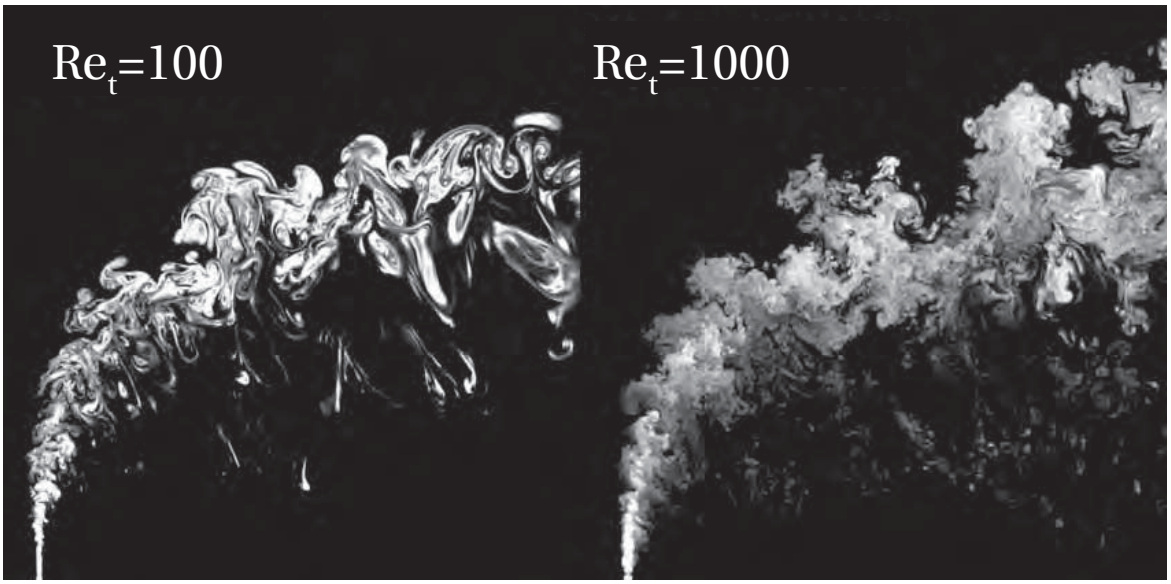

Figure 2.1: Mixed-fluid concentration in the symmetry plane of a jet in cross flow with different turbulent Reynolds numbers. Figure taken from [102].

Equations 2.11 to 2.13 show that Re_t is the parameter that describes the connection between the Kolmogorov scales and the integral length scales. With respect to premixed combustion theory outlined in section 2.2.3, Re_t is the relevant structure parameter of the turbulence for the premixed flame regime.

2.2 Flame Propagation

Flame propagation describes the motion of a reaction zone through a mixture of oxidizer and fuel. For the design of technical combustion applications the flame propagation speed is an important design parameter to stabilize the flame and avoid flashbacks or blow-offs. In chapter 6 the flame propagation speed is a crucial parameter to determine the flame lift-off height and, therefore, the different types of flame propagation are presented in the next sections. The propagation of a flame in a laminar flow is well understood and trustworthy models exist. Flame propagation in turbulent flows is more complex. Most models for turbulent flame speeds build up on laminar flame speed models. An appropriate correlation for turbulent flame speeds for flow conditions similar to the ones within this study is presented in section 2.1. Additionally, auto-ignition can control the flame propagation under certain condi-

tions. As the laminar flame propagation is the basis for most turbulent flame speed theories it is presented first. Secondly, the transition from laminar flame propagation to auto-ignition will be discussed. Afterward, models for turbulent flame speeds are presented.

2.2.1 Laminar Flame Speed

The laminar flame speed S_l is defined as the propagation velocity of a reaction zone in a laminar flow. The flame speed depends on the reactants properties. The most important properties are the type of fuel, oxidizer, pressure, temperature, diffusivity and fuel-oxidizer ratio.

Schmid [100] showed that the laminar flame speed S_l is proportional to mean reaction rate $\bar{\dot{\omega}}$, thermal diffusivity a and reactant density ρ_{reac}:

$$S_l \sim \left(a \frac{\bar{\dot{\omega}}}{\rho_{reac}} \right)^{\frac{1}{2}}. \tag{2.14}$$

Equation 2.14 shows the dependency of the laminar flame speed on the mean reaction rate which allows the usage of the laminar flame speed as a measure for the chemical timescale τ_c:

$$\tau_c = \frac{a}{S_l^2}. \tag{2.15}$$

Therefore, the laminar flame speed is able to characterize the reactivity of a fluid and is used in section 6.5 to define chemical time scales of investigated flames. To calculate the chemical time scales the laminar flame speeds have to be determined. For the specific case of premixed methane-air flames a correlation from Peters [84, 85] for the laminar flame speed exists:

$$S_l = 0.22176 \left[\frac{m}{s} \right] + \left(\frac{1}{1 + \frac{17.16}{\phi}} \right)^{0.565} e^{\frac{6444.27[K]}{T_n}} \frac{T_0}{T_n} \left(\frac{T_1 - T_n}{T_1 - T_0} \right)^{2.516} \left[\frac{m}{s} \right] \tag{2.16}$$

$$T_n = \frac{23873[K]}{\log_{10} \frac{3155[bar]}{p}} \tag{2.17}$$

$$T_1 = 0.627 T_0 + 1270.15 - 2449\phi + 6776\phi^2 - 3556\phi^3. \tag{2.18}$$

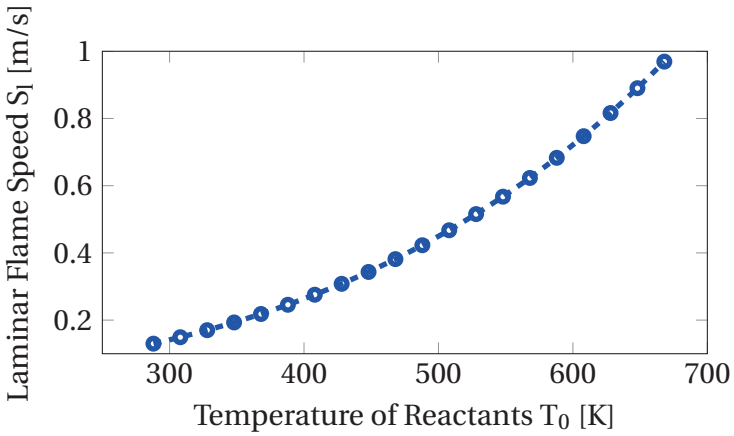

Figure 2.2: Dependency of laminar flame speed S_l on temperature of the reactants, with pressure p = 1bar and equivalence ratio $\phi = 0.66$.

The correlation is an empirical fit and includes the equivalence ratio ϕ, the temperature of the reactants T_0, and the pressure of the system p. Two temporary temperatures T_n and T_1 are calculated as inputs to evaluate the laminar flame speed S_l for methane-air mixtures. Figures 2.2, 2.3 and 2.4 show the dependency of the laminar flame speed on the parameters mentioned at the beginning of this section. A validation of the correlation from Peters was performed with a numerical simulation of an one-dimensional premixed laminar flame using the software Cantera [35] and the reaction mechanism GRI 3.0 [103]. The comparison of the laminar flame speeds from the simulations and Peters' correlation is shown in figure 2.5. The agreement of the two results is good and therefore Peters' correlation is used for the calculation of the laminar flame speed within this thesis.

The laminar flame speed scales exponentially with the preheating temperature, see figure 2.2. High temperatures reduce the time to preheat the reactants before combustion and, furthermore, increase the adiabatic flame temperature which increases the reaction rate. In figure 2.3 it is shown that the increasing pressure reduces the laminar flame speed. The increase of the reaction rate at high pressure also accelerates the laminar flame speed, but the decrease of the thermal diffusivity a dominates and decelerates the propagation. The influence of the equivalence ratio ϕ is shown in figure 2.4. The laminar flame speed has a maximum for $\phi = 1.1$. For lower equivalence ratios the thermal ballast of excess air decelerates the flame and for higher equivalence ratios the lack of oxidizer decreases the flame velocity.

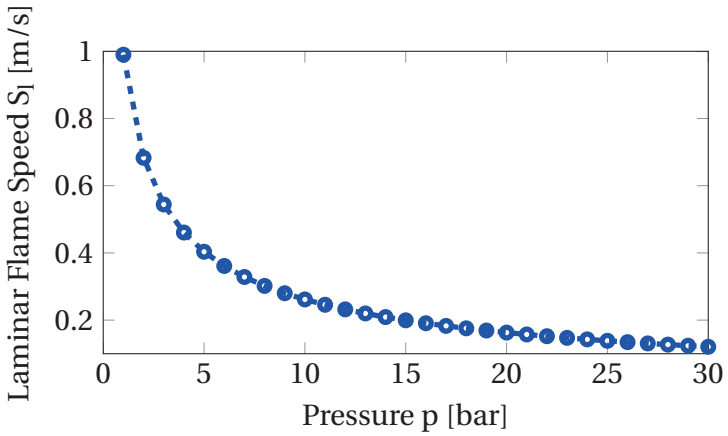

Figure 2.3: Dependency of laminar flame speed S_l on pressure p, with temperature $T_0 = 673K$ and equivalence ratio $\phi = 0.66$.

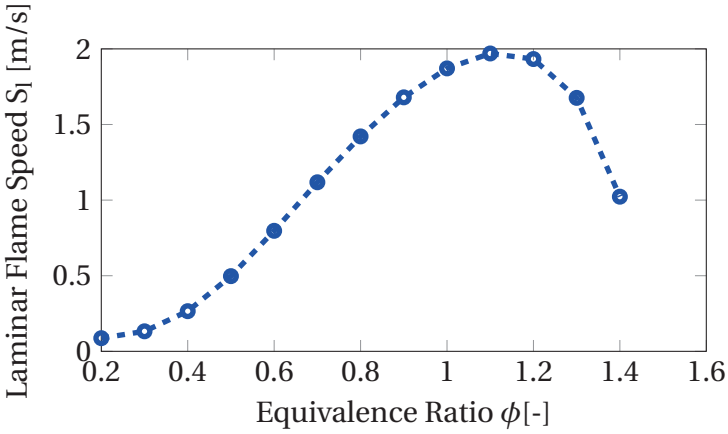

Figure 2.4: Dependency of laminar flame speed S_l on equivalence ratio ϕ, with pressure p = 1bar and temperature $T_0 = 673K$.

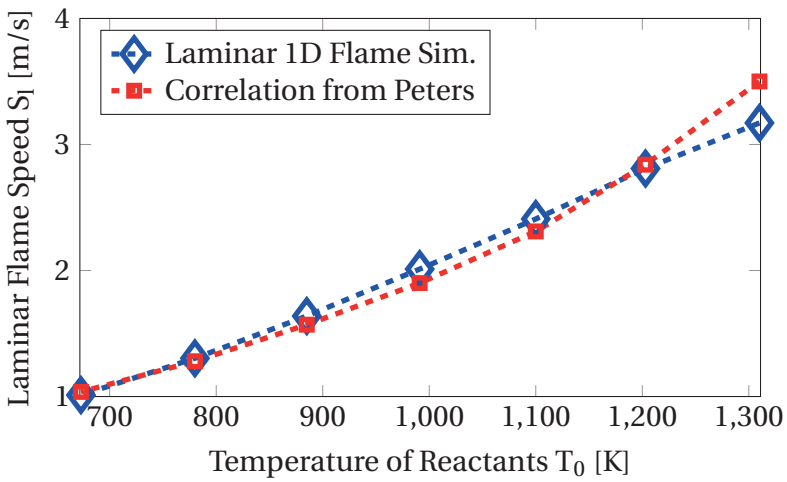

Figure 2.5: Laminar flame speeds calculated from Peters' empirical correlation [85] compared to free flame calculations using Cantera [35] with GRI3.0 [103].

For higher preheating temperatures (>1000K) the flame propagation is controlled by auto-ignition. Habisreuther and Galeazzo [40] used one-dimensional laminar premixed flame simulations to compare laminar flame propagation with the flame propagation of an auto-ignition controlled flame. They were able to identify a transition between a laminar flame propagation regime as presented above and an auto-ignition regime. If auto-ignition dominates the reaction rate increases drastically. They also found that the two regimes do not interact. Once the transition point is reached one or the other mechanism completely controls the flame propagation speed. It is important to notice that this is only true for one dimensional flames. In more complex flames the two regimes are likely to exist next to each other.

2.2.2 Auto-Ignition

Auto-ignition describes the formation of ignition kernels. In this thesis auto-ignition of a reactive mixture mixing with a hot exhaust gas is investigated.

If suitable conditions are present auto-ignition takes place after an ignition delay time τ_{ign} followed by a flame which propagates spherically for homogeneous mixtures. For several applications it is important to know this ignition delay time to design the engine or combustor. In the last years insight into the chemical reactions of auto-ignition was gained by experiments and simula-

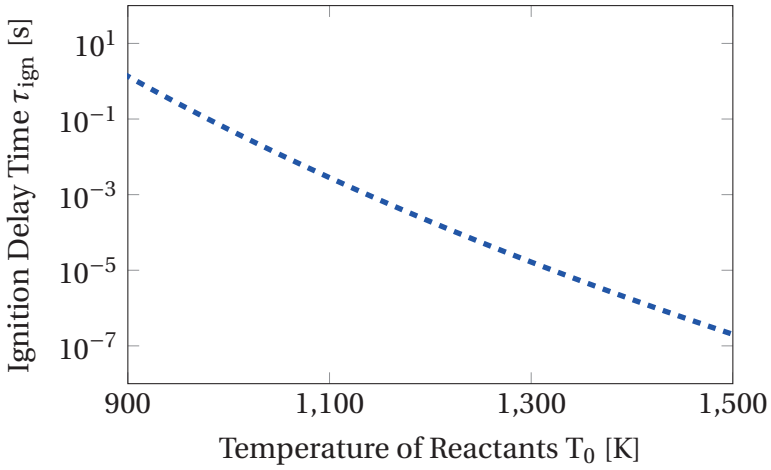

Figure 2.6: Ignition delay time of a stoichiometric methane-air mixture at atmospheric pressure calculated using Cantera [35] with GRI3.0 [103].

tions [11, 74, 75].

To obtain auto-ignition a minimum temperature is required. Below this temperature no auto-ignition occurs. Above this temperature the auto-ignition occurs after the ignition delay time τ_{ign}. Previous research found the minimum auto-ignition temperature to be about 873K [21, 105] for stoichiometric methane-air mixtures at atmospheric pressure. Figure 2.6 shows the ignition delay time for a stoichiometric methane-air mixture at atmospheric pressure for different initial reactants temperatures. There are also empirical expressions available in literature which correlate the temperature, pressure and equivalence ratio with ignition delay times, e.g. by Spadaccini and Colklet [106]. They found that the ignition delay time reduces exponentially with temperature while the pressure influence is almost linear. Furthermore, experiments showed that leaner mixtures have lower ignition delay times, but compared to the temperature influence the effect is negligible [106].

Knowing the ignition delay time and the mean flow velocity $\bar{u}$ of a free jet, it is possible to calculate the distance from the nozzle until ignition occurs:

$$h_{al,ign} = \bar{u}\tau_{ign}. \tag{2.19}$$

This auto-ignition length $h_{al,ign}$ is applicable for homogeneous conditions only. For inhomogeneous conditions the ignition delay depends on the local air-fuel ratio. Recent publications on inhomogeneous auto-ignition showed that the ignition always occurs at the most reactive mixture fraction (MRMF)

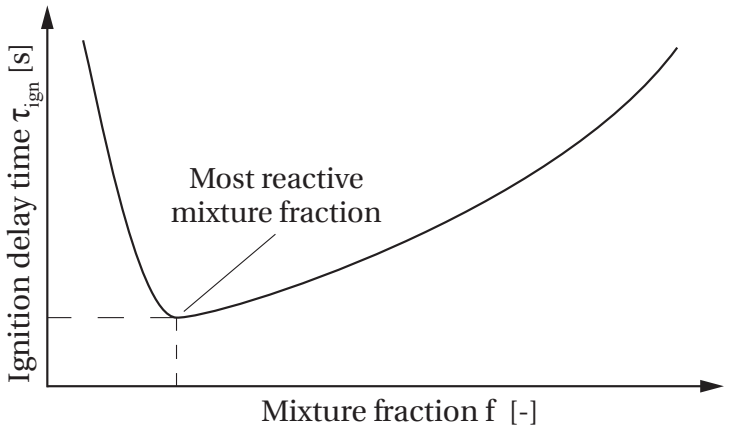

Figure 2.7: Scheme of the ignition delay for different fuel and air mixtures with a minimum at the most reactive mixture fraction (MRMF).

[27, 52, 60, 74, 75]. The MRMF is defined as the mixture fraction f of two or more fluids with the lowest ignition delay time τ_{ign}. Figure 2.7 shows the ignition delay times of mixture fractions of two flows with its minimum marked as the MRMF.

2.2.3 Turbulent Flame Speed

In most industrial applications and also in the set up investigated in this thesis the flow is turbulent. Flame propagation in turbulent flows is faster than the laminar flame speed due to the turbulent velocity fluctuations which increase the flame surface area. The turbulent vortices play an important role as they can interfere with the flame front. Schmid [100] gives a comprehensive explanation of different combustion regimes using the turbulent macro timescales τ_t, the Kolmogorov timescales τ_η, and the chemical timescales of the laminar flame τ_c. His theory is based on the work of Peters [83] on turbulent combustion regimes. Peters' classification of turbulent combustion regimes, shown in figure 2.8, is based on four parameters: the turbulent velocity fluctuation u'_t, the laminar flame speed S_l, the integral length scale l_t and the laminar flame thickness δ_L.

For flows where the chemical timescale is smaller than the Kolmogorov timescale, $\tau_c < \tau_\eta$, the vortices wrinkle the flame and increase the flame sur-

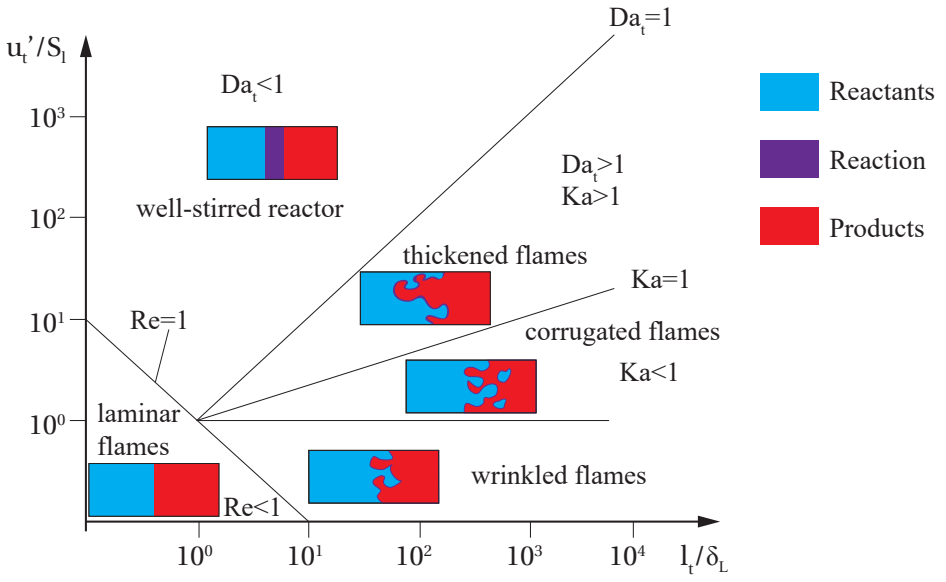

Figure 2.8: Flame regimes of premixed flames according to Peters [83].

face area, but within the flame thickness they do not influence the reaction. The wrinkling increases the flame propagation speed proportional to the increased flame surface area. In this regime the turbulent flame speed mainly depending on the velocity fluctuations:

$$\frac{S_t}{S_l} \sim \frac{u_t'}{S_l}. \tag{2.20}$$

Figure 2.9 shows a scheme of a laminar and a turbulent flame stabilized in a pipe. The mean surface of the turbulent flame has a higher propagation speed compared to the laminar flame. In the flame regime diagram, figure 2.8, this regime is called wrinkled flames. An extension to this regime are the corrugated flames. As the turbulent timescales decrease bales of reactants can penetrate the flame surface faster than the reaction can convert them. This penetration leads to an enlargement of the flame surface area. If the turbulent scales are further increased and the chemical timescale becomes bigger than the Kolmogorov timescale but stays smaller than the turbulent macro timescale, $\tau_\eta < \tau_c < \tau_t$, the large vortices wrinkle the flame while the smaller ones stir within the flame front and increase its thickness. This regime is called thickened flames. The last flame regime describes the conditions where the chemical timescale is larger than all turbulent timescales, $\tau_c > \tau_\eta$. In this case, vortices of all sizes contribute to the stirring within the flame front. The reaction process is dominated by the chemical timescale similar to a well-stirred

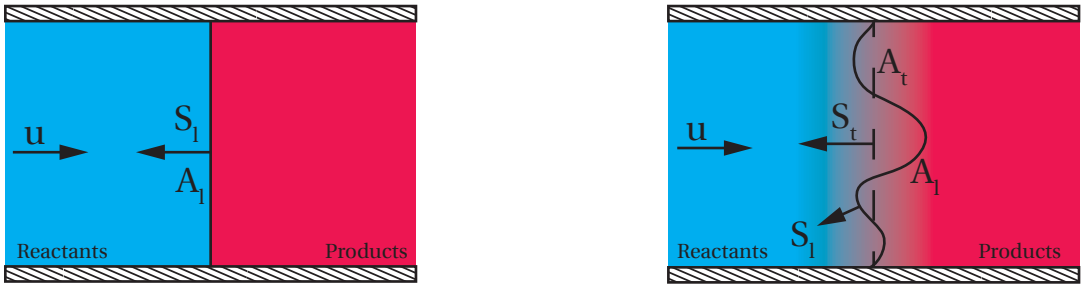

Figure 2.9: Left: Scheme of a laminar flame stabilized in a pipe. Right: Scheme of turbulent flame stabilized in a pipe.

reactor and the influence of the laminar flame speed increases [100]:

$$\frac{S_t}{S_l} \sim Re_t^{0.5}. \tag{2.21}$$

The dimensionless numbers turbulent Reynolds number Re_t, turbulent Damköhler number Da_t and Karlovitz number Ka are used to differentiate the combustion regimes. Re_t describes the relevant structure parameters of the flow for premixed combustion (section 2.1). Da_t sets the turbulent macro timescale τ_t and chemical timescale τ_c in relation:

$$Da_t = \frac{\tau_t}{\tau_c} = \frac{l_t S_l^2}{u_t' a}. \tag{2.22}$$

Turbulent Damköhler numbers smaller than unity characterize flame regimes where the reaction is limited by chemistry. For turbulent Damköhler numbers bigger than unity combustion is limited by turbulent mixing.

The Karlovitz number Ka compares the Kolmogorov timescale τ_η and the chemical timescale τ_c. The Karlovitz number is approximated using turbulent Reynolds and turbulent Damköhler numbers:

$$Ka = \frac{\tau_c}{\tau_\eta} \approx \sqrt{\frac{Re_t}{Da_t^2}} = \frac{u_t'^{1.5} a^{0.5}}{l_t^{0.5} S_l^2} \tag{2.23}$$

Details on the derivation can be found in literature [1, 85, 86]. The Karlovitz number becomes unity if the smallest vortices have the same size as the reaction zone. For the modeling in section 6.5 a jet Karlovitz number Ka_j is calculated based on the jet composition and a mixture Karlovitz number Ka_{mix} is calculated for the composition of a mixture of jet and cross flow material.

A correlation for the turbulent flame speed which is valid for all combustion regimes cannot be found in literature. The flames considered within this work are close to a Karlovitz number of unity. For this regime Andrews and Bradly derived a correlation for the turbulent flame speed depending on the Prandtl number Pr [10]:

$$S_t = S_l \left(\frac{u_t' l_t}{\nu} \mathrm{Pr} \right)^{0.5}. \tag{2.24}$$

This correlation will be used in section 6.5 to model the lift-off height.

An additional parameter which is important in this thesis is the ignition delay time τ_{ign}. As shown in section 2.2.2 it is the main parameter to describe auto-ignition. An ignition delay Damköhler number Da_{ign} is defined as the ratio of turbulent integral timescale τ_t and the ignition delay time τ_{ign}:

$$Da_{ign} = \frac{\tau_t}{\tau_{ign}} = \frac{l_t}{u_t' \tau_{ign}}. \tag{2.25}$$

The ignition delay Damköhler number characterizes the auto-ignition process and is independent of the chemical timescale τ_c.

2.3 Free Jets

A jet issuing from a nozzle into a very large space filled with stagnant fluid is called free jet. For free jets analytical solutions exist for laminar flows based on similarity theory. It is found that these can also be applied to turbulent jet flows if a turbulent viscosity ν_t is used [99]. Based on the comprehensive knowledge on free jets and the similarity to jets in cross flow, free jet theory is extended to analyze and model jets in cross flow in chapter 5.

2.3.1 Overview

Although a free jet is a flow with a simple topology it covers all turbulent phenomena: Shear layer instability with large scale structures, eddy break up and dissipation. As the shear layer instability governs the development of the near field of the jet, the radial flow profile and the turbulence at the nozzle exit have

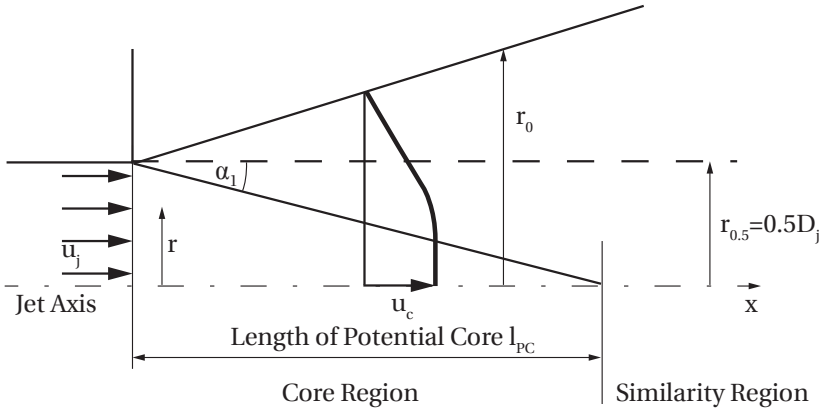

Figure 2.10: Scheme of a free jet. The jet comes from the left and enters a quiescent volume.

an influence on the length of the potential core region. This is known from hydrodynamic stability theory. For high Reynolds number nozzle flows typical of gas turbine combustor flows, however, the exponential growth of the instability into turbulence will dominate the potential core region such that the nozzle exit conditions are reduced to the effects of the nozzle geometry. This was also shown experimentally by many groups, e.g. Hussein et al. [51] and Papadopulus et al. [82]. Analytical models were presented and validated with experimental data, e.g. the Tollmien solution [113] as well as the Goertler solution [34].

The overall flow field of free jets can be divided into a core region close to the nozzle and a similarity region further downstream [89], see figure 2.10. The core region covers the jet from the nozzle exit to the end of the potential core. The potential core is defined as the flow region where the velocity or species concentration is equal to the conditions at the nozzle exit. The similarity region starts from the end of the potential core and has no limitation downstream. The velocities and concentration in the similarity region are known to be self-similar.

The core region close to the nozzle is not self-similar and highly dependent on the previously presented parameters velocity profile, nozzle shape, turbulent intensity and fluid density. In literature no general valid model for this region can be found.

2.3.2 Core Region

The main characterizing parameter of the core region is its length which is determined by the length of the potential core. Various groups investigated turbulent annular shear layers experimentally, e.g. [2, 89]. Also analytical solutions for the core region were proposed, e.g. [8, 107]. Despite the research efforts no universal model for the length or spread of the potential core region is found in literature. Therefore, the characterizing parameters, especially the length of the potential core, are estimated using correlations and experimental results. For a round jet issuing from a nozzle with a top-hat velocity profile, the length of the potential core is reported to be $l_{PC} \approx 6.5\,D_j$ [89] for the velocity field. For potential cores determined by the jet concentration the length is reported to be shorter [98].

For non-circular jets, e.g. slot nozzles, the length of the core region is estimated based on the angle of the inner shear layer, see figure 2.10 for the definition of the angle. For the velocity field the angle is reported to be about $\alpha_1 \approx 4.5°$ [2]. For the concentration field the length of the potential core is reported to be shorter and, therefore, the angle must be larger $\alpha_1 > 4.5°$. Using α_1 the length of the potential core is estimated based on the width h_0 of the jet nozzle. For a circular jet the width is equal to the diameter; for a rectangular jet, the width corresponds to the shorter side. The model assumes that the shear layers do not interfere with each other. The length of the potential core is calculated as:

$$l_{PC} = \frac{0.5 h_0}{\tan \alpha_1}. \tag{2.26}$$

The angle α_1 depends on the velocity and concentration profiles, densities of jet and ambient air as well as the turbulent intensities.

2.3.3 Similarity Region

The similarity region of free jets covers the region after the potential core. It is called similarity region as it is modeled using similarity theory. Based on the conservation equations models are deduced which describe the velocity at every point in the similarity region. Assuming similar species and momentum transfer as proposed by the Reynolds analogy, the species concentrations can

also be described. To derive the model proposed by Schlichting [99], it is assumed that the momentum in axial direction is constant, that the momentum in radial direction is zero, and that the pressure is constant. The conservation equations for mass and axial momentum remain:

$$u\frac{\partial u}{\partial x} + v\frac{\partial u}{\partial r} = \nu\frac{1}{r}\frac{\partial}{\partial r}\left(r\frac{\partial u}{\partial r}\right) \tag{2.27}$$

$$\frac{\partial u}{\partial x} + \frac{\partial v}{\partial r} + \frac{v}{r} = 0. \tag{2.28}$$

Assuming inertia and friction of the same order in equation 2.27, laminar flow, top-hat velocity profile at the nozzle, and no radial velocity component solutions for the differential equation have been derived by different authors. Here, the solution of Tollmien [113] is used:

$$\frac{u(r,x)}{u_0} = \frac{3}{32}Re\frac{D_j}{x}\left(1+\frac{\xi^2}{4}\right)^{-2} \tag{2.29}$$

$$\xi = 0.2165 \cdot Re\frac{r}{x}. \tag{2.30}$$

The Reynolds number Re depends on the conditions at the nozzle:

$$Re = \frac{u_j D_j}{\nu}. \tag{2.31}$$

If only the velocity on the center line u_c of the jet is of interest, equation 2.29 simplifies to:

$$\frac{u(r=0,x)}{u_j} = \frac{u_c(x)}{u_j} = \frac{3}{32}Re\frac{D_j}{x}. \tag{2.32}$$

For turbulent jets with sufficient high Reynolds numbers the flow field becomes independent of the Reynolds number. Based on the eddy viscosity approach the molecular viscosity ν is replaced by a turbulent viscosity ν_t [99]. The turbulent viscosity for free jets is a function of the jet velocity, diameter, and a pre-factor.

$$\nu_t = 0.01426 u_j D_j. \tag{2.33}$$

The pre-factor is determined from experiments, e.g. [47]. This turbulent viscosity is only applicable for the velocity field, for the concentration distribution the turbulent viscosity has to be adjusted using the turbulent Schmidt

number $Sc_t \approx 0.737$ which is also determined from experiments [47]. The turbulent viscosity for species transport is written as:

$$\nu_t = \frac{0.01425}{Sc_t} u_j D_j = 0.01934 u_j D_j. \tag{2.34}$$

Finally, the Reynolds number, which is determined with the turbulent viscosity, is inserted into equation 2.32 to get the velocity development on the center line for a turbulent free jet:

$$\frac{u_c(x)}{u_j} = \frac{3}{32} \frac{1}{0.01426} \frac{D_j}{x}. \tag{2.35}$$

The equation for the jet concentration on the center line is equal to equation 2.35, only the turbulent viscosity has to be adjusted using the turbulent Schmidt number Sc_t. It is important to notice that equation 2.35 is only valid in the similarity region, not the core region.

2.4 Flow Structure of Jets in Cross Flow

In the jet in cross flow configuration the ambient fluid (cross flow) is moving transversely to the jet flow direction. Jets in cross flow are present in many practical applications. This is why publications treating jets in cross flow are found as early as in the 1930s when Sutton tried to estimate the distribution of volcanic ash [110]. Bosanquet and Pearson investigated the soot distribution from power plant stacks [12]. Since then, there have been numerous publications on jets in cross flow for various applications. Recently, comprehensive reviews with overviews of the applications as well as the current state of research were given by Karagothian [57] and Mahesh [72].

In combustion applications jets in cross flow are used to premix fuel and air or stabilize flames [9, 29, 55, 56, 71, 104]. Another application is found in the dilution zone of combustors to tailor the combustor exit temperature profile or provide the burn-out air in Rich-Quench-Lean systems [26, 49, 67].

The application of premixed jets in hot cross flow is hardly found in literature. Therefore, the following literature overview is focused on non-reacting jet in cross flow research investigating the influences jet nozzle shape and momentum ratio on the flow and concentration fields.

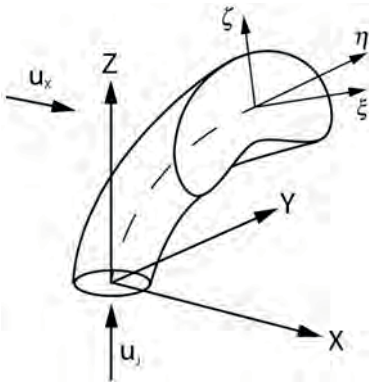

Figure 2.11: Coordinate system of the jet in cross flow experiment.

2.4.1 Overview of Non-Reacting Jet in Cross Flow Research

Similar to free jets the primary literature on jets in cross flow focuses on a standard configuration. It has a round jet nozzle and a cross flow much bigger compared to the jet nozzle to reduce wall influences. Over the years other jet nozzle shapes like square, ellipse, triangle or rectangle have been considered. Yet, the basic phenomena are similar for all of them. For that reason, the fundamental understanding of round jets will be presented first. At the end of the section the influence of the jet shape will be discussed.

The coordinate system which is used by most researchers to describe the flow field of jets in cross flow is presented in figure 2.11. An absolute Cartesian coordinate system x, y, z has its origin at the center of the jet nozzle. The x-coordinate is in the direction of the cross flow and the z-coordinate corresponds to the jet nozzle direction. The y-coordinate is normal to the x-z plane. In addition, a relative coordinate system is used which also has its origin in the center of the jet nozzle exit. ξ is bound to the jet trajectory, η is parallel to the y-coordinate and ζ is normal to the $\xi - \eta$ plane.

The main parameters to characterize jets in cross flow are the diameter of the jet nozzle D_j, velocities of the jet u_j and cross flow u_x as well as the densities of the jet ρ_j and the cross flow ρ_x. Different non-dimensional ratios are formed with these parameters. The velocity ratio:

$$R_j = \frac{u_j}{u_x}. \tag{2.36}$$

The momentum flux density ratio J of both streams:

$$J = \frac{\rho_j u_j^2}{\rho_x u_x^2}. \tag{2.37}$$

In literature J is often called momentum ratio which is also adopted in this thesis. Finally, a Reynolds number is calculated. Several methods to calculate a Reynolds number for a jet in cross flow configuration were presented in literature [57, 72]. In this thesis a jet Reynolds number Re_j is used:

$$Re_j = \frac{u_j D_j}{\nu_j}. \tag{2.38}$$

Here, D_j describes the jet nozzle diameter and ν_j the kinematic viscosity of the jet fluid. Using these non-dimensional numbers, various attempts have been made to derive simple scaling rules. Pratte and Baines [88] presented experimental data and used an $R_j D_j$ scaling to correlate jet trajectories. Keffer and Baines used $R_j^2 D_j$ to scale jet trajectories with different velocity ratios [58]. While these scaling methods are still in use [72, 73], their applicability to correlate literature data is rather poor.

Most jet in cross flow studies focus on the velocity fields, much fewer investigate the concentration fields. In the 1970s groups started to measure the concentration fields of jets in cross flow using heated jets and temperature measurements [50, 55]. They provided correlations to describe the flow and the concentration field. As shown in section 2.4.3 they fail to predict the trajectory for jets with conditions comparable to the jets investigated in this work. Experimental methods like particle image velocimetry and laser induced fluorescence allow to capture instantaneous mixing and velocity fields simultaneously [102, 104, 109]. At the same time computational studies showed that large eddy simulations and direct numerical simulations predict the concentration field much better than Renolds-averaged Navier-Stokes simulations [23, 78, 96, 119]. Although sophisticated numerical and experimental methods exist to describe jets in cross flow, no good correlation was found which is useful to describe the mixing in the cases studied here.

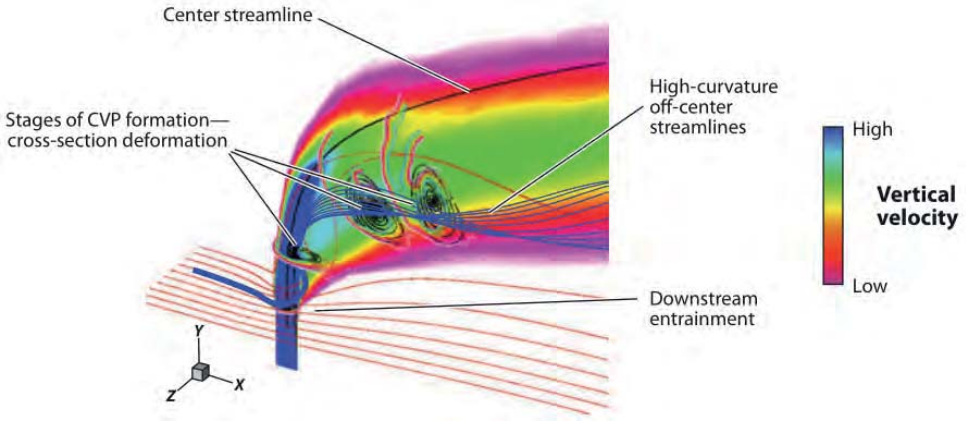

Figure 2.12: Time averaged vertical velocity field of a jet in cross flow. The development of the CVP at different positions along the jet trajectory is shown. Figure taken from [78].

2.4.2 Vortex Systems

The vortex systems of jets in cross flow are the drivers of momentum and mass exchange between jet and cross flow. They increase the contact surface massively and ultimately enhance molecular mixing. Jets in cross flow feature more vortex structures compared to free jets. Kelso and Lim [59] explained that jets in cross flow encompass a kaleidoscope of vortex phenomena even for the simplest case of transverse jets. Besides the counter rotating vortex pair (CVP) there are shear layer vortices, the horseshoe vortex and the upright vortices. These vortex systems will be briefly presented in the following sections.

2.4.2.1 Counter Rotating Vortex Pair (CVP)

The CVP is visible in the mean flow and is often considered the dominating vortex structure of a jet in cross flow, since it is the only formation visible far downstream of the jet. Figure 2.12 shows a time averaged flow field of a jet in cross flow with streamlines highlighting the CVP. The instantaneous CVP is unsteady and asymmetric and becomes symmetric only in the time averaged flow field. Several formation mechanisms of the CVP have been discussed of which the latest and most widely accepted one was presented by Kelso and Lim [59]. They combined their results of water channel and wind channel experiments to get a comprehensive understanding of formation of the CVP. Fig-

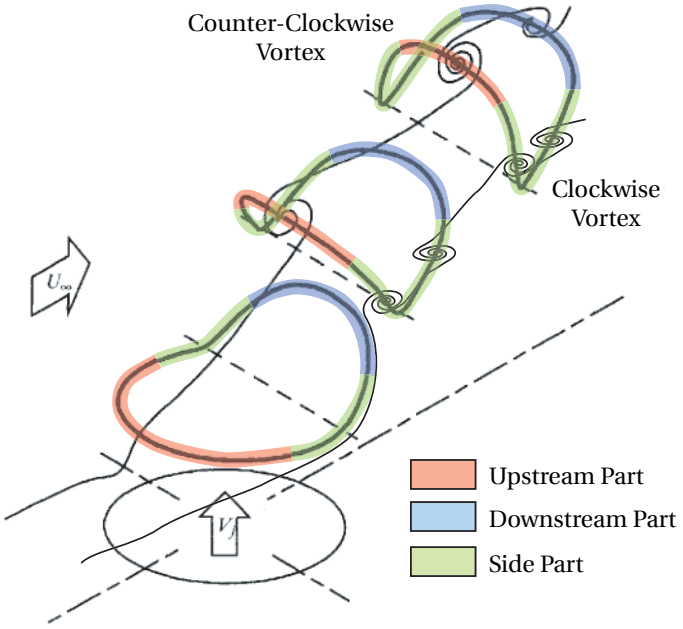

Figure 2.13: Formation of the CVP through tilting and folding of the shear-layer vortices. Figure adapted from [59].

ure 2.13 shows the essence of their findings. The colored lines mark the vortex cores of the shear layer vortices. The upstream part of the vortices tilts with the curvature of the jet. The downstream part of the vortices is less influenced by the cross flow and keeps the initial direction of the jet for longer. The difference in the upstream and downstream part leads to the folding of the side parts. These side parts then contribute to the circulation of the CVP. The CVP is dominant in the far field, in the near field its influence on mixing and velocities is of minor importance.

2.4.2.2 Shear Layer Vortices

The shear layer vortices, also called ring vortices, are similar to the ring vortices of a free jet. The main difference is their distortion by the cross flow at the sides, while they are almost undisturbed on the upstream and downstream side. In the near field they are the dominating vortex system which contributes most to the momentum and species exchange of jet and cross flow.

2.4.2.3 Horseshoe Vortices

The horseshoe vortices form within the boundary layer upstream of the jet and are similar to the horseshoe vortex of a flow around a solid obstacle. The main difference is that also a vortex in the jet nozzle forms. This transient vortex moves in the range of the boundary layer into and out of the jet pipe. For cases close to the flashback limit the horseshoe vortex can get significant influence as cross flow material can be transported into the jet pipe causing flashback. The influence on the overall mixing and flow field is small compared to the CVP and the shear layer vortices [72].

2.4.2.4 Upright Vortices

The upright vortices form in the wake of the jet and are often compared to the vortex street behind a cylinder. They have similarities but nevertheless are different as shown by Fric and Roshko [29]. They seem to exist for various velocity ratios, originating from the cross flow boundary layer and are caused by the pressure difference between the jet and the boundary layer. They are the main mixing driver in the wake region, but compared to CVP and shear layer vortices their contribution to overall mixing is small. For that reason the mixing in the wake region is weak.

2.4.3 Trajectory Correlations for a Jet in Cross Flow

There are different definitions of jet trajectories in the jet in cross flow context. The most common ones are curves connecting the velocity or concentration maxima starting from the center of the jet nozzle exit. Alternative trajectories are characterized by vorticity maxima, pressure maxima or the center streamline. Those are more complicated to determine and are not that common.

Callaghan and Ruggeri [19] were one of the first to present an empirical trajectory correlation. Their work was based on temperature measurements where the jet was preheated and the mixture calculated from the temperature field. The trajectory therefore describes the curve of maximum jet mixture fraction:

$$\frac{z}{D_j} = 1.91 \left(\frac{\rho_j u_j}{\rho_x u_x} \right)^{0.606} \left(\frac{x}{D_j} \right)^{0.303} . \tag{2.39}$$

They validated the correlations for jet Reynolds numbers $Re_j > 50,000$ and momentum ratios $J = 4 - 50$.

Since then a lot of effort was spend by various groups to find an universal trajectory correlation, e.g. [49, 50, 55]. Most trajectory correlations, whether for velocity or concentration trajectories, have the following form:

$$\frac{z}{D} = A J^{B_c} \left(\frac{x}{D_j} \right)^{C} . \tag{2.40}$$

A, B_c and C are empirically defined constants. These parameters differ for every experiment and, therefore, the correlations can only be used for rough estimations.

Various groups also worked on analytical models to scale jets in cross flow, e.g. [2, 16, 43, 44, 49, 50, 55, 58, 90]. First analytical models were presented by Volinsky and later extended by Abramovich [2]. They assumed that the deflection of the jet can be modeled with the forces that affect an inclined wing profile where the main parameters are the drag coefficient C_D and the momentum ratio of the jet J. For a constant drag coefficient their scaling of the trajectory depends on the product of the jet momentum J and diameter D_j. The same scaling rule was also proposed by other groups, e.g. [58]. In figure 2.14 on the left experimental data of Kamotani and Greber [55] for jets with different momentum ratios is scaled with JD_j. It can be seen that the curves do not lie on top of each other.

A second method based on entrainment was presented by Hasselbrink and Mungal [44]. They performed a similarity analysis of a jet in cross flow for high momentum ratios (J>100) which is based on Broadwells' and Breidenthals' [16] approach. They neglected pressure terms and divided the flow field into a jet region, where the jet is unaffected by the cross flow and a wake-like region, where the jet is deflected. The main difference to the first approach is that they do not include drag coefficients but entrainment coefficients to model the deflection. For constant entrainment coefficients this approach leads to a scaling of the trajectory depending on the product of the square-root of the momentum ratio $J^{0.5}$ and the jet diameter D_j. Figure 2.14 on the right shows

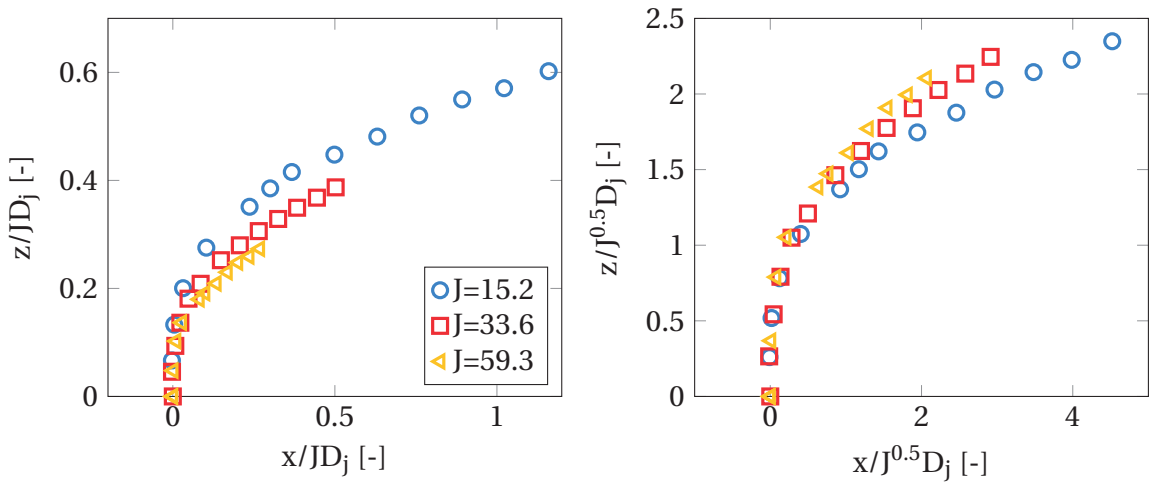

Figure 2.14: Velocity trajectory as presented by Kamotani and Greber [55] scaled based on drag on the left and based on entrainment on the right.

Kamotani and Grebers data scaled with $J^{0.5}D_j$. The curves do not lie on top of each other and therefore the scaling method seems to miss some influence.

Both methods fail to correlate comparable data of literature. Forliti [28] recently proposed that the trajectory is influenced by both drag and entrainment. He assumed that the entrainment coefficient c_{ej} of a jet with momentum ratio $J > 16$ is similar to a free jet as also proposed by Ricou and Spalding [90]. Forliti calculated the drag coefficient of a circular jet from experimental data to be $C_D = 1.7$. The coefficient is higher than for a solid cylinder, because the fluid jets gets distorted to a kidney shaped cross section increasing the drag. Forlitis' scaling parameter B combines momentum ratio, drag and entrainment coefficients to characterize the ratio of initial jet momentum and cross flow momentum which is transferred to the jet:

$$B = \frac{J}{\frac{2C_D}{\pi} + c_{ej}J^{0.5}}. \tag{2.41}$$

In figure 2.15 it can be seen that the velocity trajectories of different momentum ratios lie on top of each other if the data is scaled with Forlitis' parameter B. The scaling also works for mixture trajectories. The factor B becomes zero if the momentum ratio becomes zero and tends to infinity for increasing momentum ratio. More details of the model are found in [28]. The model was found to be the best available so far for correlating experimental data of different momentum ratios and will be used in this work.

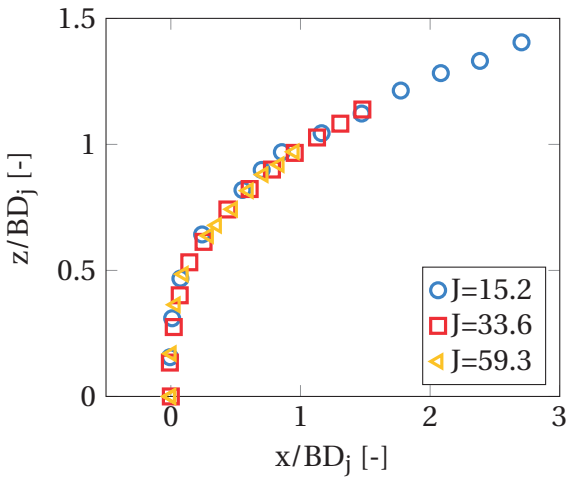

Figure 2.15: Velocity trajectory as presented by Kamotani and Greber [55] normalized with the Forlitis' parameter B [28].

2.4.4 Mixing Field

Many applications of jets in cross flow have the goal to achieve good mixing. Good mixing means that the concentration gradients are reduced as quickly as possible. Perfect mixing is obtained when no concentration gradient is left in the flow field.

A comparison of the jet mixture fraction f along the mixture trajectory of a free jet and a jet in cross flow shows that mixing in a jet in cross flow is more efficient. In figure 2.16 the decays of the jet concentration against the mixture trajectory ξ for a free jet and for jets in cross flow with different momentum ratios as presented by Kamotani and Greber [55] are shown. The three curves are very similar in the near field $\xi/D < 5$ of the nozzle but are axially shifted due to different potential core length. For jet mixture fractions below 0.5-0.6, however, the jet in cross flow cases continue to decrease significantly below the values of the free jet. At $\xi/D = 10$ the J = 59.6 case overtakes the J = 15.3 case and reaches slightly lower values of jet mixture fraction in the observed range. Beyond $\xi/D = 20$ the jet mixture fractions of the jet in cross flow cases are almost constant whereas for the free jet case the mixture fraction value still decreases towards the asymptotic $f \approx 0$. The perfect mixture is different for each case, but all are close to zero. Summarizing figure 2.16 it can be stated that the jet in cross flow configuration mixes more rapidly with respect to the jet trajectory in the near field with a distinct influence of the momentum ratio

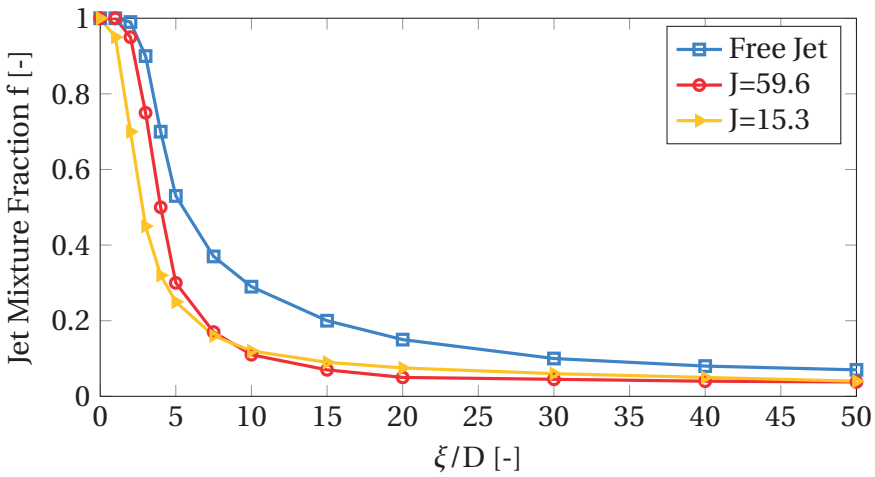

Figure 2.16: Concentration decay along the jet trajectory for a free jet and jets in cross flow configurations with momentum ratios J = 15.3 and 59.6, respectivly. Reproduced from [55].

J in the potential core region. In the far field at $\xi/D = 10$ the slope of the jet in cross flow configuration becomes smaller compared to the free jet configuration. However, the jet in cross flow configurations have lower jet mixture fractions for the observed range. Several groups [44, 55, 72, 104] found similar results when comparing free jets and jets in cross flow. As shown later in section 5.2 the enhanced mixing in the near field is explained by higher velocity and concentration gradients in the shear layers. The cross flow drags jet material away and therefore reduces the thickness of the shear layer which enhances the momentum and species transport. In the far field the velocities of jet and cross flow become almost equal which reduces the shear stress and, therefore, slows down the mixing process.

2.4.4.1 Potential Core

The potential core of a jet in cross flow is shorter in comparison to a turbulent free jet and depends on the momentum flux ratio J. Hasselbrink and Mungal [44] used the k-ϵ model presented by Coelho and Hunt [20] to derive a correlation for the length of the potential core l_{PC}:

$$l_{PC} = \frac{-1 + \left(1 + 24 \cdot J^{-0.5}\right)^{0.5}}{2 \cdot J^{-0.5}} \tag{2.42}$$

The potential core of a free jet ($J \rightarrow \infty$) is hereby about 6 diameters long and gets shorter for jets in cross flow with decreasing momentum ratio. For very low momentum ratios the length of the potential core approaches zero.

Hasselbrink and Mungals focus were high momentum ratio cases which is why they captured well the asymptote for the free jet. For cases with momentum ratios of $J < 20$ the length of the potential core is overestimated. For cases in literature with low momentum ratio, e.g. [33], potential core lengths 4 times shorter than predicted by equation 2.42 are reported. No alternative correlation for the length of the potential core was found in literature. A new approach will be proposed in section 5.2.3.

2.4.5 Jet Nozzle Shapes

Jet nozzle shapes were investigated by different groups in the past, e.g. [37–39, 45, 46, 68–71, 79]. All authors agree that the far field mixing ($\xi > 20D_j$) is not influenced by the nozzle shape. Haven and Kurosaka [46] as well as Gutmark [39] found that the main flow features presented in section 2.4.2 are present for all analyzed geometries. However, the size and location of the various vortex systems mentioned in section 2.4.2 is very different in the core region. Only further downstream the CVP always dominates the flow field. Liscinsky et al. [71] could show that the mixing fields of different injectors become similar beyond $x/D > 5.5$ while they vary closer to the jet nozzle.

Vortex generators like delta wings or swirlers in the jet pipe were also investigated [69, 120]. The mixing enhancement effect through delta wings was found to be very small and for many setups mixing was even reduced. Swirlers were also tested and all of them showed worse mixing than the comparable jet shape without a swirler.

2.5 Lift-Off

No model for flame lift-off of a premixed jet in vitiated cross flow is available in literature. Closest to the focus of this work are jet diffusion flames which are common in literature. Below two different but common approaches to model

flame lift-off will be discussed. The first approach for a lift-off model was given by Kalghatgi [54]. His experiment features a fuel jet penetrating a volume of stagnant air with both fluids at ambient temperature. He found the flame lift-off height (LO) to be at the equilibrium of the turbulent flame velocity S_t and the flow velocity u_j. A nondimensionalization with the jet diameter allows the definition of a dimensionless lift-off height:

$$\mathrm{LO} = \frac{z(S_t = u_j)}{D_j}. \tag{2.43}$$

The equilibrium is reached in the shear layer where at the one hand the flow velocity decreases and on the other hand the turbulent flame speed increases due to turbulence and stoichiometric fuel-air mixture. There are two main differences to this work. Kalghatgis jets were surrounded by stagnant air at ambient temperature and his jets were not premixed but pure fuel. A scheme of the flow velocity distribution downstream of the nozzle and the turbulent flame speed in the shear layer as proposed by Kalghatgi is shown in figure 2.17. In addition to the turbulent flame speed of the fuel jet, the turbulent flame speeds of lean premixed jets surrounded by cold ambient air and hot ambient air are labeled. Cold corresponds to T_∞ = 288K and hot to T_∞ = 1734K. Depending on the ambient temperatures the flame speeds change. For the case of cold ambient fluid the turbulent flame speed decreases when ambient fluid is entrained by the jet as the mixture gets leaner and the mixture temperature is not changed. For the hot ambient fluid case the mixing also dilutes the jet but the additional enthalpy increases the turbulent flame speed which leads to the maximum. However, for the given jet velocity there is no equilibrium of premixed turbulent flame speed and jet velocity found. Therefore, the theory would predict blow-out. Still, his idea of finding the equilibrium of turbulent flame speed and mean flow velocity is extended to predict the lift-off height of jet flames in chapter 6. Because his idea is driven by the flame propagation speed, his method will be referred to as the flame propagation mechanism.

The equilibrium between turbulent flame speed and flow velocity can also be expressed using a ratio of a flow timescale τ_t and reaction timescale τ_c. This leads to the previously presented turbulent Damköhler and Karlovitz numbers, see section 2.2.3. These dimensionless numbers reproduce Kalghatgis results and are used in chapter 6 to model flame lift-off.

Another approach to model flame lift-off with the focus on auto-ignition is

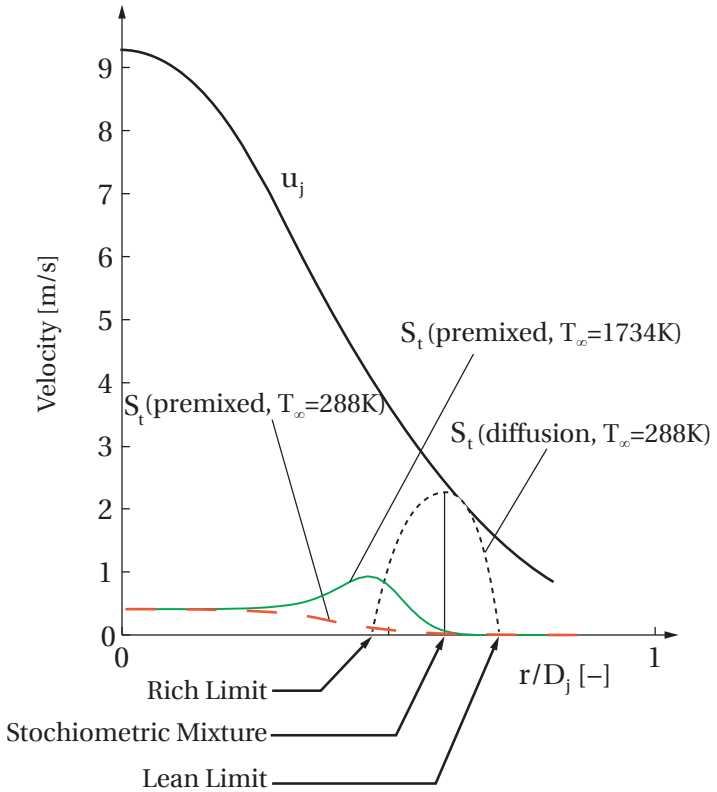

Figure 2.17: Radial velocity profile of a free jet downstream of the nozzle where the flame stabilizes. The turbulent flame speeds of a diffusion flame and of premixed flames are drawn. Based on [54].

common in literature. Markides and Mastorakos [74] studied the lift-off of a diluted hydrogen jet flame which enters a domain of hot co-flow. The co-flow temperature is between 950-980K. In contrast to Kalghatgis model using a turbulent flame speed their lift-off depends only on the ignition delay and the flame speed is negligible. This difference is explained by the vitiated co-flow which induces auto-ignition. When the jet enters the domain the turbulent mixing between jet and co-flow starts. After the ignition delay time an auto-ignition spot occurs at a volume of fluid with the most reactive mixture fraction (MRMF). Contrary to Kalghatgis flame stabilization in a stoichiometric region, the MRMF is very lean. Very little fuel but much enthalpy from the hotter co-flow in the mixture promotes the ignition. The ignition delay Damköhler number Da_{ign} can describe the lift-off phenomenon dominated by auto-ignition, see section 2.2.3.

There are more concepts on lift-off available in literature, but the two examples already consider the main influences, namely flow velocity and the chemical drivers laminar flame speed and ignition delay. As presented in section 2.2.1, Habisreuther [40] showed that a 1D laminar flame is either driven by laminar flame speed or auto-ignition. Since a turbulent jet consists of several different flamelets it is not possible to determine one dominant mechanism for the whole flame surface. Thus, for this work both mechanisms are taken into consideration to model the lift-off height of the jet in chapter 6.

2.6 Nitrogen Oxide Formation

One goal of this work is to show the potential of different jet nozzle configurations to reduce nitric oxide emissions. Therefore, the NO formation mechanisms are presented. The literature distinguishes between different chemical reactions which lead to nitric oxide:

- Zeldovich mechanism
- N_2O mechanism
- Fenimore mechanism
- Fuel-bound nitrogen oxide mechanism

- NNH mechanism

Hoferichter [48] showed that for the combustion of methane at 1 to 20 bar and equivalence ratios $0.33 < \phi < 1$ the Zeldovich and N_2O mechanisms contribute over 99% of the overall NO_x. Therefore, the other three mechanisms are neglected in this work and will not be further discussed. The overall NO_x concentration consists of NO and NO_2. At high temperatures the chemical equilibrium between NO and NO_2 lies on the side of NO. At lower temperatures NO is oxidized to NO_2. Since both nitrogen oxides are noxious, throughout this work only their sum will be examined. In the following, the main NO_x contributing mechanisms will be briefly introduced.

The Zeldovich mechanism is also called "Thermal" mechanism, because it scales mainly with temperature. For temperatures higher than 1800K the Zeldovich mechanism generates the largest share of the total NO_x emissions. While Zeldovich was the first to formulate the NO formation path and also extended it later [115], Bowmans' [13] suggestion of the formulation is more common nowadays:

$$O + N_2 \leftrightarrows NO + N \tag{2.44}$$

$$N + O_2 \leftrightarrows NO + O \tag{2.45}$$

$$N + OH \leftrightarrows NO + H \tag{2.46}$$

The reaction chain needs a high activation energy (319,05kJ/kmol) for reaction 2.44 and therefore is strongly dependent on temperature. High concentrations of OH or O radicals can significantly increase the NO formation rate [115].

The second important mechanism is the N_2O mechanism which contributes an important part of the overall NO_x for lean premixed flames $\phi < 0.8$ [77]. N_2O is produced as an intermediate species with a short lifespan which is converted to NO or N_2 [22]. The key reaction which starts the mechanism was suggested by Malte and Pratt:

$$O + N_2 + M \leftrightarrows N_2O + M \tag{2.47}$$

M stands for some arbitrary collision partner. There are many reaction pathways which can follow. The important reaction for this work is the one which

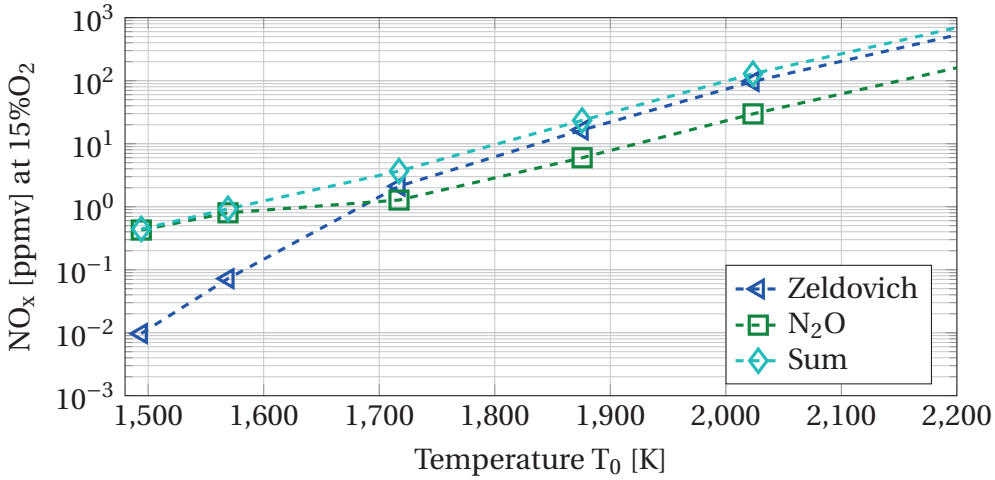

Figure 2.18: Contribution of reaction pathways to the overall NO_x concentration as a function of flame temperature at a residence time of 95 ms for atmospheric lean premixed combustion with T_0 = 693K initial temperature. Data taken from [48].

generates NO:

$$N_2O + O \leftrightarrows NO + NO \tag{2.48}$$

The overall NO_x creation for premixed flames depends mainly on temperature and residence time, whereby temperature has a stronger influence. Figure 2.18 shows the amount of NO created by the three presented mechanisms 95 ms after the flame front. It is evident that the Zeldovich mechanism dominates for temperatures above 1700 K while the N_2O mechanism is more important for temperatures below 1700 K. The dominance of the Zeldovich mechanism decreases for lower residence times, however, the order of the mechanism's contributions stays the same. Figure 2.19 shows the overall NO for different residence times, where 0 ms is directly after the flame front. In conclusion, the best method to avoid NO is to lower the overall temperature and to reduce the residence time, especially in high temperature regions [4].

2.7 Carbon Monoxide Formation

Carbon Monoxide (CO) is a very toxic gas for humans and animals. Most regulators all over the world force the gas turbine manufacturers to keep the CO emissions below 10 ppmv at 15% O_2 . In gas turbine combustion the CO is pro-

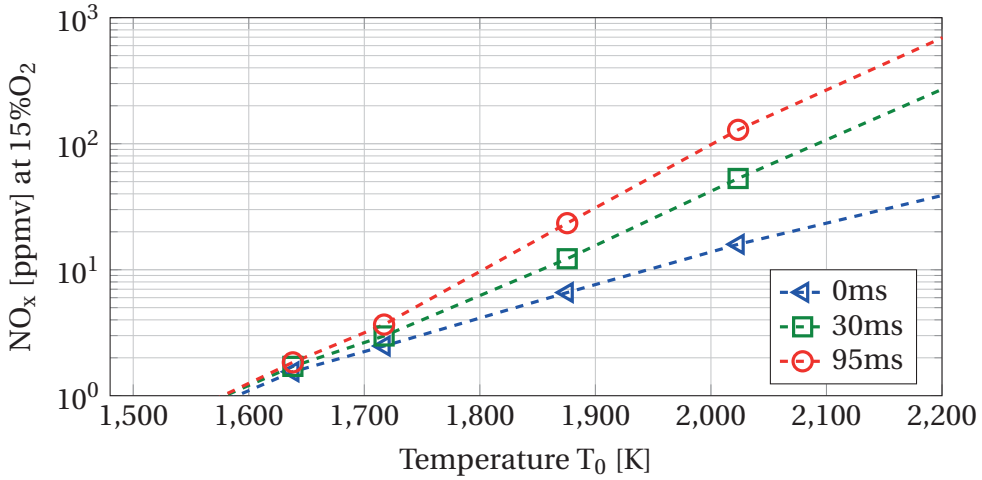

Figure 2.19: NO_x concentration from atmospheric lean premixed combustion as a function of flame temperature and residence time, with T_0 = 693K initial temperature. Data taken from [48].

duced within the flame front and converted to carbon dioxide CO_2 afterward until the equilibrium is reached. The equilibrium CO concentration rises with temperature [48,95]. In gas turbine design CO is a main factor to determine the length of combustors. If the residence time is too short, the CO oxidation is not finished before the flow enters the turbine. High CO emissions are the consequence. Figure 2.20 shows the CO emissions for different residence times. It is seen that there is almost no difference between 30 ms and 95 ms cases, but a big difference to the 0 ms case. So CO needs a certain residence time after the flame front to reach its equilibrium concentration before entering the turbine. This is one of the main reasons why combustor designs with extremely short residence times are not realized. However, long residence times produce high amounts of nitric oxide. So a tradeoff has to be found for every design.

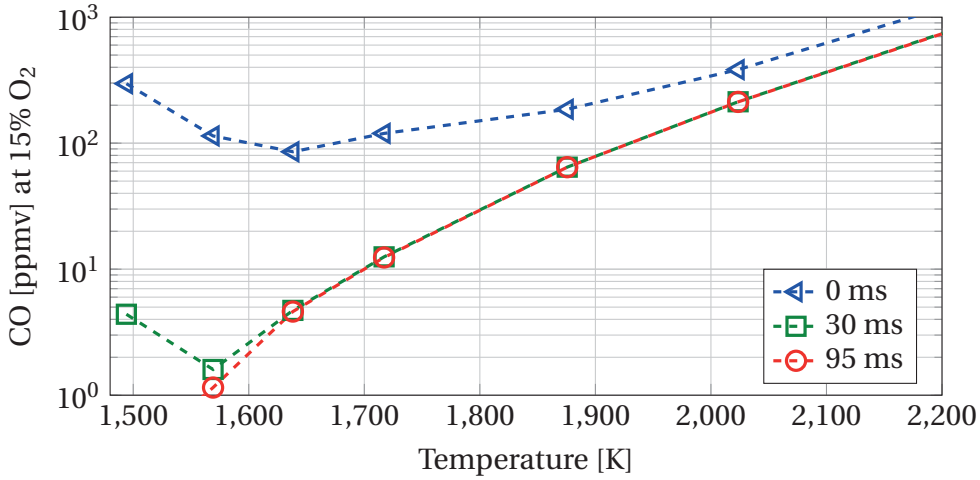

Figure 2.20: CO concentration from atmospheric lean premixed combustion as a function of flame temperature and residence time, with T = 693K initial temperature. Data taken from [48].

3 Test Rig

3.1 Operating Conditions of a Heavy-Duty Gas Turbine

Table 3.1 shows a list of the typical operating conditions of heavy-duty gas turbine combustors. Pressure, mass flows, and power were taken from [15], temperatures can be found in [17,41,95] and the combustors velocities in [14]. The scaling calculations to dimension the laboratory model combustor of the test rig presented in the next section are performed on basis of these operating parameters.

Parameter	Value	Unit
Pressure	20	bar
Mass Flow	>500	$\frac{kg}{s}$
Electrical Power	>200	MW
Adiabatic Flame Temperature	>1800	K
Turbine Inlet Temperature	>1600	K
Combustor Velocity	>40	$\frac{m}{s}$

Table 3.1: Operating conditions of a heavy-duty gas turbine.

3.2 Scaling of the Experiment

The laboratory model combustor is operated at atmospheric pressure in order to easily apply optical and intrusive measurement methods. It has a second stage with a jet in cross flow arrangement. The combustion air is preheated to 673K as this temperature corresponds to typical compressor outlet temperatures. The jet nozzles are exchangeable to investigate different configurations.

Starting with the velocity, pressure, and temperature of the heavy-duty gas

turbine combustor, a similarity scaling based on Reynolds number Re and Damköhler number Da is applied to dimension the laboratory model combustor. Re and Da are known from premixed combustion theory [115] as the dimensionless numbers which characterize the premixed combustion regime. As Re is very large in the heavy-duty gas turbine combustor due to the high pressure, strict similarity cannot be achieved.

With the assumption that auto-ignition is one of the main drivers of the reacting jet in hot cross flow an ignition delay Damköhler number Da_{ign} is suitable to scale the experiment. It is defined as:

$$Da_{ign} = \frac{\tau_t}{\tau_{ign}}. \tag{3.1}$$

The turbulent timescale is calculated by:

$$\tau_t = \frac{l_t}{u_j'} \sim \frac{D_j}{u_j}. \tag{3.2}$$

The integral length scale l_t is assumed to be proportional to the jet diameter D_j and the velocity fluctuation of the jet flow u_j' is assumed to be proportional to the jet velocity u_j.

The calculation of the ignition delay time is more complex, but correlations exist, e.g. [106]. For the scaling it is not necessary to know the ignition delay times but only that they are almost inversely proportional to pressure [106]:

$$\frac{p_{Eng}}{p_{Exp}} \approx \frac{\tau_{ign,Exp}}{\tau_{ign,Eng}}. \tag{3.3}$$

$\tau_{ign,Eng}$ and $\tau_{ign,Exp}$ are the ignition delay times in the gas turbine engine and the experiment, respectively.

From equation 3.3 follows that the ignition delay time for the atmospheric experiment will be higher by the factor of the pressure ratio $p_{Eng}/p_{Exp} = 20$. To get the same ignition delay Damköhler number for the experiment as for the real engine, the turbulent timescale of the experiment $\tau_{t,Exp}$ has to be increased. With equations 3.1 to 3.3 the turbulent time scale of the experiment $\tau_{t,Exp}$ can

Description	Parameter	Value	Unit
Pressure	p	1	bar
Cross Flow Velocity	u_x	17	m/s
Jet Flow Velocity	u_j	10-180	m/s
Cross Section of Cross Flow	A_x	0.25	m^2
Jet Diameter	D_j	0.015-0.1	m

Table 3.2: Targeted operating conditions of the scaled experiment.

be calculated to compensate for the increased ignition delay time scale $\tau_{\text{ign,Exp}}$:

$$\tau_{\text{t,Exp}} = \underbrace{\frac{\tau_{\text{ign,Exp}}}{\tau_{\text{ign,Eng}}}} \cdot \tau_{\text{t,Eng}} \tag{3.4}$$

$$\left.\frac{l_t}{u'}\right|_{\text{Exp}} = 20 \cdot \left.\frac{l_t}{u'}\right|_{\text{Eng}} \tag{3.5}$$

$$\left.\frac{D_j}{u_j}\right|_{\text{Exp}} = 20 \cdot \left.\frac{D_j}{u_j}\right|_{\text{Eng}} \tag{3.6}$$

$$\frac{D_{\text{j,Exp}}}{D_{\text{j,Eng}}} \cdot \frac{u_{\text{j,Eng}}}{u_{\text{j,Exp}}} = \frac{\tau_{\text{ign,Exp}}}{\tau_{\text{ign,Eng}}} = 20. \tag{3.7}$$

A reduction of the flow velocity by a factor of 5 and a scale-up of the geometry by a factor of 4 were chosen with respect to the infrastructural limits of the laboratory:

$$\frac{D_{\text{j,Exp}}}{D_{\text{j,Eng}}} = 4; \qquad \frac{u_{\text{j,Exp}}}{u_{\text{j,Eng}}} = \frac{1}{5}. \tag{3.8}$$

With these values the temperatures, mass flows and geometric measures of the scaled experiment are determined. Table 3.2 gives an overview of the calculated experimental operation conditions and dimensions.

3.3 Description of the Experiment

Based on the ignition delay Damköhler number scaling the test rig which is shown in figure 3.1 was designed. It consists of four modules with a cross section of 500 x 500 mm each. The individual modules are placed on a rail system to accommodate thermal expansion. The connecting flanges are made of thin 3 mm sheet metal and have a flange height of 200 mm to reduce stress from thermal deformations of the connected modules.

A plenum feeds 16 premixed natural gas burners in a four by four arrangement. The flames produce exhaust gas in the primary combustion zone which is partly insulated with ceramics and partly impingement cooled. The next module is the secondary combustion zone which has windows on the top and on the sides. The windows are replaced by ceramically insulated steel plates with slots to perform intrusive temperature or emission measurements. The bottom plate is impingement cooled and contains the jet inlet. The jet inlet pipe has a diameter of 100 mm. Orifices are installed inside the pipe to decrease the diameter or the shape of the nozzle. The last module is ceramically insulated and allows emissions measurements after longer residence times.

3.3.1 Plenum

The plenum houses 16 alternating swirl burners generating the vitiated cross flow. Eight swirlers rotate clock- and eight counterclockwise to eliminate the global swirl. The plenum has four maintenance ports for easy access to damaged components. As shown in figure 3.2, the combustion air enters the plenum from the top (1) and then passes the face plate (2). This flow configuration ensures cooling of the face plate. Natural gas is injected through small pipes (3) and mixes with the air in the combustor tubes. Before entering the combustion chamber (4) the flow passes a swirl generator. The swirl creates a recirculation zone in the combustor and anchors the flames.

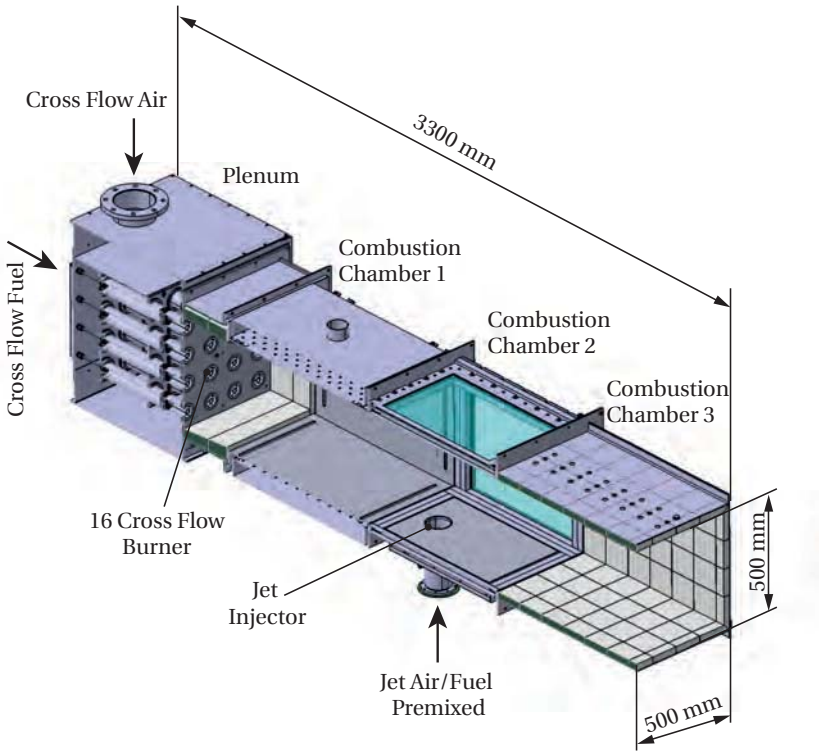

Figure 3.1: Scheme of the jet in cross flow experiment. The main flow enters from left and the jet is injected from the bottom of combustion chamber 2.

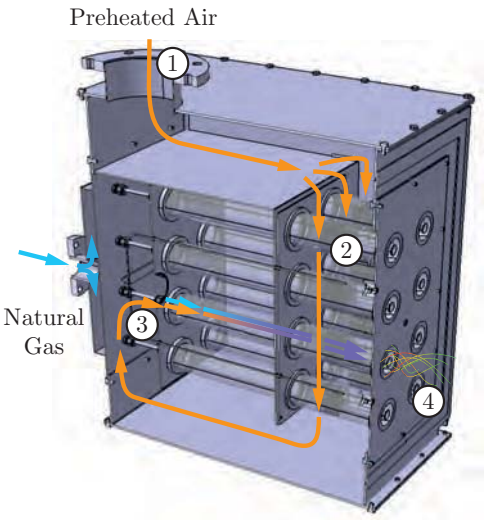

Figure 3.2: Flow path trough the plenum.

Parameter	Value	Unit
Pressure	1	bar
Pressure Drop	20	%
Mass Flow	34-80	$\frac{g}{s}$
Thermal Power	33-165	kW
Preheating Temperature	288-700	K
Equivalence Ratio	0.43-1	-

Table 3.3: Operating conditions of the swirl burner.

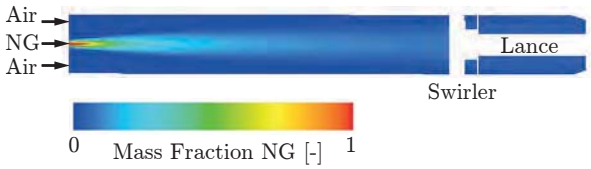

Figure 3.3: Mixing of air and natural gas (NG) in the burner tube.

3.3.1.1 Swirl Burner

Figure 3.3 shows a CFD simulation of one of the swirl burners. The natural gas enters the domain with high velocity and mixes with the air as a turbulent jet in co-flow.

The burner was tested on a single burner test rig. The operational window is listed in table 3.3. For a preheating temperature of $T_0 = 673K$ the lean blow-out limit of the burner was $\phi = 0.43$ for all tested conditions. The burner pressure drop can be tailored by the swirler slot width. A very high relative pressure drop of 20% was chosen to avoid thermoacoustic coupling.

To assess the premixing quality of the jet mixer design the burner was also operated with perfectly premixed flow generated by an industrial premixer upstream of the burner. The results show that the nitrogen oxide emissions achieved with the two mixing methods are the same, see figure 3.4. The emissions are close to NO_x concentrations reported in [95] which were calculated using a perfectly premixed laminar flame code for the same operating conditions and at similar residence times.

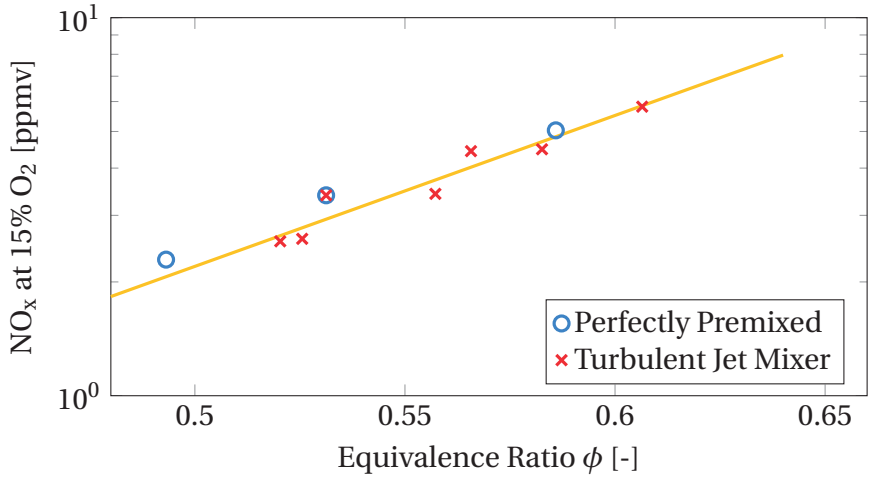

Figure 3.4: Measured NO_x emissions of the single burner for perfect premixing and turbulent jet mixing with preheating temperature $T_0 = 673$ K, ambient pressure, and natural gas as fuel.

3.3.2 Combustion Chamber 1

Combustion chamber 1, see figure 3.5, has to withstand the high temperatures of primary combustion (up to 1.1 MW, 1820K). The first 300 mm of combustion chamber 1 are insulated with 50 mm thick ceramic plates. This part is in direct contact with the swirl stabilized flames which cause high velocities close to the wall and therefore high heat transfer coefficients. Simple impingement cooling would not be able to control the wall temperatures. After the ceramic section the hot combustion products create a turbulent channel flow with lower heat transfer coefficients close to the wall such that it is cooled sufficiently with a simple impingement cooling system placed on the outside of the combustor liner. The wall temperature is designed to be about 800-1000 K to keep the thermal radiation low which could disturb optical measurements.

Due to the rectangular channel design the wall temperature is inhomogeneous which leads to buckling. To reduce mechanical deformations thermal stress relieve pockets are cut into the walls and sealed with thin steel sheets.

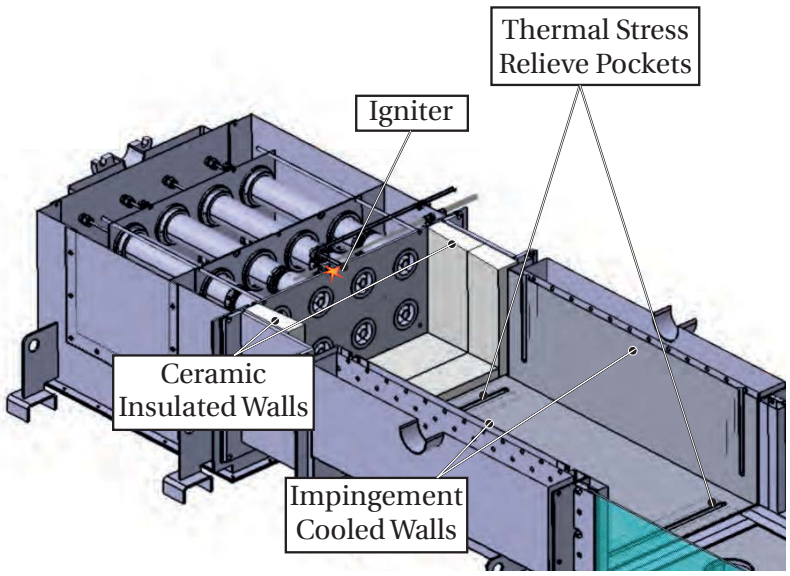

Figure 3.5: Combustion Chamber 1 with the ceramic insulated part, thermal stress relive joints, igniter and impingement cooling.

3.3.3 Combustion Chamber 2

All measurements concerning the second stage are carried out in combustion chamber 2. As shown in figure 3.6, the chamber consists of a frame made of square tubes, windows, and a bottom plate with the jet inlet. The square tubes are water cooled and prevent thermal expansion of the module as any deformation could break the windows which are on the sides and on the top. The windows are float-mounted in a stiff steel frame and are removed easily to have quick access to the injector. The windows are replaced with ceramic insulated steel plates with slots, to insert emission or temperature probes. The film cooling of the windows is realized with pressurized air. Due to the very high melting point and the low thermal expansion of quartz glass their cooling is not a critical issue. Too weak cooling does not damage the windows, but the thermal radiation can damage laboratory equipment and must be avoided.

The bottom plate is mounted flush with the frame and is impingement cooled similar to combustion chamber 1 to avoid strong thermal radiation. A 100 mm pipe is attached to the plate to inject the jet material into the combustion chamber. Different jet nozzles are mounted in this pipe to investigate smaller diameters or other shapes.

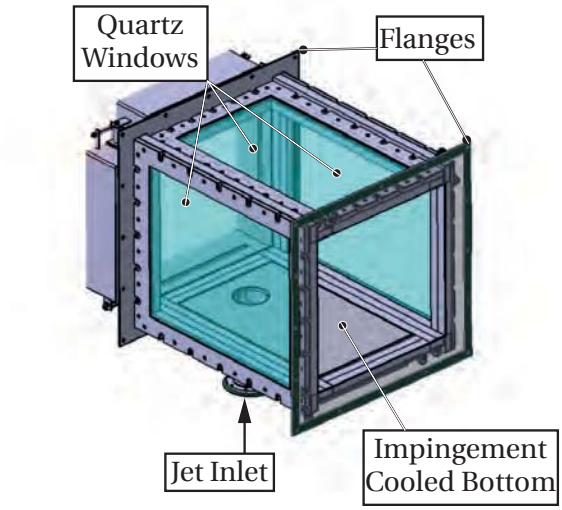

Figure 3.6: Combustion chamber 2 with three windows.

Since the attached modules combustion chamber 1 and combustion chamber 3 are subject to strong thermal deformations the modules are connected with large flanges. The size of the flanges allows for elastic deformation.

3.3.4 Combustion Chamber 3

Combustion chamber 3, see figure 3.7, is ceramically insulated and leads to a large 1000 x 1000 mm cross section exhaust duct after a gap to provide an open end boundary condition to minimize thermoacoustic oscillations. A large volume flow blower generates a venting air mass flow in the laboratory which also exits through the gap between Combustion chamber 3 and exhaust duct. Therefore, the hot exhaust is cooled before exiting the stack into the atmosphere.

3.4 Jet Geometries

In order to test different jet nozzles diameters and shapes, orifices are mounted into the 100 mm round jet pipe. The inserts reduce the original diameter of 100 mm to 50 mm, 30 mm and 15 mm, respectively. Additionally,

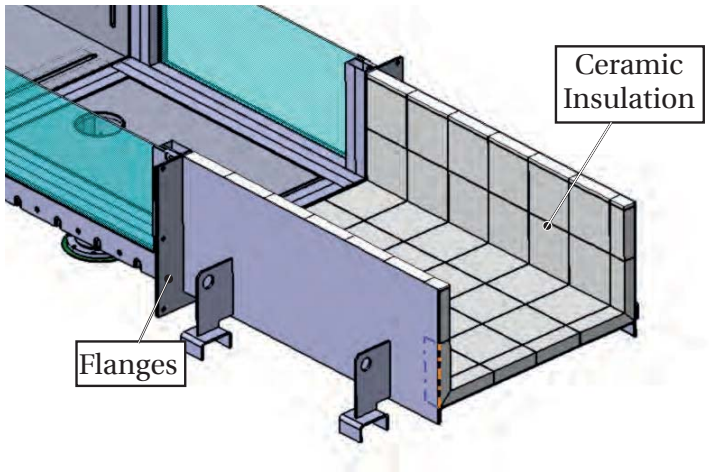

Figure 3.7: Combustion Chamber 3 with ceramic insulation.

inserts with triangle and slot shape but the same cross section area as the corresponding round nozzles were designed. The nozzles are rotated to vary their orientation with respect to the cross flow. In figure 3.8 the investigated configurations are shown. The round injector (P) is the reference configuration. The majority of literature on jets in cross flow deals with circular jets. The second configuration is the slot which is aligned parallel or perpendicular to the cross flow direction. The parallel slot (S1) is a small obstruction for the cross flow, while the perpendicular slot (S2) forms a larger barrier. The last configuration is the equilateral triangle. The edge of the first one is pointing upstream (T1), the edge of the second one is pointing downstream (T2). The edges of all non-circular configurations have radii of 2.5 mm.

For the plain jet four different diameters were manufactured, while for the slots and triangle 30 mm and 50 mm sizes are available. To keep the mass flow and momentum ratios equal for different configurations, the area of the slots and triangles is equivalent to the corresponding plain jet, see table 3.4. In this work, a slot configuration with the same area as a 50 mm plain jet is referred to as 50 mm slot.

3.5 Operating Conditions

Table 3.5 shows the parameters of the jet and cross flow for the reacting and the non-reacting cases. For the non-reacting cases the cross flow air was pre-

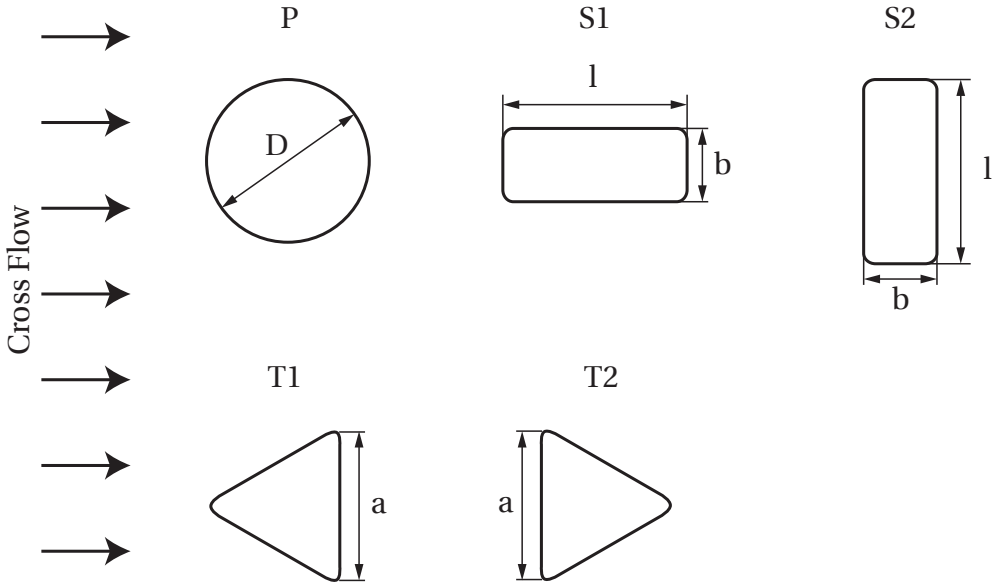

Figure 3.8: Overview of the different nozzle configurations which are tested.

Configuration	D_j [mm]	A [mm^2]	l [mm]	b [mm]	a [mm]
P	100	7850	-	-	-
P	50	1960	-	-	-
P	30	707	-	-	-
P	15	177	-	-	-
S1/S2	50	1960	70	28	-
S1/S2	30	707	52	13	-
T1/T2	50	1960	-	-	67
T1/T2	30	707	-	-	40

Table 3.4: Characteristic parameters of the available jet shapes.

heated to T_x = 400 K, while the jet air mass flow was kept at ambient temperature T_j = 293 K. The jet air mass flow was adjusted to get momentum flux ratios 15 < J < 42. For the reacting cases the cross flow air is preheated to T_x = 673K and the jet to 288K < T_j < 673K. In the combustion experiments reported in this work the primary zone is operated at an equivalence ratio range of 0.45 < ϕ_x < 0.55 corresponding to an adiabatic flame temperature of 1643K < $T_{ad,x}$ < 1821K . The jet equivalence ratio is in the range of 0.33 < ϕ_j < 1. Based on the fresh gas properties of the jet and the hot gas properties of the cross flow the investigated momentum flux ratios are between 6 < J < 210.

In the non-reacting case the cross flow density and temperature are kept constant for all operation points. The mass flows of jet and cross flow depend on the momentum flux of the operation point. For the reacting case u_j and ρ_j are the velocity and density of the unburnt jet flow, while u_x and ρ_x the velocity and density of the burnt products of the primary zone combustor.

	Reacting Cases		Non-Reacting Cases	
	Cross Flow	Jet	Cross Flow	Jet
Air mass flow $\dot{m}$ [$\frac{g}{s}$]	760	9.8-131.5	781.9	27.8-46.5
Natural gas mass flow $\dot{m}$ [$\frac{g}{s}$]	17.9-21.9	0.5-7.5	–	–
Equivalence ratio ϕ [−]	0.45-0.55	0.33-1	–	–
Preheating temperature T_0 [K]	673	288-673	400	293
Adiabatic flame temperature T_{ad} [K]	1643-1821	1472-2391	–	–
Area A [mm^2]	250k	177 – 7850	250k	177 – 7850
Reynolds Number Re [−]	24k	30k	68k	38k-63k
Momentum Ratio J [−]	–	15-42	–	6-210

Table 3.5: Operation conditions of the jet in cross flow experiment.

4 Measurement Methods

In the framework of this thesis several measurement techniques were applied. The jet mixture fraction field reconstruction in non-reacting experiments was determined using spatial temperature measurements. Flame position and shape were investigated with standard analysis of OH*-chemiluminescence. The mixture fraction field of the reacting flow is analyzed using the Mie scattering of laser illuminated particles. Velocity fields are obtained from particle image velocimetry. O_2, CO as well as NO_x species were detected using a conventional exhaust gas measurement unit connected to a water cooled suction probe. The following section introduces each technique, the test set up, and the evaluation methods.

4.1 Mixture Fraction Measurements

A common method to determine the mixture fraction of non-reacting mixing flows are temperature measurements. One of the flows is preheated so that the enthalpy at any point in the flow field is directly connected to the mixture fraction of the two flows. It is assumed that turbulent mixing of enthalpy and species are similar. For non-unity Lewis numbers the small scale mixing by diffusion and heat conduction differ, but on the scale of the thermocouple this difference is negligible [91]. The method was previously used by other groups [55, 81].

4.1.1 Setup

The setup of the measurement equipment is shown in figure 4.1. A temperature probe is inserted from the top into the flow channel. The probe is connected to a 3D traverse system which moves the probe in all spatial directions. The probe itself consists of 5 Type K thermocouples in a row with a distance of

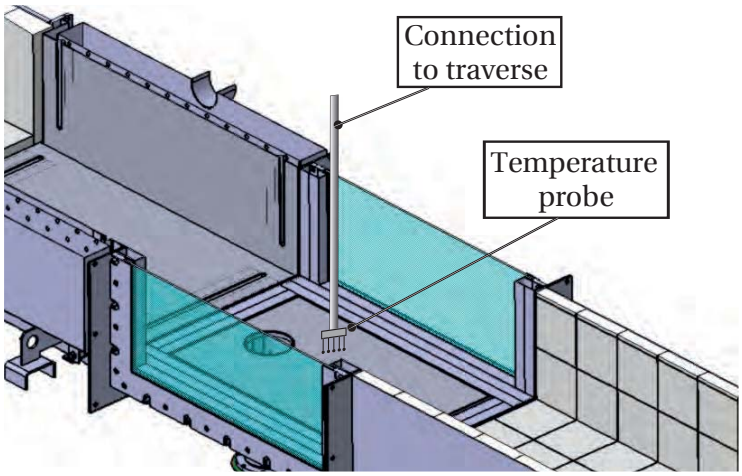

Figure 4.1: Scheme of the temperature probe in combustion chamber 2.

5 mm to each other to measure simultaneously at five positions. The junction of the wires has a diameter of 300 μm.

4.1.2 Data Processing

With a preheated jet and a cold cross flow it is possible to calculate the jet mixture fraction f at any given point in the measurement volume using equation 4.1:

$$f(x,y,z) = \frac{h_{mix}(x,y,z) - h_x}{h_j - h_x}. \tag{4.1}$$

$h_{mix}(x,y,z)$ is the enthalpy at the probe location, h_x the enthalpy of the cross flow, and h_j the enthalpy of the jet. The enthalpies area calculated from the respective temperatures and heat capacities.

The temperature is measured at about 15,000 points with a spatial resolution of 5mm for each investigated operation point. With a measurement time of 30 seconds at each point, the measurement time for one operation point is about 24h. The result is a 3D mean mixture fraction field which can be evaluated in various planes and along lines.

4.2 OH*-Chemiluminescence

In natural gas combustion four species emit relevant light intensities: C_2*, CH*, CO_2* and OH*. Several groups investigated chemiluminescence for combustion analysis purposes. Publications show that all four types of radical scale with the heat release rate q, but are also dependent on strain rate, preheating temperatures and pressure [65, 117]. Therefore, the chemiluminescence intensity does not scale one to one with the heat release rate. In this study the flame position is the most important information from the chemiluminescence images while the quantitative heat release rate is not of interest. Although the chemiluminescence intensity of the flame is attenuated by strain [80], the strain effect is weak and therefore the use of the data for lift-off and flame shape evaluation is assumed valid.

The experimental setup of the OH* chemiluminescence measurement is shown in figure 4.2. The OH* sensitive high-speed camera Photron FASTCAM-ultima APX I^2 with a 45 mm lens and a 307±5 nm bandpass filter is used. The camera has an integrated image intensifier to resolve weak light intensities and is placed normal to the x-z plane of the experiment in front of the windows of combustion chamber 2. The emitted light of the flame surface is then captured by the camera. The camera detects the line of sight integrated chemiluminescence of the flame front. The image intensifier of the camera is highly non-linear. This non-linearity was measured with a constant light source and all data was adjusted with the resulting calibration function, see Lauer [65] for details.

The captured images are processed to get information about flame position and shape. In figure 4.3 a scheme of the evaluation method is shown. The flame base is defined as the closest point of the flame to the injector, where 5% of the maximum OH* intensity is detected. The distance from the injector exit to this flame base is defined as lift-off height. The time average of 500 images is used to determine the lift-off height.

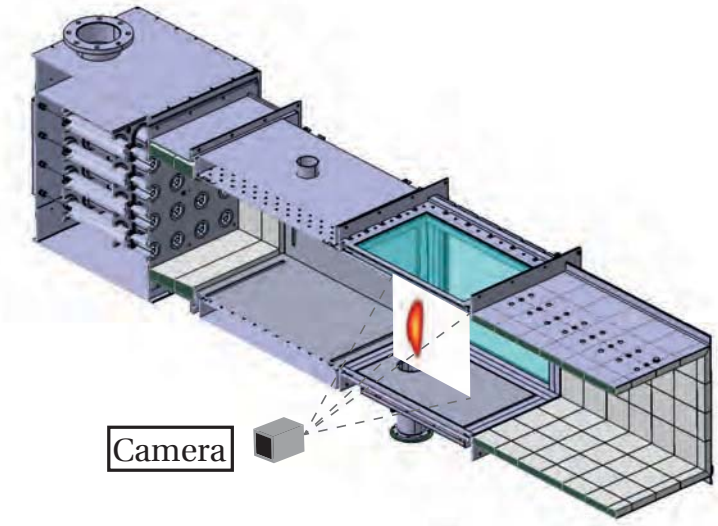

Figure 4.2: Position of the OH* camera equipment.

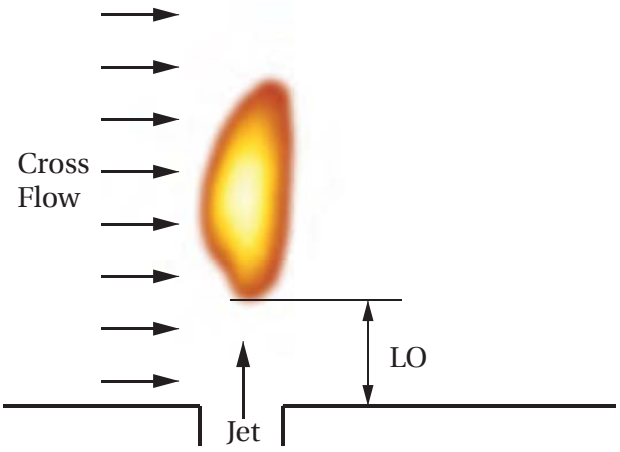

Figure 4.3: Method to measure the lift-off height from the OH* chemiluminescence images.

4.3 Particle Image Velocimetry Method

Particle image velocimetry is a common method to measure velocities of gaseous or liquid flows. To measure the velocities, seeding particles are added to the flow. The particles are illuminated with a laser and the scattered light is captured with a camera. The camera captures pairs of images at a certain time interval. Cross correlating the image pairs locally a local particle displacement can be obtained which, together with the time interval, gives the local velocity.

4.3.1 Setup

The laser used to illuminate the particles is a Litron LDY-304 high-speed laser with a cavity mean power of 30 W and a pulse energy of 30 mJ at 1 kHz. The camera is a Photron SAX which can capture up to 12,500 frames per second at full resolution. Figure 4.4 shows the setup of the camera and the laser sheet. The evaluated area is about 300 x 300 mm. The material of the seeding particles is TiO_2 and the mean size of the particles is 1 μm. The small size of the particles is necessary to ensure that they follow the turbulent flow. The TiO_2 material is able to withstand the temperatures in the flame front without melting.

4.3.2 Particle Following Behavior

If the inertia forces on the particles are too high, slip between particles and fluid falsifies the PIV measurements results. An indicator to evaluate slip is the Stokes number St which describes the influence of drag on particles in fluid flow:

$$\mathrm{St} = \frac{\tau_\mathrm{P}}{\tau_\mathrm{F}}, \tag{4.2}$$

where τ_P is the characteristic time of the particle. The timescale τ_F characterizes the flow field and is replaced by integral or Kolmogorov timescales which were calculated in section 2.1. The timescale of the particles, τ_P, is calculated based on the particle parameters and the flow conditions under the assumptions that the flow around the particle is laminar and only the inertia and drag

forces are important [93]:

$$\tau_P = \frac{d_P^2 \rho_P}{18 \eta_F}. \tag{4.3}$$

d_P represents the particle diameter, ρ_P the density of the particle and η_F the dynamic viscosity of the flow. For TiO_2 particles with 1 μm diameter which were used in the experiments, the given flow conditions the Stokes number can then be calculated:

$$St_t = \frac{\tau_P}{\tau_t} = 0.013 \ll 1. \tag{4.4}$$

$$St_\eta = \frac{\tau_P}{\tau_\eta} = 0.82 < 1. \tag{4.5}$$

In equation 4.4 the Stokes number for the turbulent timescale is calculated. The result is much smaller than unity and therefore the particles follow the macroscopic flow structures. The motions of the Kolmogorov scales have a much higher frequency which results in a higher Stokes number in equation 4.5. The Stokes number is still smaller than unity and a negligible slip can even be assumed for the Kolmogorov scales.

4.3.3 Data Processing

The recorded double images are processed with the Matlab tool PIVlab which uses a cross correlation scheme to calculate the shift of several particles in an interrogation area. The results are 2D matrices with the instantaneous velocity vectors in the x and z direction. The data is then further processed to calculate the mean velocities and turbulence intensities.

4.4 Mixture Field Analysis

The mixture field analysis utilizes the Mie scattering of seeding particles to calculate the mixture fraction of two mixing flows and to track the flame front. The method was used by other groups before for non-reacting flows [70, 108, 118]. Within this study the approach is extended to also resolve the

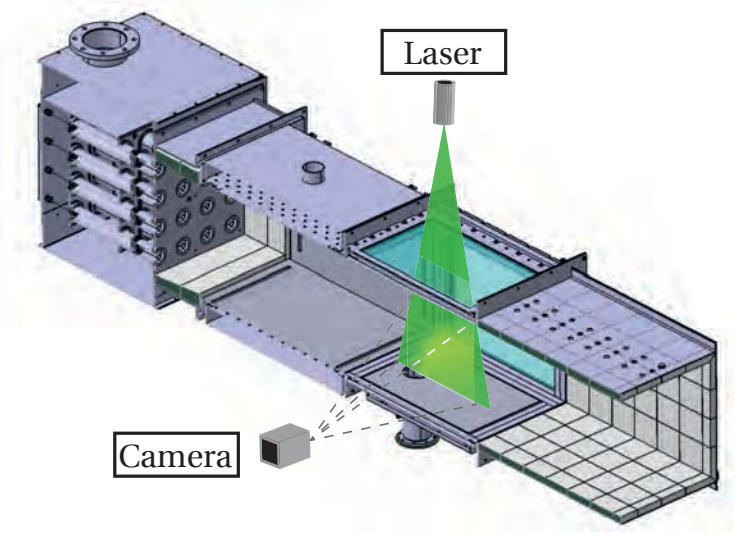

Figure 4.4: Particle image velocimetry/MixPIV setup to measure the flow velocities and the jet mixture fraction.

mixture field of reacting flows [61]. As it uses the same setup as the particle image velocimetry and allows the determination of the mixture it is called MixPIV in the following.

4.4.1 Setup

The measurement setup of MixPIV is equal to the PIV setup, see figure 4.4. The laser sheet of a Nd:YLF pulse laser enters the measurement section from top and illuminates the center plane. Only the jet is seeded with TiO_2 particles with 1 μm diameter and the cross flow must not contain any seeding particles. A camera with a bandpass filter (527 ± 5 nm) captures the scattered light.

In difference to the PIV setup reflections are critical, because the calculated mixture fraction depends on the light intensity. Therefore, reflections are minimized by coating of reflecting components. A non-uniform laser sheet and intensity fluctuations of the laser are corrected by the algorithm presented in the next section. Absorption is negligible by keeping the amount of seeding low enough.

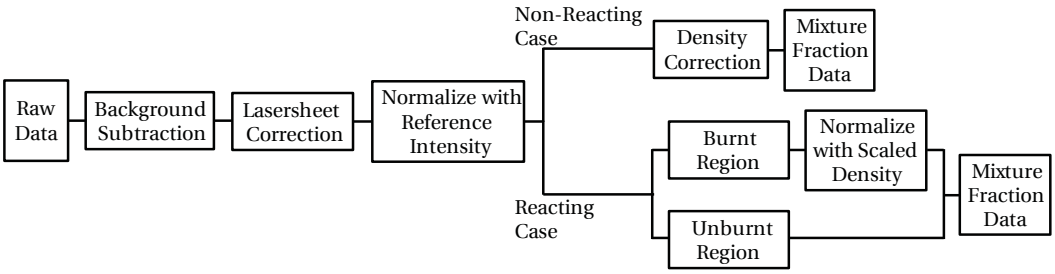

Figure 4.5: Scheme of the MixPIV algorithm.

4.4.2 The MixPIV Algorithm

The input of the MixPIV algorithm is an array of images of the seeded flow field. The following corrections of the measurements have to be performed to get reliable mixture fraction results:

1. Background subtraction
2. Laser sheet correction
3. Seeding density correction
4. Density correction

In equation 4.6 the four corrections are applied:

$$f(x,z,t) = \frac{I(x,z,t) - BG(x,z)}{I_{ref}(t)} LS(x,z) \frac{\rho_{ref}}{\rho(x,z,t)}, \tag{4.6}$$

where x and z describe the spatial coordinates and t the temporal resolution. f is the mixture fraction, I the light intensity of the raw picture, I_{ref} the light intensity at the reference point, BG the background image, LS the light sheet correction, ρ the fluid density and ρ_{ref} the fluid density at the reference point. A scheme of the algorithm is shown in figure 4.5.

The image of the flow without seeding is taken as the background image BG. It is then subtracted from the raw intensity of all images of a time series. Furthermore, images of the seeded cross flow are recorded and time-averaged to analyze the laser sheet non-uniformity and adjust the measurement data with this reference field. During the measurements a reference point in the jet

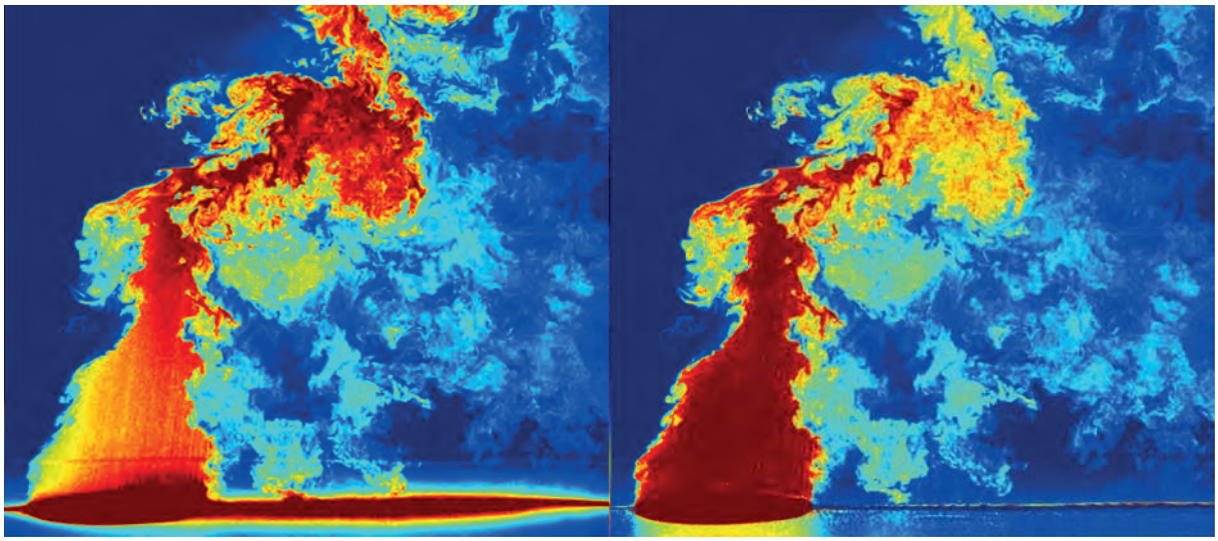

Figure 4.6: Example of light intensities of a raw (left) and processed image (right). Background subtraction, laser sheet correction and normalization with the reference point were applied.

core is defined where the mixture fraction is always f = 1. At this point the reference intensity I_{ref} is measured for every frame to adjust fluctuations of the laser power and the seeding density. The captured light intensities of the raw picture are divided by this reference intensity I_{ref}. The result of the corrections are presented in figure 4.6 which shows the differences between a raw and a processed image.

For cases with different densities of the two flows, the density of the mixture has to be taken into account which is calculated as a function of the mixture fraction f. The density ρ at any point is expressed as function of I and the initial densities of the two mixing flows as proposed in [97].

Images from reacting cases need additional processing due to the density change along the flame front. The density change causes a drop of the scattered light intensity I, but the mixture fraction f does not change over the reaction. The flame front is detected through the density change and the unburnt as well as burnt regions are treated separately to avoid deviations in the mixture analysis. The only difference for the two regions is that the reference intensity I_{ref} is scaled by the ratio of the densities before and after the flame front. All other corrections are equal to the non-reacting cases. Details on the method are found in [61].

4.4.3 Validation for the Cold Case

For the validation of the MixPIV algorithm non-reacting cases are considered first. The mixture field is measured in the symmetry plane x-z, using the MixPIV method and by point wise temperature measurements presented in the previous section 4.1. The quantitative comparison is made along the z-axis at y = 0 and different x coordinates in figure 4.7. The results show that the agreement between the two measurement techniques is very good.

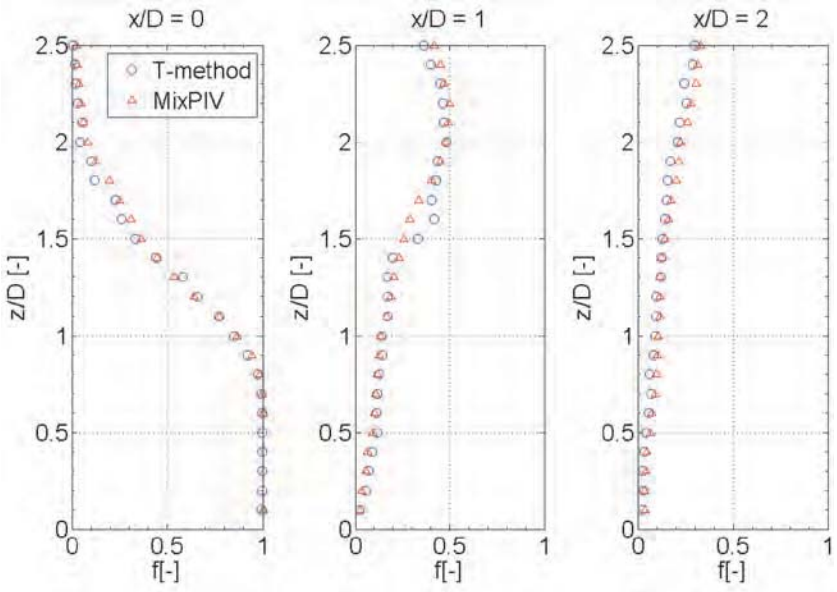

Figure 4.7: Quantitative comparison of the results of temperature and MixPIV method.

4.4.4 Results for the Reacting Case

In comparison to the non-reacting cases the density drop over the flame front has to be taken into account for reacting cases. One processed instantaneous image of a reacting jet at a momentum ratio J = 4, jet equivalence ratio of ϕ = 0.77, and cross flow equivalence ratio of ϕ = 0.5 is shown in figure 4.8. The flame front, marked with a white line, is found by the algorithm utilizing the density drop. The mixture fraction does not change over the flame front, which shows that the density compensation of I_{ref} works well. The noise in the data is the result of the density drop over the flame front and therefore the reduction of the light intensity. However, the method gives qualitative, time and spatial resolved information about the mixture field.

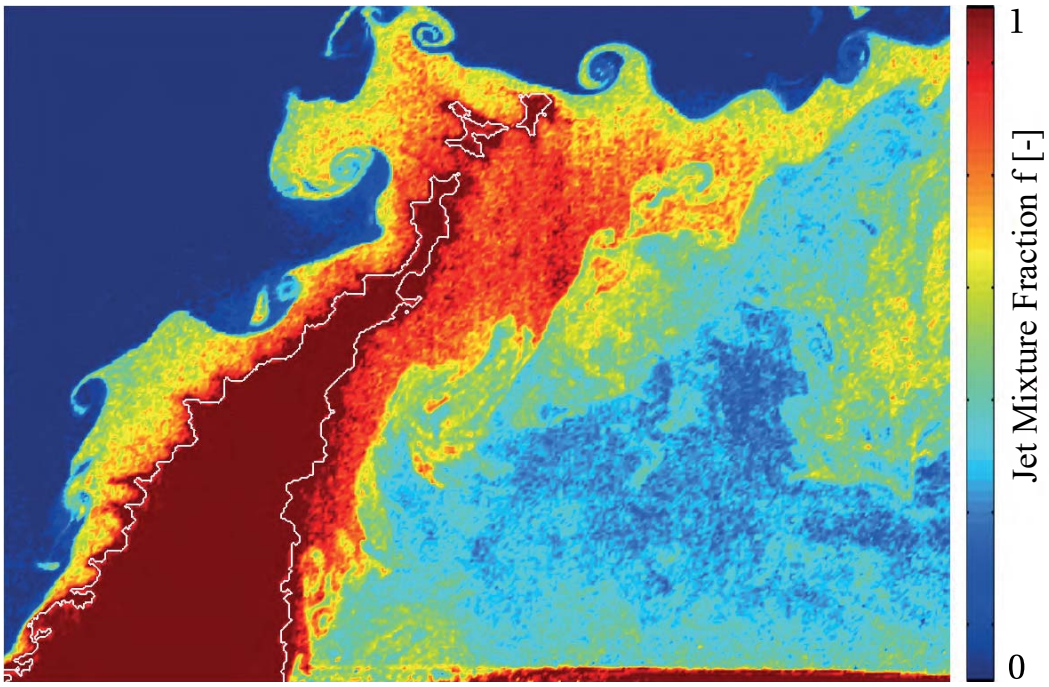

Figure 4.8: MixPIV data in the center plane for the reacting jet. The flame front is marked by the white line.

4.5 Emission Analysis

A emission analyzing system is used to measure the CO, CO_2, O_2, and NO_x species concentrations. From the raw data the equivalence ratio as well as the NO_x concentrations corrected to 15% O_2 are calculated. A water cooled, cranked probe is attached to a traverse and moved to different measurement positions to obtain the local emission concentrations. The water cooling allows measurements within the flame front and the cranked tip improves the spatial accuracy. Furthermore, cooling quenches the reaction in the sampled gas which is especially important with respect to the CO and NO_x concentrations. The pipe which transports the exhaust gas from the probe to the analyzer is heated to 105°C to prevent condensation. When the exhaust gas enters the analysis unit, the flow is divided into two paths. The first path goes directly to the NO_x analyzer. The NO_x concentration is measured in the wet exhaust gas, because NO_x is soluble in water and a condensation would distort the results. The measurement principle is based on the chemiluminescence of NO molecules which are oxidized to NO_2. The gas for measurement of all other species flows through the second path in which all water is removed by a condenser. The O_2 concentration is then measured using the paramagnetic properties of the molecule. The CO and CO_2 species are measured using infrared absorption detectors.

4.5.1 Mixture Fraction Based on Oxygen Content

It is possible to calculate the mixture fraction of jet material in the cross flow based on the O_2 content. The O_2 content at the inlet of jet and cross flow is equal to the O_2 content in the ambient air. Depending on the equivalence ratio a certain amount of O_2 is combined to CO_2 and H_2O . The equivalence ratio for each flow is known and therefore the O_2 content after the reaction zone is calculated. It is then possible to determine the jet mixture fraction from measured $O_{2,\mathrm{measured}}(x,y,z)$ concentrations at any point downstream of the reaction zone:

$$f(x,y,z) = \frac{O_{2,\mathrm{measured}}(x,y,z) - O_{2,j}}{O_{2,x} - O_{2,j}}. \tag{4.7}$$

4.5.2 Normalized Emission Values

The NO_x emissions are normalized to 15% O_2 standard condition. Since the measurements here are made for wet exhaust gas, this has to be taken into account. Turns [115] provides a detailed calculation of normalized NO_x values from raw NO_x measurements. The equation to normalize the measured amount of NO_x to an equivalent value at 15% O_2 is:

$$NO_{x,\text{dry at } 15\,\%\,O_2} = NO_{x,\text{wet}} \cdot \frac{v_{min} + l_{min}\left(1/\phi - 1\right)}{v_{min,\,dry} + l_{min}\left(1/\phi_{0.66} - 1\right)} \,. \tag{4.8}$$

ϕ is the measured equivalence ratio, $\phi_{0.66}$ is the equivalence ratio with 15% O_2 in the exhaust gas, l_{min} is the minimal amount of air required for complete combustion of the reactants, v_{min} is the minimal amount of exhaust gas, $v_{min,dry}$ is the minimal amount of exhaust gas without water and $NO_{x,wet}$ the amount of measured NO_x in the wet flow. The v_{min} and l_{min} values are specific for the fuel and are published by the natural gas supplier [111].

5 Influence of Jet Nozzle Geometries on the Flow Field

The influence of different jet nozzle geometries on the velocity and mixing field of jets in cross flow has not been broadly discussed in literature, yet. In particular no general correlations have been proposed that allow the dimensioning and scaling of such systems. In this chapter the results obtained from measurements performed for this study are shown and discussed. Based on these measurements, a model is derived to predict the length of the potential core of jets in cross flow which is crucial to understand the mixing process. Furthermore, a trajectory correlation for different nozzle geometries is presented and the concentration decay depending on the jet nozzle geometry is evaluated. Afterwards, the results of the non-reacting investigations are used to model the mixing fields of reacting cases. At the end of the chapter NO_x emission measurements are shown to identify similarities of non-reacting mixture fields and NO_x formation.

5.1 Results of Non-Reacting Cases

The mixture fraction results obtained with the temperature method allow the complete reconstruction of the mean mixture field of the jet in cross flow. An overview of the flow field in the symmetry plane with the important features is given in figure 5.1. Two coordinate systems are often used in literature, see section 2.4 for details. The first one is an absolute system, x,y,z, and the second one is a relative system, ξ, ζ, η. Here, the relative coordinate system follows the path of the highest jet concentration starting from the middle of the jet nozzle exit. The region where no cross flow material is entrained is called core. The penetration depth is the the distance from the bottom of the channel to the trajectory at the point where the trajectory becomes parallel to the cross flow. The lower and upper boundary confine the spread of the jet material in the

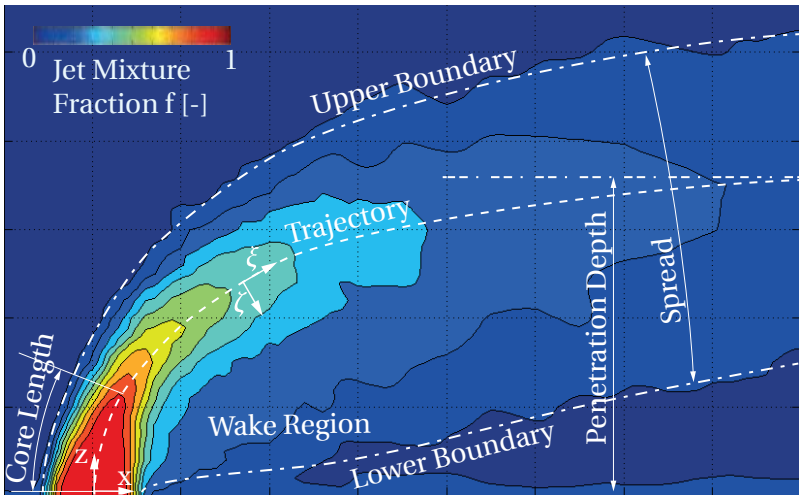

Figure 5.1: Overview of the mixture field of non-reacting jets in cross flow.

cross flow.

The time-averaged measured mixture fields of different jet nozzle geometries in the symmetry plane are shown in figure 5.2 for a momentum ratio of J = 15. The results of configuration P are similar to the data of circular jets in cross flow found in literature [50,55,69]. The configurations S2 and T2 penetrate less compared to the other configurations and both have an increased spread. Circular jets with lower momentum ratios and therefore lower penetration depth show a similar spread. The decreased distance of jet to the lower wall increases the mass transport in the wake region due to the different pressures of lower wall boundary layer and the jet core. For higher momentum ratios and therefore higher penetration depths the mixing in the wake region reduces. The configurations with the deepest penetration depths S1 and T1also have the lowest spread and the wake with the lowest amount of jet material. The penetration depth of configuration P is in between and also shows a spread smaller than S1, T1 and higher than S2, T2. A comparison of the mixture trajectories is shown in figure 5.3. Gutmark [39] investigated the same five nozzle configurations and found the same order of penetration depths for velocity trajectories.

The analysis of mixture fields in a y-z plane further downstream at $z/D_j = 12$ was presented by Salweski et al. [94]. They found the peak jet mixture fraction for configurations similar to P, S1 and S2 to be equal. However, similar to the results of this thesis, the distribution of the mixture in the evaluation plane is dominated by the CVP.

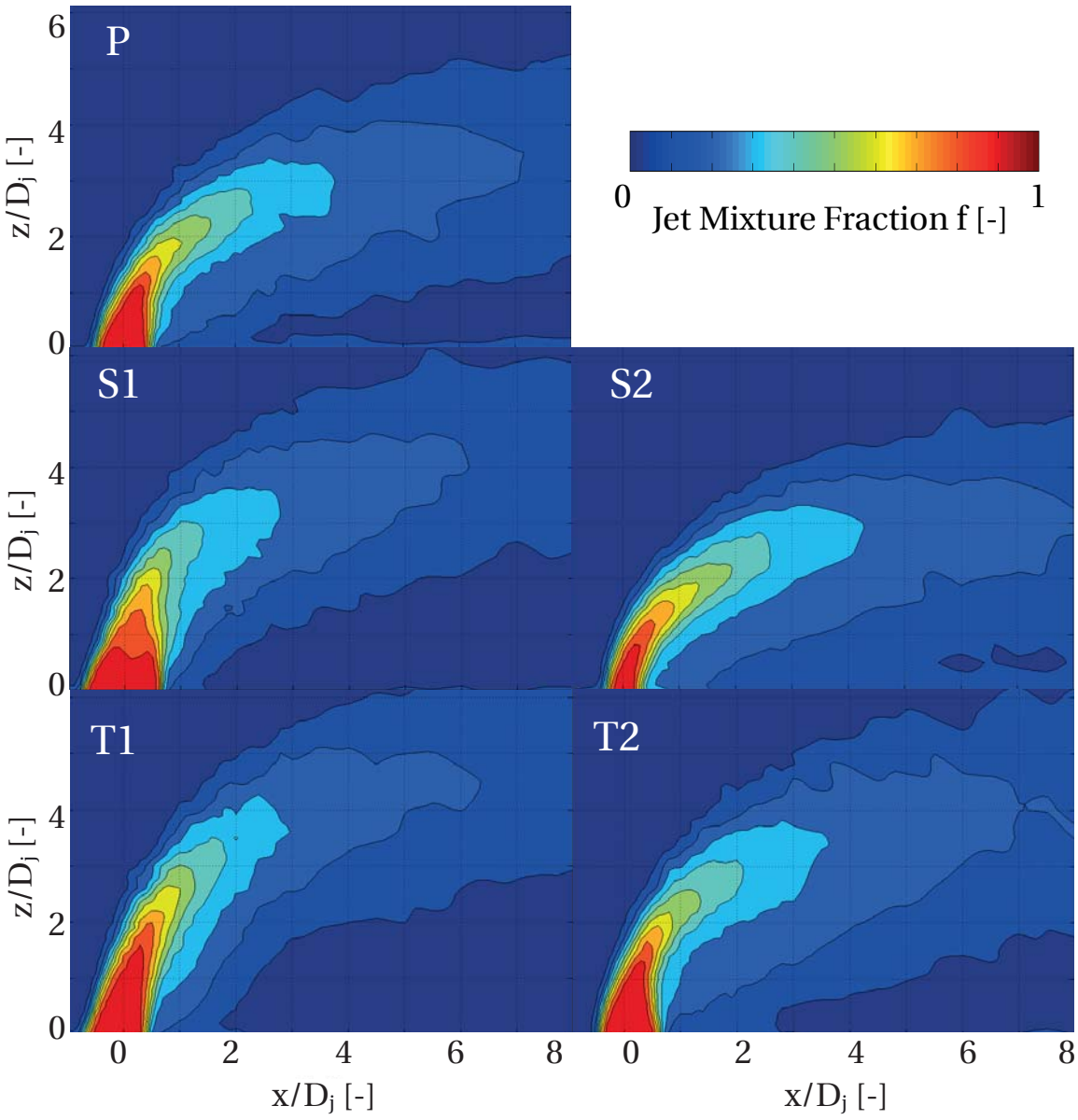

Figure 5.2: Time-averaged jet mixture fraction fields of the different jet nozzle configurations in the x-z plane at y=0, J=15, non-reacting, $D_j = 50\,mm$.

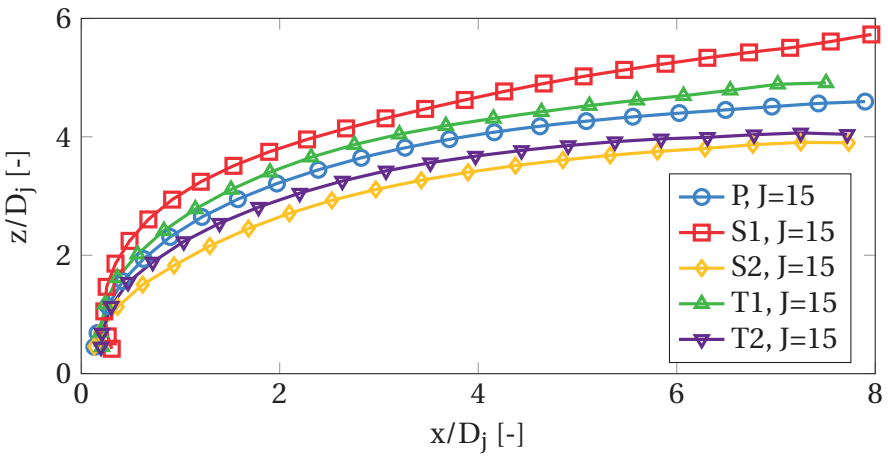

Figure 5.3: Mixture trajectories of different jet nozzle configurations.

Based on the measurements presented here models for the mixture trajectory and the concentration decay along the mixture trajectory are proposed in the next section.

5.2 Analytical Model for Non-Reacting Jets in Cross Flow

Analytical models of jets in cross flow are found in literature [44]. However, the available models are focused on high momentum ratios and the far field of the jet. In this section a model based on turbulent free jet theory for moderate momentum ratios and the near field of the jet is derived and subsequently validated against measured data.

5.2.1 Potential Core

The length of the potential core of a turbulent free jet is independent of the jet velocity and depends only on the jet diameter. However, in the jet in cross flow configuration the length of the potential core is found to depend also on the momentum ratio J. In this section it is shown that the influence of the momentum ratio can be considered using elements from free jet theory. Figure 5.4 shows a scheme of the near field around the potential core of a circular free jet, where $\dot{m}_0$ is the initial mass flow, u_j the initial jet velocity, l_{PC} the length of the potential core, $\dot{m}_1$ the mass flow and u_1 the velocity at the end of the po-

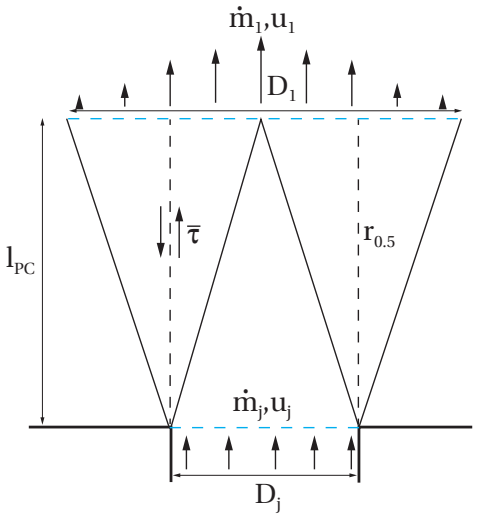

Figure 5.4: Scheme of the potential core region of a turbulent free jet.

tential core, $r_{0.5}$ the center of the shear layer, and $\bar{\tau}$ the time averaged turbulent shear stress.

The vertical momentum conservation equation for the shown control volume gives:

$$\dot{I} = \dot{m}_j u_j = \dot{m}_1 u_1 \tag{5.1}$$

$$\dot{m}_j = u_j \frac{\pi}{4} D_j^2 \rho_j \tag{5.2}$$

$$\dot{m}_1 = u_1 \frac{\pi}{4} D_1^2 \rho_j. \tag{5.3}$$

Assuming a similar angle for the inner and outer boundary of the shear layer, the diameter of the flow has doubled at the end of the potential core:

$$D_1 = 2D_j. \tag{5.4}$$

Substitution of diameter D_1 with $2D_j$ in equation 5.1 leads to:

$$4\frac{\pi}{4} D_j^2 \rho_j u_1^2 = \frac{\pi}{4} D_j^2 \rho_j u_j^2. \tag{5.5}$$

Solving for u_1 yields:

$$u_1 = 0.5 u_j. \tag{5.6}$$

This means that the mass flow at the end of the potential core $\dot{m}_1$ has doubled compared to the mass flow at the jet exit $\dot{m}_j$. The momentum which entrains additional fluid through turbulent shear stress is estimated according to literature [89]:

$$\frac{\dot{I}}{2} = \dot{m}_j \frac{u_j}{2} = \bar{\tau} U_{circ} l_{PC}. \tag{5.7}$$

$\bar{\tau}$ is the mean turbulent shear stress, l_{PC} the length of the potential core and $U_{circ} = \pi D_j$ the perimeter of the $r_{0.5}$ contour.

The mean turbulent shear stress along $r_{0.5}$ is approximated as proposed by [87]:

$$\bar{\tau} = \rho_j \nu_t \bar{S}. \tag{5.8}$$

ν_t is the eddy viscosity and $\bar{S}$ the mean shear rate which is approximated with a quotient of the initial jet velocity and the width of the shear layer at the end of the potential core:

$$\bar{S} \approx \frac{u_j}{D_j}. \tag{5.9}$$

Inserting equations 5.2, 5.8 and 5.9 and into 5.7 results in:

$$\rho_j \nu_t \frac{u_j}{D_j} D_j \pi l_{PC} = \rho_j D_j^2 \frac{\pi}{4} \frac{1}{2} u_j^2. \tag{5.10}$$

Solving for l_{PC}/D_j yields:

$$\frac{l_{PC}}{D_j} = \frac{u_j^2}{8 \nu_t \bar{S}} = \frac{u_j D_j}{8 \nu_t}. \tag{5.11}$$

With an estimated length of the potential core of $l_{PC}/D_j = 6.57$ from literature [2], the eddy viscosity in the shear layer is calculated:

$$\nu_t = \frac{D_j}{8 l_{PC}} u_j D_j = \frac{D_j}{8 \cdot 6.57 D_j} u_j D_j = 0.019 u_j D_j. \tag{5.12}$$

This is compared with the eddy viscosity value in the self-similar region found in literature [2]:

$$\nu_t = 0.014 u_j D_j. \tag{5.13}$$

Considering the simplicity of the integral ansatz the agreement is good and indicates that the proper physics are captured.

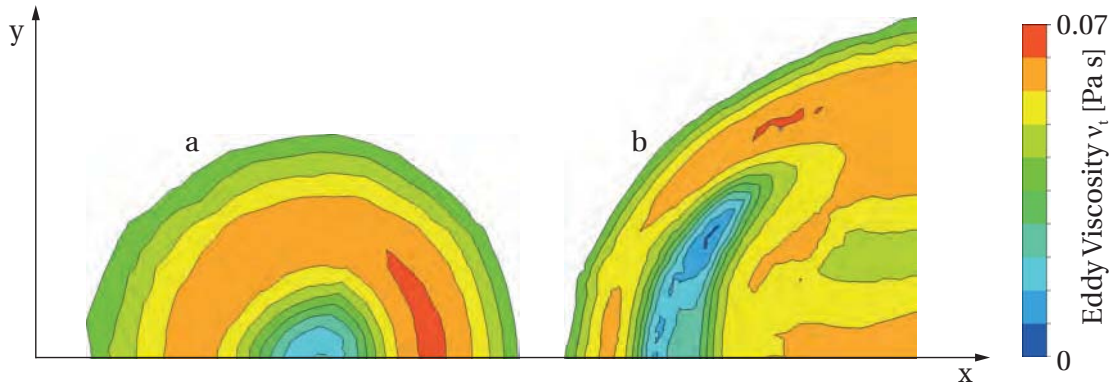

Figure 5.5: Comparison of the eddy viscosity of a free jet (a) and a jet in cross flow J = 15 (b) in the x-y plane at the end of the potential core.

In the next step the cross flow is added to the problem to model the jet in cross flow. Simple numerical Reynolds-averaged Navier-Stokes (RANS) simulations were carried out to get information on the eddy viscosity of free jets compared to jets in cross flow. The simulations are steady-state, incompressible, without combustion reaction, pressure based, the turbulence model is k-ϵ and the jet velocity in the nozzle is equal for both cases.

In figure 5.5 the eddy viscosity from simulations of a free jet and of a jet in cross flow are shown. Although the distribution of the eddy viscosity is very different for the two configurations, the values in the shear layers are almost equal. The much higher velocity of the jet compared to the cross flow for momentum ratios $J \gg 1$ dominates the eddy viscosity.

The experimental data as well as literature [72] show that the potential core of a jet in cross flow is shorter than the potential core of a free jet. This means that the mean shear stress (see equation 5.8) is larger for jets in cross flow. Since the eddy viscosity is hardly affected by the cross flow, the enhanced shear stress must have another reason. A reasonable explanation could be the deformation of the jet shear layer which increases the mean stress rate $\bar{S}$.

The cross flow pushes the windward jet boundary downstream and thereby distorts the jet. The areas of the jet mixture fraction fields of free jet and jet in cross flow in figure 5.6 are almost equal, but the width from the jet core to the outer boundary, i.e. the shear layer thickness, is smaller for the jet in cross flow. The decreased width causes higher velocity and concentration gradients. The width of the jet in the symmetry plane is estimated by assuming that the

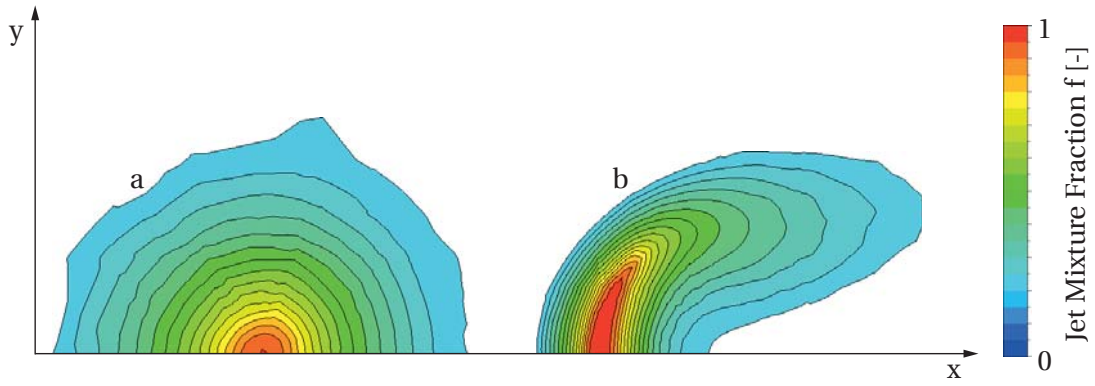

Figure 5.6: Comparison of the mixture field of a free jet (a) and a jet in cross flow J = 15 (b) in the x-y plane at the end of the potential core.

windward shear layer gets pushed towards the jet center with the velocity of the cross flow u_x while the jet material moves perpendicular to it:

$$d_c = D_j \left(1 - \frac{u_x}{D_j} t_{l_{PC}}\right). \tag{5.14}$$

d_c denotes the mean width of the jet over the length of the potential core, D_j the initial diameter, u_x the cross flow velocity, and $t_{l_{PC}}$ the mean time until the end of the potential core is reached (assuming the velocity on the center line is u_j, the velocity in the outer shear layer is zero). This time of flight $t_{l_{PC}}$ from the nozzle exit to the end of the potential core is approximated for a linear velocity distribution:

$$t_{l_{PC}} = \frac{l_{PC}}{0.5 u_j}. \tag{5.15}$$

The velocity of the jet u_j has to be much higher than the cross flow velocity u_x, because else the jet thickness d_c could become negative which would be unphysical. The shear rate of the free jet (equation 5.9) is extended with the reduced jet width d_c to model the shear rate of the jet in cross flow:

$$\bar{S}_{ext} = \frac{u_j}{d_c} = \frac{u_j}{D_j} \frac{1}{1 - \frac{u_x}{D_j} \frac{2 l_{PC}}{u_j}}. \tag{5.16}$$

The extended shear rate can then be inserted into equation 5.11 which de-

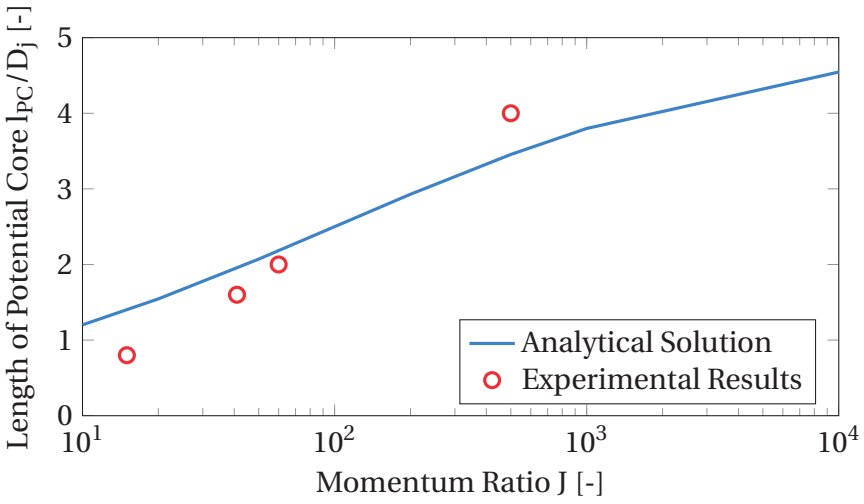

Figure 5.7: Length of potential core of a circular jet as predicted by equation 5.18 in comparison to experimental data of this study.

scribes the potential core length:

$$\frac{l_{PC}}{D_j} = \frac{u_j^2}{8\nu_t \bar{S}} = \underbrace{\frac{u_j^2}{8\nu_t \frac{u_j}{D_j}}}_{l_{PC,0}/D_j} \left(1 - \frac{u_x}{u_j}\frac{2l_{PC}}{D_j}\right). \tag{5.17}$$

The substitution with $l_{PC,0}/D_j$ and $u_x/u_j = 1/\sqrt{J}$ in 5.17 results in:

$$\frac{l_{PC}}{D_j} = \frac{l_{PC,0}}{D_j} - \frac{l_{PC,0}}{D_j}\sqrt{\frac{1}{J}}\frac{2l_{PC}}{D_j}. \tag{5.18}$$

Solving for l_{PC}/D_j leads to an equation which describes the length of the potential core as a function of the momentum ratio J:

$$\frac{l_{PC}}{D_j} = \frac{l_{PC,0}}{D_j}\frac{1}{1 + 2\frac{l_{PC,0}}{D_j}\sqrt{\frac{1}{J}}}. \tag{5.19}$$

Figure 5.7 shows the influence of the momentum ratio on the potential core length as predicted by equation 5.19. For an infinite momentum ratio the potential core length of the jet in cross flow becomes equal to the potential core length of a free jet. For low momentum ratios the length becomes zero. The comparison to the experimental data shows the same limits but a discrepancy in the steepness of the curves.

This discrepancy is explained with the perimeter of the shear surface which is calculated with the constant perimeter of a circle in equation 5.10. The RANS simulations as well as experimental data show that the flow field of the jet becomes kidney shaped. This means that the change of perimeter causing an increased shear surface is missing in the model.

From the RANS simulation it is known that the area of the kidney is almost equal to the predicted area of a free jet at the end of the potential core. The area within the $r_{0.5}$ radius is approximated by an ellipse:

$$A_{circle} \approx A_{ellipse} = \frac{D_j^2 \pi}{4} = a_{ell} b_{ell} \pi. \tag{5.20}$$

a_{ell} is the semi-minor axis and b_{ell} the semi-major axis. Directly at the jet outlet no deformation has occurred. So the axis a_{ell} at this location is equal to half of the diameter of the jet $D_j/2$. When traveling downstream the jet is distorted by the cross flow. Based on the results of the RANS simulation the semi-minor axis a_{ell} is deformed equally as the width of the potential core d_c. Similar to equation 5.14 the semi-minor axis a_{ell} is described with equation 5.21.

$$a_{ell} = \frac{D_j}{2}\left(1 - \frac{u_x}{D_j} t_{l_{PC}}\right). \tag{5.21}$$

Given a_{ell} the semi-major axis b_{ell} is calculated based on equation 5.20:

$$b_{ell} = \frac{D_j^2}{4} \frac{2}{D_j\left(1 - \frac{u_x t_{l_{PC}}}{D_j}\right)} = \frac{D_j}{2} \frac{1}{1 - \frac{1}{\sqrt{j}} 2 \frac{l_{PC}}{D_j}}. \tag{5.22}$$

Though the perimeter of an ellipse cannot be calculated with a simple elementary equation an approximation is available:

$$U_{ell} \approx (a_{ell} + b_{ell})\pi. \tag{5.23}$$

With equations 5.21, 5.22 and 5.23 the perimeter is calculated based on the jet

diameter, the cross flow velocity and the length of the potential core:

$$U_{ell} = \pi \frac{D_j}{2} \left[\left(1 - \frac{u_x}{u_j} \frac{2l_{PC}}{D_j} \right) + \frac{1}{1 - \frac{u_x}{u_j} \frac{2l_{PC}}{D_j}} \right]. \tag{5.24}$$

Finally, the perimeter of the ellipse is set in relation with the perimeter of a circle to get a factor for the change of the perimeter:

$$s = \frac{U_{ell}}{U_{circ}} = \frac{1}{2} \left[\left(1 - \frac{u_x}{u_j} \frac{2l_{PC}}{D_j} \right) + \frac{1}{1 - \frac{u_x}{u_j} \frac{2l_{PC}}{D_j}} \right]. \tag{5.25}$$

According to the RANS simulations the change of the perimeter is somewhat smaller than predicted by equation 5.25 and therefore has to be corrected with a empirical-factor g. The final equation to describe the length of the potential core is given by:

$$\frac{l_{PC}}{D_j} = \frac{\frac{l_{PC,0}}{D_j} \frac{1}{1+2\frac{l_{PC,0}}{D_j}\sqrt{\frac{1}{J}}}}{g \cdot s}. \tag{5.26}$$

The empirical parameter g = 0.8 is determined by fitting equation 5.26 to the experimental data. The fact that the correction factor is of order 1 gives confidence that the physics are still captured properly by the model. A comparison of the experimental data and the analytical model shows excellent agreement in figure 5.8 and the enhancement compared to the previous model in figure 5.7.

In a next step the model is extended to capture the influence of the jet nozzle geometry on the potential core length. Literature [101] found that the length of the potential core scales with the width parameter h_0 which describes the diameter for circular nozzles or the width for slot nozzles. For equilateral triangles h_0 corresponds to the height of the triangle. No general rule to determine h_0 for complex nozzle geometries are found in literature so far [76].

Equation 5.27 predicts the length of the potential core as a function of the

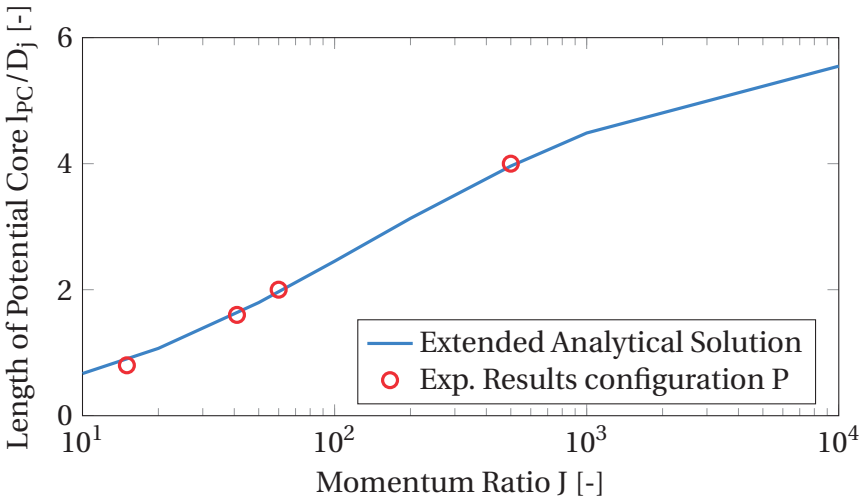

Figure 5.8: Length of potential core of a circular jet as predicted by equation 5.26 in comparison to experimental data.

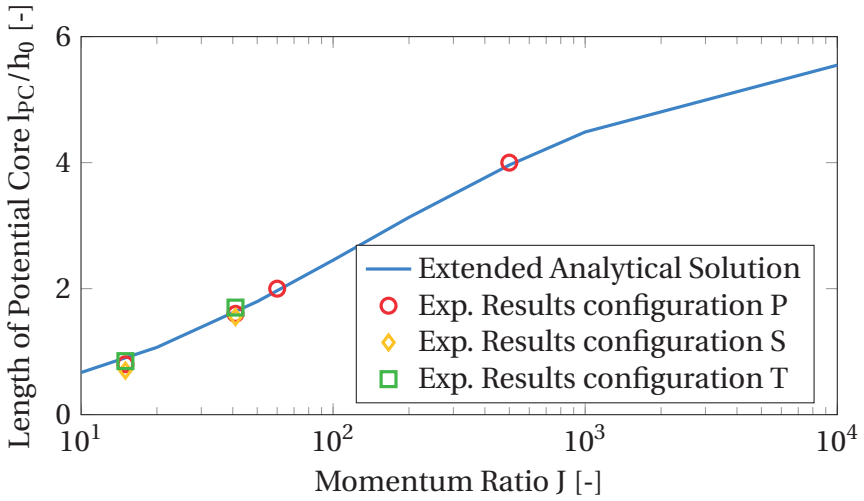

Figure 5.9: Length of potential core as predicted by equation 5.27 in comparison to experimental data of different jet nozzle geometries.

momentum ratio and the width parameter of the nozzle geometry.

$$\frac{l_{PC}}{h_0} = \frac{\frac{l_{PC,0}}{h_0}\frac{1}{1+2\frac{l_{PC,0}}{h_0}\sqrt{\frac{1}{J}}}}{g \cdot s}. \tag{5.27}$$

A comparison of results from equation 5.27 and experimental results is shown in figure 5.9, very good agreement can be seen. The width of the nozzle h_0 in equation 5.27 is independent of the alignment of the jet nozzle to the cross

flow. This independence of the potential core length from the alignment of the nozzle corresponds with the potential core lengths shown figure 5.2 at the beginning of this chapter.

In conclusion, it was found that the the potential core length of jets in cross flow depends on momentum ratio J and the width h_0 of the jet nozzle. An influence of the nozzle orientation on the potential core length is not observed.

5.2.2 Trajectories

As shown in the theory part 2.4.3 no generally applicable model is available in literature to predict the trajectories of jets in cross flow with various jet nozzle geometries. However, the relatively new model of Forliti [28] is able to predict jet trajectories for a wide range of momentum ratios very accurately for circular jets. His model combines two main influences on the trajectory path, the drag and the entrainment with the drag coefficient C_D and the entrainment coefficient c_{ej}, respectively (see equation 2.41). These coefficients are also suitable to model the trajectories of jets with different nozzle geometries. Based on literature [28, 36, 38], the influence of the jet nozzle shape on the entrainment coefficient c_{ej} is assumed to be small and therefore constant for all tested nozzles. Drag coefficients originally quantify the resistance of solid bodies to a flow. As proposed in literature [2, 16, 28] the drag coefficient is used to quantify the exchange of momentum of jet and cross flow in the jet in cross flow context. The drag coefficient of solids $C_{D,solid}$ is determined from experiments or numerical simulations. Results for solid bodies with the shape of the jet nozzle geometries used in this work are found in literature [25]. Like for solid bodies, the drag coefficient of the jet C_D is strongly influenced by the jet shape and alignment. The main difference to solid bodies is the deformation of the jet and therefore the change of shape. Forliti [28] found that the expansion of the jet causes an increased drag coefficient of the jet compared to a solid body. He determined the drag coefficient of the jet by fitting it until equation 2.41 correlates experimental trajectories from literature onto one curve.

To correlate trajectories from different jet nozzle geometries their drag coefficients have to be determined. Table 5.1 shows normalized drag coefficients C_D which are determined by fitting C_D until the results of equation 2.41 correlate

with the measurements. The normalized drag coefficients for corresponding solid bodies $C_{D,solid}$ [25] are also shown. As predicted by Forliti the experimentally determined drag coefficients are always higher compared to the drag coefficients of the solid bodies. Approaches to calculate the the drag coefficient from geometry parameters showed deviations, especially for the triangle geometries. That is why in this thesis the drag coefficients C_D are obtained by fitting equation 2.41 to the experimental results.

The entrainment and drag coefficients are assumed constant for all momentum ratios as proposed by Forliti. Figure 5.10 shows experimental data for the tested nozzles and momentum ratios of J = 15 and J = 42. The data in the left plot is only normalized with the jet diameter, while the right plot is additionally normalized with Forlitis' drag-entrainment coefficient B. For the latter the data lies on one curve.

Based on Forlitis' coefficient B a mixture trajectory correlation is derived:

$$\frac{z}{D_j B} = A\left(\frac{x}{D_j B}\right)^C, \tag{5.28}$$

where A = 0.7 and C = 0.35. The main difference to existing trajectory correlations in literature is Forlitis' parameter B which takes drag and entrainment into account.

Jet Nozzle	$C_D/C_{D,max}$	$C_{D,solid}/C_{D,max}$	$C_D/C_{D,solid}$	c_{ej}
P	0.68	0.4	1.7	0.32
S1	0.48	0.28	1.7	0.32
S2	1	0.76	1.3	0.32
T1	0.52	0.52	1.0	0.32
T2	0.8	0.68	1.2	0.32

Table 5.1: Drag and entrainment coefficients to model the jet trajectory from different jet nozzle geometries.

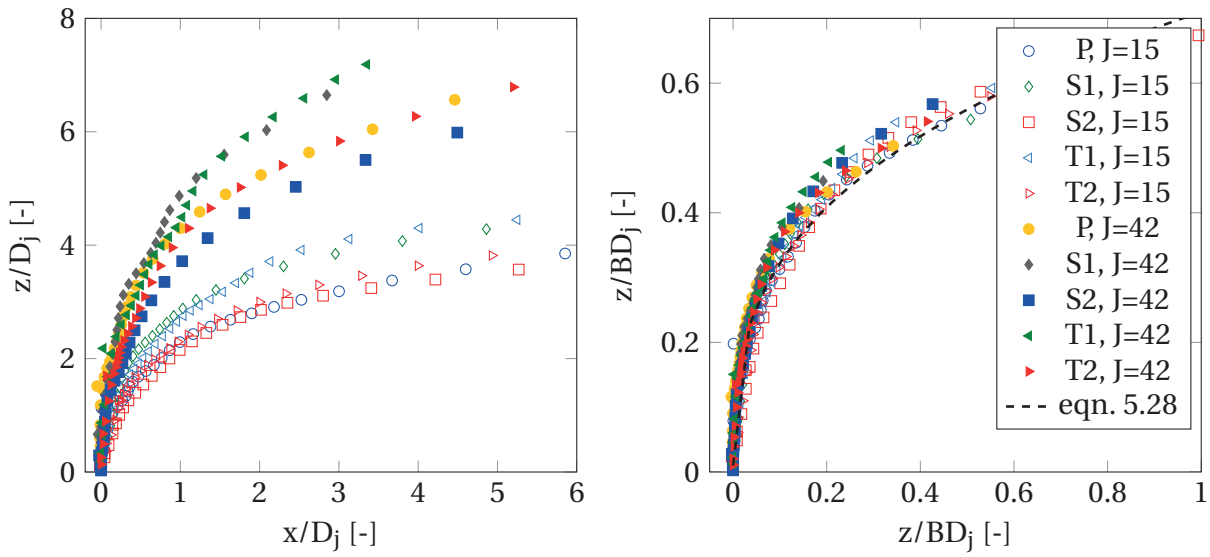

Figure 5.10: Mixture trajectories for cases with different momentum ratios and nozzle geometries. Left: Normalized with the jet diameter D_j. Right: Normalized with the diameter D_j and the drag-entrainment coefficient B.

5.2.3 Concentration Decay

The formation of nitric oxides is directly correlated with the local fuel-air ratio and thus to the local jet concentration. In this section a new model of the concentration decay will be presented and validated. For free jets it is common to plot the concentration decay against the axial jet axis. The axial decrease is a measure of how the jet mixes with the entrained flow. For jets in cross flow a comparable approach is to plot the concentration decay against the coordinate of the jet mixture trajectory ξ. In figure 5.11 the measured concentration decay of the tested configurations are shown. The different length of the potential core of the nozzles is visible. The configurations with the shortest potential core, namely S1 and S2, mix faster close to the nozzle. However, the slope of the concentration decay of S2 is flatter compared to the triangle configurations after the potential core which means that the mixing process is slower. Consequently, the jet concentration of S2 is only lower in the beginning due to the shorter potential core and the other configurations show improved mixing further downstream. S1 has a steeper slope and mixes best in the complete analyzed flow area. It is still important to note that the slope of the S1 configuration decreases faster than the slope of the other nozzle geometries. This is similar to the observation of the momentum ratio influence

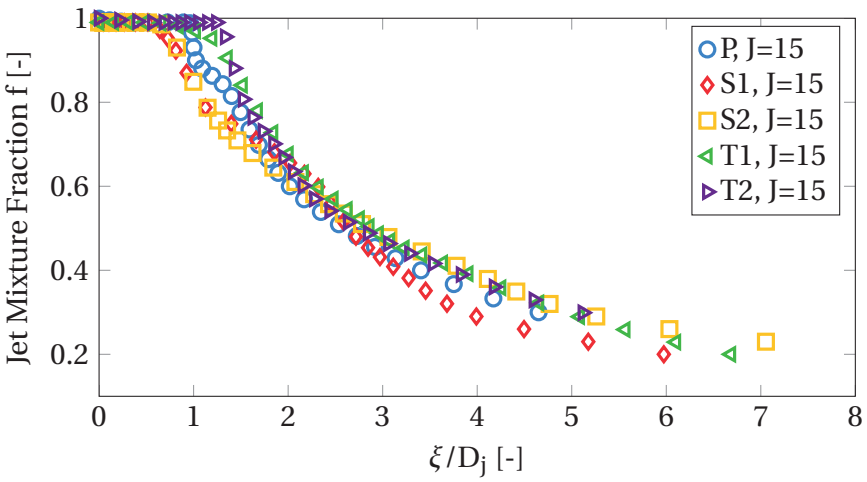

Figure 5.11: Measurements of the concentration decay of jets from different nozzle configurations along the jet mixture trajectory ξ.

presented in section 2.4.4. Jets with higher momentum ratios mix worse close to the injector and better further downstream. Transferred to the nozzle geometries this implies that jets with equal potential core length show a similar mixture fraction development close to the nozzle independent of the jet shape. Still, it is notable that the S1 configuration shows the lowest jet mixture fraction on the jet mixture trajectory for the measured range of ξ/D_j. This cannot be explained only with the potential core length. A possible explanation is the increased shear surface parallel to the cross flow. However, in this work no convincing mechanism was found to describe the improved mixing of the S1 configuration.

Starting from the concentration decay model of turbulent free jets [89], which is the asymptote for very high momentum ratios, the concentration decay of jets in cross flow after the potential core ($\xi > l_{PC}$) is modeled as:

$$f(\xi) = \frac{a}{\xi^b}, \text{ for } \xi > l_{PC}, \tag{5.29}$$

with

$$a = \sqrt{l_{PC}/D_j} \tag{5.30}$$

and

$$b = \frac{2}{3}\left(\frac{l_{PC}}{D_j}\right)^{0.2}. \tag{5.31}$$

The parameters a and b become $a = 2.5$ and $b = 1$ for a potential core length of $l_{PC} = 6.25D_j$ which is in good agreement with experimental results of turbulent

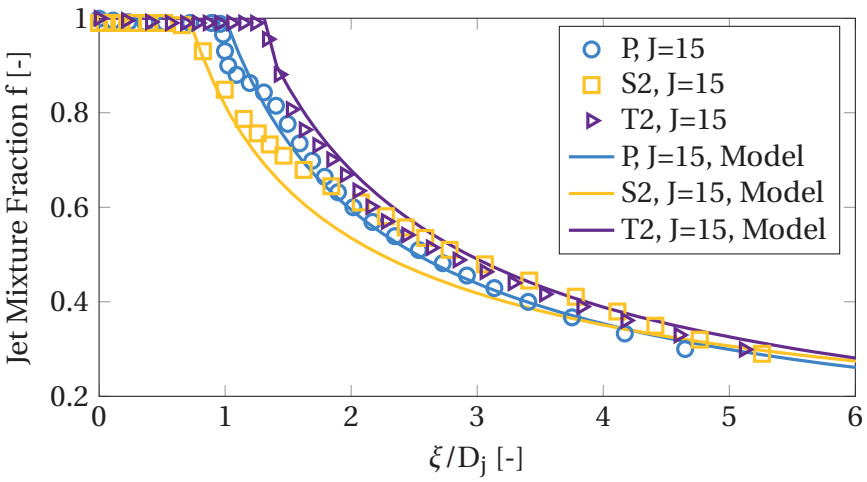

Figure 5.12: Concentration decay of three configurations along the mixture trajectory ξ compared to the concentration decay model from equation 5.29.

free jets [2]. For shorter potential cores l_{PC} the concentration decay is weaker further downstream of the nozzle. A validation of equation 5.29 for three configurations with different potential core lengths is shown in figure 5.12. The model reproduces the concentration decay of the configurations P, S1, S2, T1, and T2.

5.2.4 Summary of Non-Reacting Results

In the previous sections models for the potential core, the mixture trajectory, and the concentration decay were presented. In contrast to existing literature the near-field of the jet is in focus. It is shown that jets with short potential cores mix faster close to the jet exit. The S1 configuration was identified as the fastest mixing configuration in the near field. In the following the presented models are extended to fit the reacting results and to finally compare mixing behavior with NO_x formation.

5.3 Results of Reacting Configurations

In this section the mixture and emission measurements of the reacting cases are presented first. Then, the previously presented models of the non-reacting

jets are extended to reacting jets. At the end the jet mixture fraction fields are compared with measured nitric oxide fields.

Figure 5.13 shows the mixture fraction fields in the symmetry plane for different nozzle configurations for a momentum ratio of J = 15. The cross flow has a temperature of $T_x = 1743\,K$ and the jet equivalence ratio is $\phi_j = 0.77$. The data was measured with the MixPIV method, see section 4.4. In comparison to the non-reacting fields, see figure 5.2, the deeper penetration of the reacting jets is noticeable for all configurations. This change of penetration is explained with the additional momentum created by the gas expansion in the flame front. For all configurations less jet material is present in the wake region. This is also in agreement with literature [44] where the size of the wake region was found to decrease with increasing momentum ratio. The shear layer thickness at the windward and wake side are similar to the non-reacting cases. Finally, the reaction increases the potential core length for all nozzle configurations.

5.3.1 Scaling of Non-Reacting to Reacting Results

In order to use the presented models of potential core length and mixture trajectory from non-reacting cases for reacting cases scaling rules are necessary. The momentum ratio equation 2.37 is therefore modified with the product density ρ_{prod} and the resulting velocity of the jet u_{prod} to capture the additional momentum generated by the reaction. The ratio of the reactant density ρ_j and the product density ρ_{prod}, is written as:

$$r_\phi = \frac{\rho_j}{\rho_{prod}}. \tag{5.32}$$

Due to mass conservation the velocities of unburnt u_j and burnt jet material u_{prod} are inverse compared to the densities:

$$r_\phi = \frac{u_{prod}}{u_j}. \tag{5.33}$$

With the knowledge of r_ϕ it is possible to convert the momentum ratio of reactings jet to equivalent momentum ratios of non-reacting jets:

$$J_{reac} = \frac{\rho_{prod} u_{prod}^2}{\rho_x u_x^2} = \frac{\frac{\rho_j}{r_\phi} u_j^2 r_\phi^2}{\rho_x u_x^2} = \frac{\rho_j u_j^2}{\rho_x u_x^2} r_\phi. \tag{5.34}$$

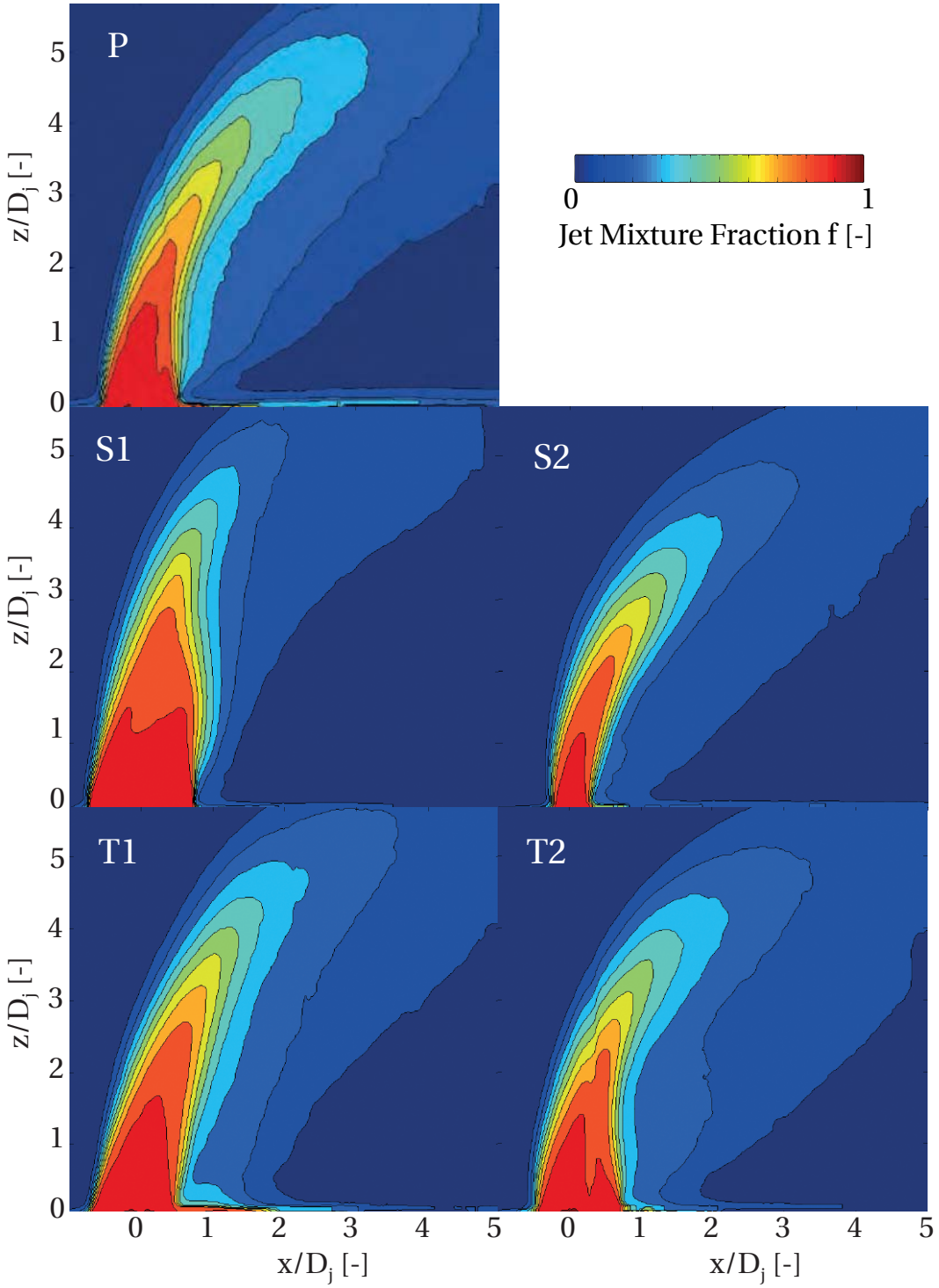

Figure 5.13: Time-averaged jet mixture fraction fields of the different jet nozzle configurations in the x-z plane at y=0, J=15, D_j = 50 mm, reacting case.

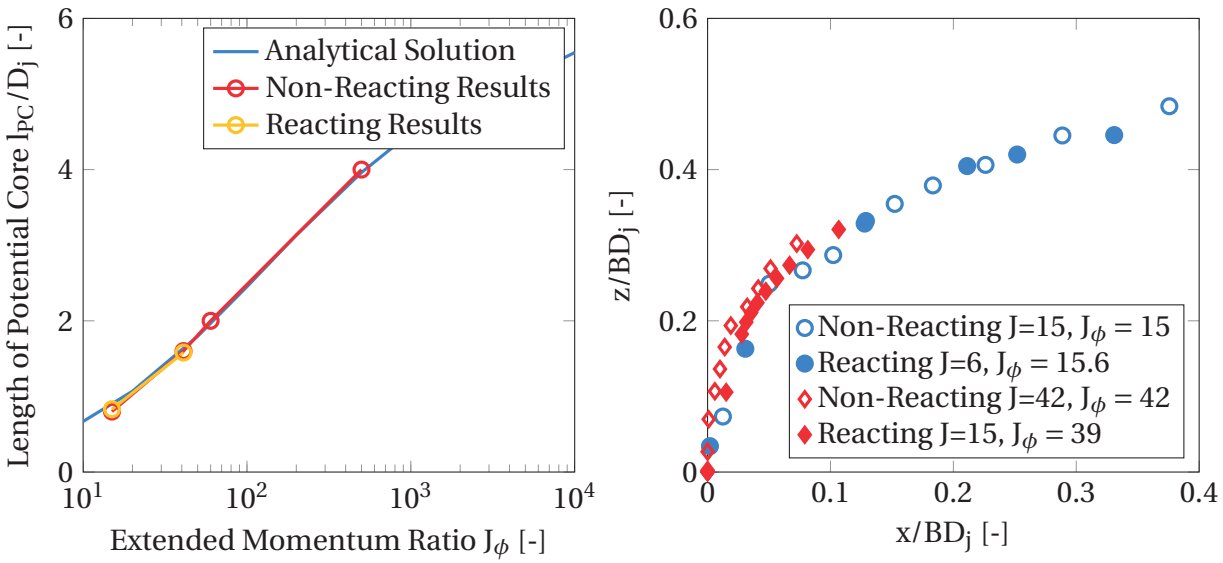

Figure 5.14: Left: Measured length of the potential core of jets from non-reacting and reacting cases compared to the model from equation 5.27. Right: Mixture trajectories for the plain jet configuration for different momentum ratios J with and without reaction normalized with Forlitis' drag-entrainment coefficient B.

The extended momentum ratio equation 5.34 allows predictions of jet mixture trajectories and potential core lengths for reacting cases. In figure 5.14 the right plot shows the jet mixture trajectories of the reacting cases $6 < J < 15$ and the non-reacting cases $15 < J < 42$ normalized with the jet diameter and Forlitis' drag-entrainment coefficient B. For the presented cases with a factor $r_\phi \approx 2.6$ the jet mixture trajectories of all cases lie on one curve. The number of measurements of reacting cases is too small to validate the model of the potential core length. However, the two data points available suggest that the model from equation 5.27 predicts the potential core length of reacting cases if extended momentum ratio J_ϕ from equation 5.34 is used, see the left plot in figure 5.14.

The factor r_ϕ depends on the jet inlet temperature T_j and the adiabatic flame temperature T_{ad}. For constant preheating the adiabatic flame temperature T_{ad} is only influenced by the equivalence ratio of the jet ϕ_j. Trajectories of jets with different equivalence ratios are shown in figure 5.15. Apparently, there is a small influence of ϕ_j. The deeper penetration of richer jets is in agreement with momentum ratio scaling. However, the influence is so small that the same density ratio $\phi = 2.6$ for different jet equivalence ratios is used in equation 5.34.

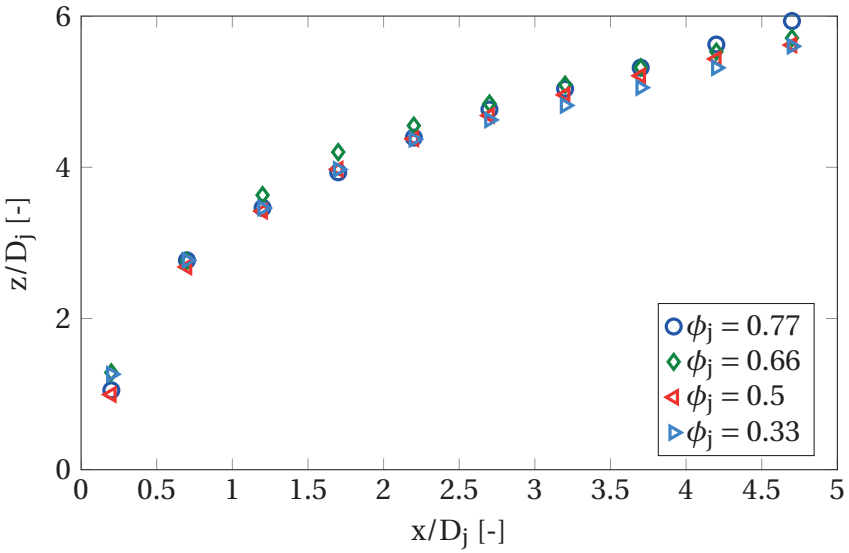

Figure 5.15: Mixture trajectories for the plain jet configuration for different equivalence ratios ϕ_j, momentum ratio J = 15, J_ϕ = 39.

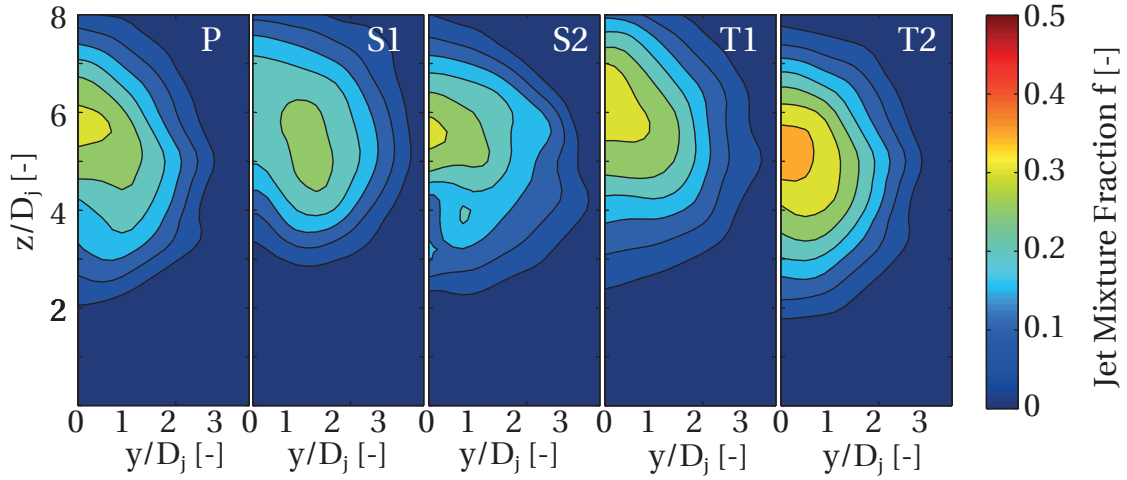

Figure 5.16: Jet mixture fraction f calculated from the O_2 content for different configurations in the y-z plane at $x/D_j = 8$, J=15, $\phi_j = 0.77$.

5.3.2 Mixing and Emissions from Exhaust Analysis

The mixing analysis of the non-reacting cases showed that the nozzle geometry has an influence on the jet concentration decay. In this section mixture fields and nitric oxide emission fields obtained from species concentration measurements in the exhaust gas are presented.

Only the symmetry plane is available from MixPIV and the y-z plane at $x/D = 8$ from emission measurements. The jet mixture fraction determined from emission measurements are presented in figure 5.16. The S1 configuration shows the lowest mixture fraction which is in agreement with the findings in section 5.2.3.

Finally, the nitric oxide fields downstream of the jet injector are measured for a jet equivalence ratio of $\phi_j = 0.77$. Figure 5.17 shows the NO_x emissions in the y-z plane at $x/D = 8$. The NO_x fields scale with the mixture fraction fields calculated from the O_2 content in figure 5.16. The conclusion is that good mixing of jet and cross flow leads to low NO_x emissions. This result was expected. It can further be seen that the S1 configuration has the lowest values, while the T2 configuration shows the highest peak. The S2 configuration has the second lowest NO_x values. It is important to notice that the emissions are measured in a single plane. As it is known from the jet concentration decay (section 5.2.3) the configuration which mixes fast in the beginning can be worse further

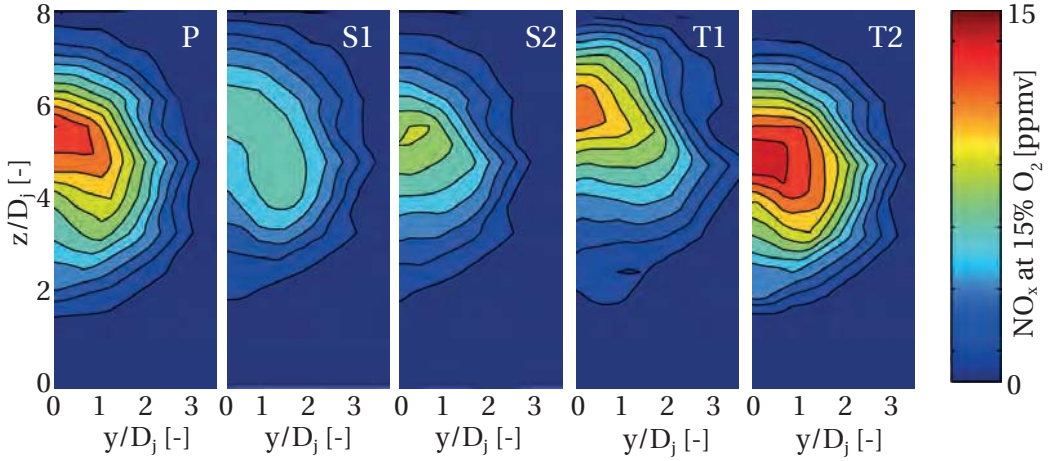

Figure 5.17: Normalized NOx emissions of different configurations in y-z the plane at x/D_j = 8, J=15, $\phi_j = 0.77$.

downstream. Spatial and temporal unmixedness as well as the residence time of the jet material also have an important influence on the nitric oxide formation. With the given experimental setup it is not possible to further study these parameters.

In conclusion, the jet nozzle geometry has an influence on near field mixing and therefore on the NO_x emissions. The mixing fields of the reacting cases show the same trends as the NO_x fields. It was observed that the non-reacting mixture fraction fields of the jet nozzle configurations show different results compared to the reacting cases. Hence, non-reactive mixture measurement alone cannot replace measurements in reacting flows, but they give helpful insights to identify the nozzle geometry with lowest NO_x emissions.

6 Flame Lift-Off

In the following chapter the results of a study on lift-off of premixed jet flames in vitiated cross flow are presented. Although flame lift-off is of high technical interest in the framework of the development of low emission staged combustion systems thorough investigations of this phenomenon are not available in the open literature. In jet in cross flow configurations of technical relevance the temperature of the cross flow is high and its mass flow is much larger than the jet mass flow. Under these conditions the lean mixture flowing through the injector begins to react while it mixes with hot cross flow material. The equivalence ratio of the jet effects the onset of reaction and the spatial heat release distribution but even for mixtures much leaner than the weak combustion limit, complete combustion of the jet mixture is finally achieved. In the experimental investigations presented in the following, the equivalence ratio range of $0.33 < \phi_j < 0.82$ is covered.

As shown in [4] nitric oxide formation in the jet depends on flame position. From the perspective of minimizing NO emissions of combustors it is highly desirable to avoid flame anchoring at the perimeter of the jet injector and to maximize flame lift-off. A higher lift-off height (LO) gives the jet material more time to mix with cross flow products before it starts burning. This additional mixing time reduces the emissions according to the discussion in the theory section 2.6. Lift-off height is defined as the distance of the flame base to the jet nozzle normalized with the jet diameter. The following sections will show and discuss the results of the lift-off measurements. Wherever possible, the influence of single parameters will be plotted for different momentum ratios. The experimental setup is described in section 4.2. In the first section experimental imaging data is shown to clarify the importance of the auto-ignition mechanism as well as flame propagation. At the end of the chapter a model will be derived to predict the lift-off heights of flames under operation conditions.

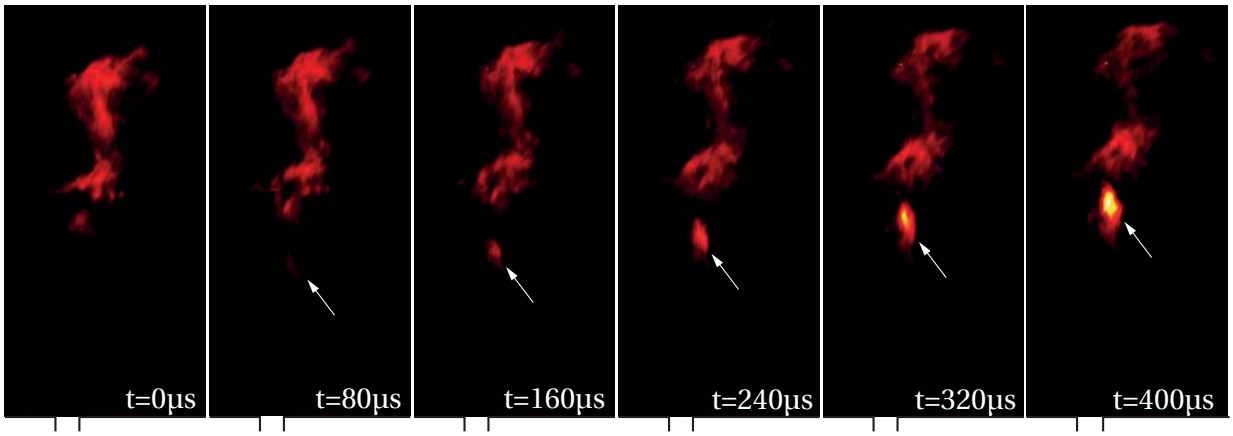

Figure 6.1: Flame chemiluminescence images of a lifted flame with an auto-ignition spot at the flame base.

6.1 Auto-Ignition Events

It is not possible to determine from existing literature wheater auto-ignition or flame propagation dominates flame lift-off. As discussed in theory section 2.5, both mechanisms are important. In flame imaging data recorded at a frame rate of 12.5 kHz reacting spots are detected which are detached from the main flame, see figure 6.1. This is clear evidence for auto-ignition events. However, it is observed that flames propagate upstream in the jet material at appropriate conditions without any triggering by auto-ignition events. For this reason a new model will be deduced on the basis of auto-ignition and flame propagation using experimental data.

6.2 Influence of Operation Conditions on Flame Lift-Off

The results of the parameter study presented below reveal the influence of the jet temperature T_j, the cross flow temperature T_x, the jet equivalence ratio ϕ_j, the jet inlet velocity u_j and the jet diameter D_j on the lift-off height (table 6.1). The primary air mass flow $\dot{m}_x$ was held constant. For this reason the velocity of the cross flow u_x varies only due to the influence of the adiabatic flame temperature on the cross flow density. A change of the jet diameter is required to cover a wide range of jet velocities and to stay within the infrastructural limitations. The model presented in section 6.5 is based on geometrical, fluid dy-

Parameter	Min	Max	Unit
Temperature Preheated Jet T_j	288	673	[K]
Temperature Cross Flow Products T_x	1643	1821	[K]
Velocity Jet u_j	13	106	[m/s]
Velocity Cross Flow u_x	13.3	14.8	[m/s]
Equivalence Ratio Jet ϕ_j	0.33	0.82	[-]
Equivalence Ratio Cross Flow ϕ_x	0.45	0.55	[-]
Diameter Jet D_j	0.015	0.1	[m]
Momentum Ratio J	6	210	[-]

Table 6.1: Operation conditions for the lift-off analysis.

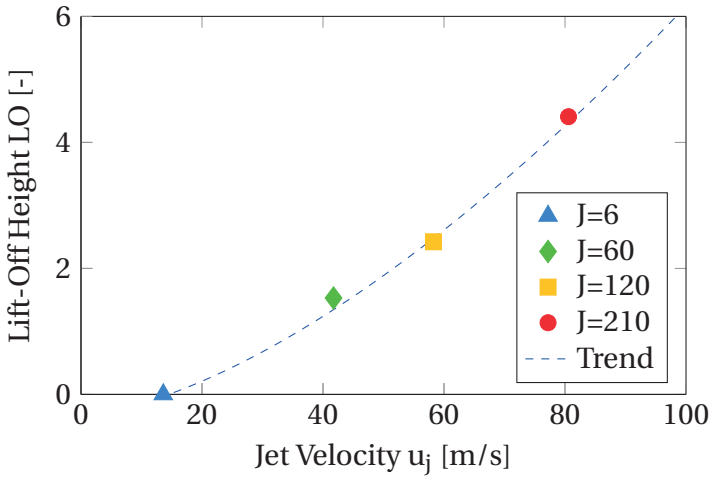

Figure 6.2: Influence of jet velocity on lift-off for different momentum ratios, $\phi_j = 0.82$, $T_x = 1643K$, $T_j = 288K$.

namical and chemical similarity. The relevant parameter for geometrical similarity is the ratio of the lift-off height and the jet diameter:

$$LO = \frac{z}{D_j}. \tag{6.1}$$

It is assumed that the lift-off height z scales with the jet diameter D_j and that D_j does no have an additional influence on flame lift-off beyond that proportionality. It will be shown in section 6.5 that this assumption is valid. The subsequent analysis is based on data from a test matrix consisting of 210 operating points in total.

The first analyzed parameter is the jet velocity. Figure 6.2 shows the lift-off height nondimensionalized with the jet diameter against the jet velocity for operation points where only the jet velocity and diameter are altered. Below

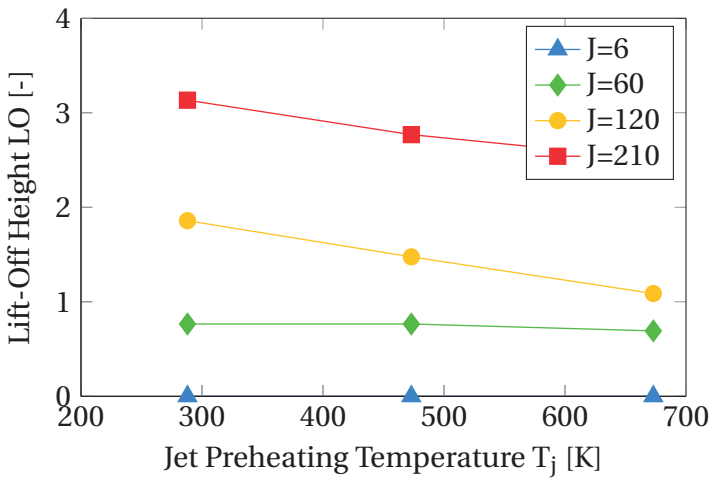

Figure 6.3: Influence of jet preheating temperature T_j on lift-off LO for different momentum ratios J, $\phi_j = 0.82$, $T_x = 1643$K.

a minimum value of the jet velocity lift-off does not occur. The flame either anchors on the perimeter or even flashes back into the jet pipe. At higher velocities the nondimensionalized lift-off height increases with the jet velocity.

Since the jet and cross flow temperatures and equivalence ratios of the lift-off measurements presented in figure 6.2 are constant, the chemical timescale τ_c and the ignition delay τ_{ign} are also constant, while the turbulent timescale τ_{turb} decreases with increasing jet velocity and decreasing jet diameter. A smaller turbulent timescale compared to the chemical timescale results in an increased flame lift-off height.

In figures 6.3 to 6.5 influences of various parameters are shown for different momentum ratios J. Figure 6.3 shows the lift-off heights depending on the jet preheating temperature T_j for different momentum ratios. It can be seen that the lift-off height decreases with increasing preheating temperature. This general trend is explained with the ratio of the chemical timescale τ_c or ignition delay τ_{ign} and the turbulent timescale τ_{turb} (see equations 2.25 and 2.23). It is important to note that the increasing preheating temperature decreases the density of the jet. For a preheating temperature of $T_j = 673$ K the velocity of the jet has to be increased by 54% compared to the $T_j = 288$ K case to keep the momentum ratio constant. The increasing jet velocity causes a decreased turbulent timescale whereas the preheating reduces the chemical timescale. As shown in figure 6.2, increasing the jet velocity alone would increase the lift-

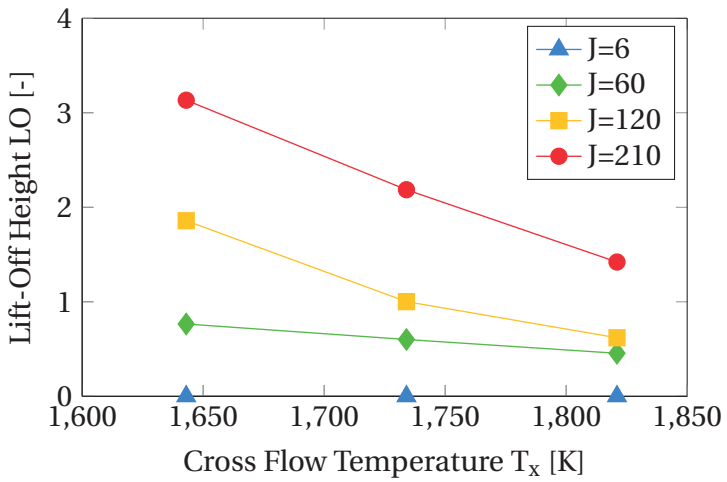

Figure 6.4: Influence of cross flow temperature T_j on lift-off LO for different momentum ratios J, $\phi_j = 0.82$, $T_j = 288\,K$.

off. Here, the decreasing lift-off height shows that the influence of the turbulent timescale is smaller than the influence of the chemical timescale, causing a reduced lift-off height with increasing jet preheating temperature. The data suggests that for a constant jet velocity the lift-off height would decrease more due to preheating. The lift-off model which is presented in section 6.5 confirms this assumption.

The next investigated parameter is the cross flow temperature. The results are presented in figure 6.4. With increasing cross flow temperature the lift-off height decreases. Higher temperatures of the cross flow lead to higher temperatures of the mixture of jet and cross flow and, therefore, reduce the chemical timescale τ_c as well as the ignition delay τ_{ign}. It is apparent that the sensitivity of the lift-off to a change of temperature is much higher for the cross flow temperature than for the jet preheating temperature. This is an important finding which will be discussed later in more detail.

The last investigated parameter is the jet equivalence ratio. Figure 6.5 shows the lift-off height depending on the jet equivalence ratio ϕ_j for different momentum ratios. With increasing jet equivalence ratios the lift-off height decreases. This is explained by the higher reactivity of the mixture and the reduced chemical timescale τ_c. However, the ignition delay increases slightly with higher equivalence ratios for methane-air mixtures [106]. This leads to the insight that the ignition delay cannot explain lift-off depending on jet

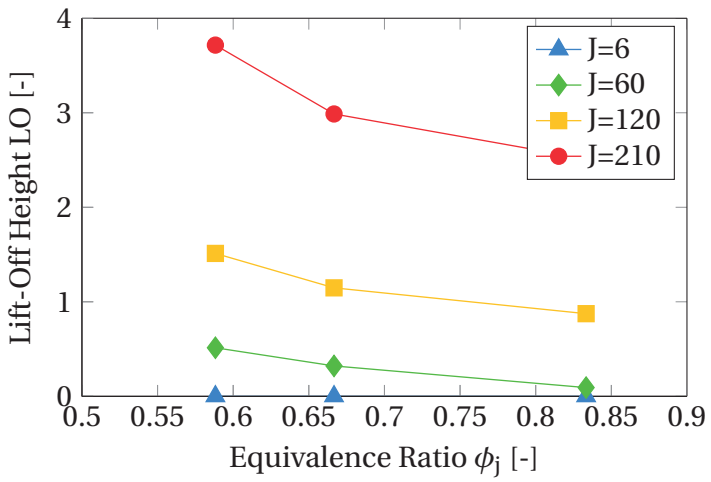

Figure 6.5: Influence of jet equivalence ratio ϕ_j on lift-off height LO for different momentum ratios J, T_X = 1643K, T_j = 288K.

equivalence ratio.

In conclusion, the reduction of the chemical timescale τ_c or ignition delay τ_{ign} through an increase of jet or cross flow temperature as well as equivalence ratio in the jet leads to a decrease of lift-off height. A reduction of the turbulent timescale τ_t due to a higher jet velocity increases the lift-off height.

6.3 Sensitivity Analysis

The influences of jet and cross flow temperature on lift-off height are clearly visible in figures 6.3 to 6.5. However, the importance of the jet temperature seems to be less compared to the cross flow temperature. The main influences on the reactivity of the mixture af jet and cross flow are identified: jet preheating temperature T_j, cross flow temperature T_x and adiabatic jet temperature $T_{ad,j}$ due to the variation of the jet equivalence ratio ϕ_j. Figure 6.6 shows the lift-off height for temperature changes ΔT of the three parameters. The influence of cross flow temperature T_x is about six times higher compared to jet preheating temperature T_j. The influence of temperature change due to an increased equivalence ratio ϕ_j is in between.

The dominant influence of the cross flow temperature suggests that a certain degree of mixing of jet and cross flow material occurs prior to the onset of

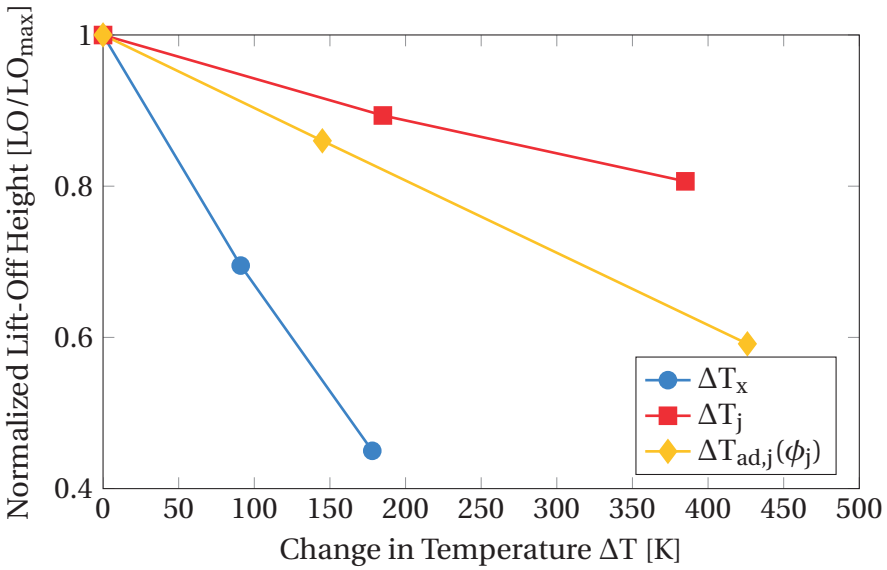

Figure 6.6: Sensitivity of lift-off height LO to changes of the jet T_j and cross flow temperature T_x as well as the equivalence ratio of the jet ϕ_j. $0.66 < \phi_j < 0.82$, $1643 < T_x < 1821$K, $288 < T_j < 673$K, J = 210

reaction in the jet. Such mixing would change the composition and temperature of the reaction zone and, therefore, the laminar flame speed due to an increased cross flow fraction. The next section will introduce more observations regarding the mixture at the onset of combustion.

6.4 Jet Mixture Fraction at the onset of Combustion

The last section showed the strong influence of the cross flow temperature on flame lift-off. It was found that mixing occurs between jet and cross flow before reaction. This mixing determines the jet mixture fraction f at the onset of combustion and it is crucial for the modeling of lift-off. Since direct measurement of f is not possible in the experiment an indirect method is chosen for its evaluation.

It is assumed that the mass flow of the jet $\dot{m}_j$ must be equal to the mass participating in the reaction $\dot{m}_{reac}$:

$$\dot{m}_j = \dot{m}_{reac}. \tag{6.2}$$

The assumption of a mean turbulent flame speed S_t over the flame surface

area A_{fl} leads to equation 6.3.

$$u_j A_j \rho_j = S_t A_{fl} \rho_j. \tag{6.3}$$

Thus, the flame surface area A_{fl} scales inversely to the turbulent flame speed S_t for a constant jet mass flow $\dot{m}_j$. With equation 2.24 from theory section 2.2.3 the turbulent flame speed is estimated. For a constant turbulent time scale τ_t the change of turbulent flame speed S_t depends only on the change of the laminar flame speed S_l:

$$d(S_t)\frac{1}{d\Psi} = d(S_l)\frac{1}{d\Psi}K. \tag{6.4}$$

Ψ represents the jet temperature T_j, the cross flow temperature T_x or the jet equivalence ratio ϕ_j and K a constant. It must be noted that the jet temperature T_j also severely influences the jet velocity and therefore u_t'. However, figure 6.3 shows that the influence of the jet temperature is higher than the jet velocity and therefore the influence of u_t' is assumed to be negligible compared to the temperature influence. Based on these assumptions it is possible to conclude that the slower the conversion of reactants becomes the larger the flame surface must get to satisfy mass conservation:

$$d(S_l)\frac{1}{d\Psi} \sim d\left(\frac{1}{A_{fl}}\right)\frac{1}{d\Psi}. \tag{6.5}$$

It is also known that the laminar flame speed increases for lower jet mixture fractions. As shown in figure 6.7, the laminar flame speed is low for a jet mixture fraction of one which corresponds to jet material only. The more cross flow is added, the hotter the mixture gets and the flame speed increases. The additional cross flow also dilutes the fuel and O_2 of the jet, but the higher temperature dominates the flame speed.

An additional assumption regarding the geometrical shape of the flame will be required for modeling. The flame shape changes depending on the operation conditions and a precise reconstruction of the flame surface area is not possible. From the chemiluminescence data recorded the projected flame surface $A_{fl,pro}$ is measured. Assuming a spherical flame we can calculate a flame radius r_{fl} and thus the flame surface area A_{fl}:

$$r_{fl} = \sqrt{\frac{A_{fl,pro}}{\pi}} \tag{6.6}$$

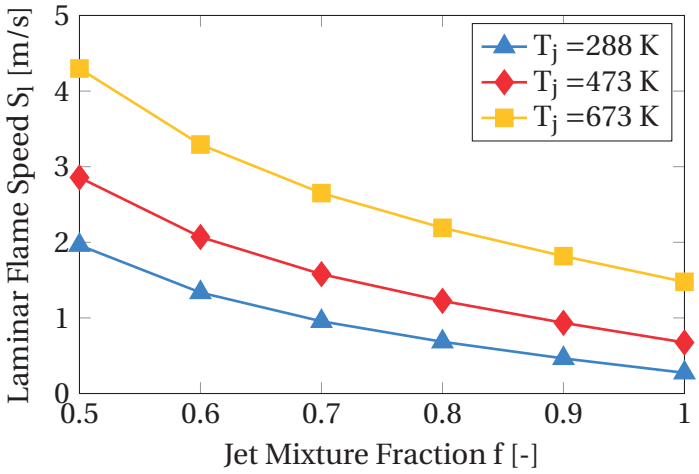

Figure 6.7: Laminar flame speed S_l for different jet preheating temperatures T_j and jet mixture fractions f using the correlation from Peters [85]. One corresponds to jet material and zero to cross flow material, $\phi_j = 0.82$, $T_X = 1643\,K$.

$$A_{fl} = 4\pi r_{fl}^2. \tag{6.7}$$

With the model of the laminar flame speed S_l and equation 6.5 for the change of the flame surface, an estimation of the laminar flame speed and the mixture fraction at the onset of combustion for the different operating points is possible. Figure 6.8 shows the measured change of the inverse normalized flame surface area $1/A_{fl,norm}$ over the jet equivalence ratio. Operation points with equal momentum ratios J are grouped and the flame surface area A_{fl} is normalized using the minimum flame surface area $A_{fl,min}$ of each group:

$$A_{fl,norm} = \frac{A_{fl}}{A_{fl,min}}. \tag{6.8}$$

Furthermore, the calculated laminar flame speed S_l normalized with the minimum flame speed $S_{l,min}$ occurring in each group:

$$S_{l,norm} = \frac{S_l}{S_{l,min}}. \tag{6.9}$$

$S_{l,norm}$ is plotted for different mixture fractions f for the same range of equivalence ratios. The laminar flame speed is calculated using the correlation from [85], see figure 6.7, which includes the parameters temperature, equivalence ratio and pressure. The richer the jet gets, the higher the laminar flame speed

S_l and the inverse flame surface area $1/A_{fl}$. This is shown in figure 6.8 where the calculated normalized laminar flame speeds are compared to the normalized measured inverse flame surfaces. The change of flame surface area A_{fl} depends on jet velocity and therefore on momentum ratio for the shown operation points. The mixture fraction f at the onset of combustion is determined by matching the inverse flame surfaces with the laminar flame speed. Higher equivalence ratios shift the measured points to higher mixture fractions. That is reasonable as the higher fuel content makes the jet more reactive.

In summary, the procedure derived in this section provides the basis for the calculation of the mixture fraction at the onset of combustion. As result of this section the mixture fraction f at the onset of combustion can be determined for every operation point.

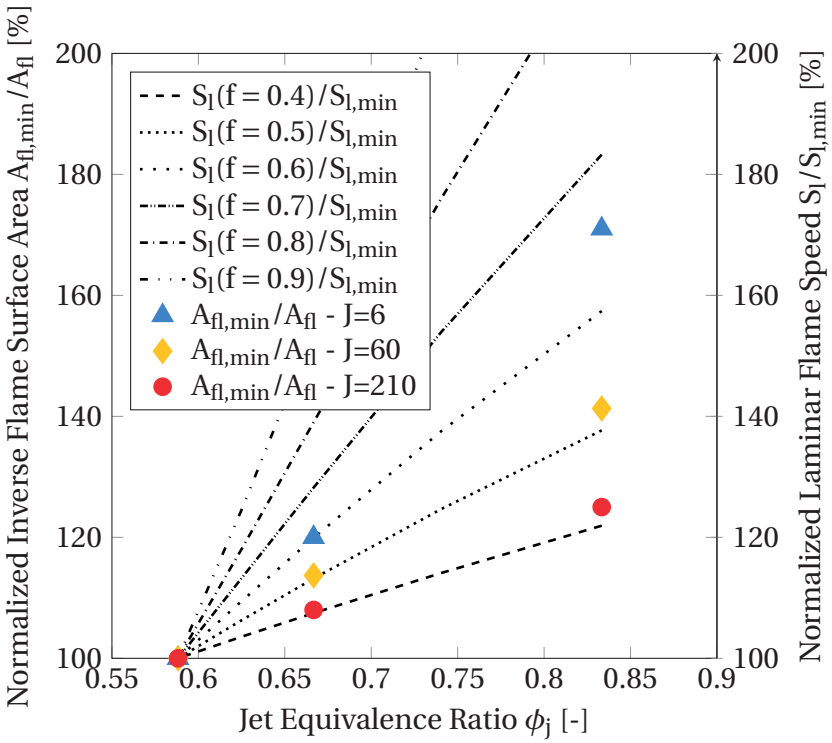

Figure 6.8: Laminar flame speed S_l of different jet mixture fractions f and measured inverse flame surface area $1/A_{fl}$ for the jet equivalence ratio ϕ_j, $T_X = 1643\,K$, $T_j = 288\,K$

6.5 Lift-Off Model

In the previous section the lift-off data was shown and analyzed. In this section, the modeling of the lift-off height on the basis of timescale comparisons using dimensionless numbers will be presented. In the theory section 2.2.3 the dimensionless numbers ignition delay Damköhler number Da_{ign} (equation 2.25) and jet Karlovitz number Ka_j (equation 2.23) were identified to be able to model the flame lift-off behavior.

Figure 6.9 (left) shows the dependency of lift-off heights of operation points with equal cross flow temperature T_X = 1643 K on the jet Karlovitz number for varying jet preheating temperatures $288 < T_j < 673$ K. Each jet temperature leads to a different curve. For low jet Karlovitz numbers the lift-off height is zero and for increasing jet Karlovitz numbers the lift-off height increases. The lift-off heights of the operations points with different jet preheating temperatures do not lie on top of each other. Therefore, it seems that the jet Karlovitz number can model the influence of the jet velocity, but not of the jet temperature on lift-off.

As shown in the last section the onset of combustion is observed after a certain degree of mixing between jet and cross flow. The jet Karlovitz number uses only the jet properties and does not account for mixing between jet and cross flow. Cross flow material increases the laminar flame speed significantly as shown in figure 6.7. With the correlation of flame speed and flame surface area from equation 6.5 it is possible to estimate the mixture fraction f at the onset of combustion depending on the jet velocity in the flame front.

Knowing this mixture fraction allows the calculation of composition and temperature of the reaction zone. Similar to the jet Karlovitz number Ka_j, equation 2.23, the mixture Karlovitz number Ka_{mix}, equation 6.10, is calculated. The difference is that the laminar flame speed and thermal diffusivity depend on the composition and temperature at the onset of combustion.

$$Ka_{mix} = \frac{u_t'^{1.5} a(f)^{0.5}}{D_j^{0.5} S_l(f)^2}. \tag{6.10}$$

The result of the transition from a jet Karlovitz number with only jet composition to the mixture Karlovitz number is seen in figure 6.9. The substantially

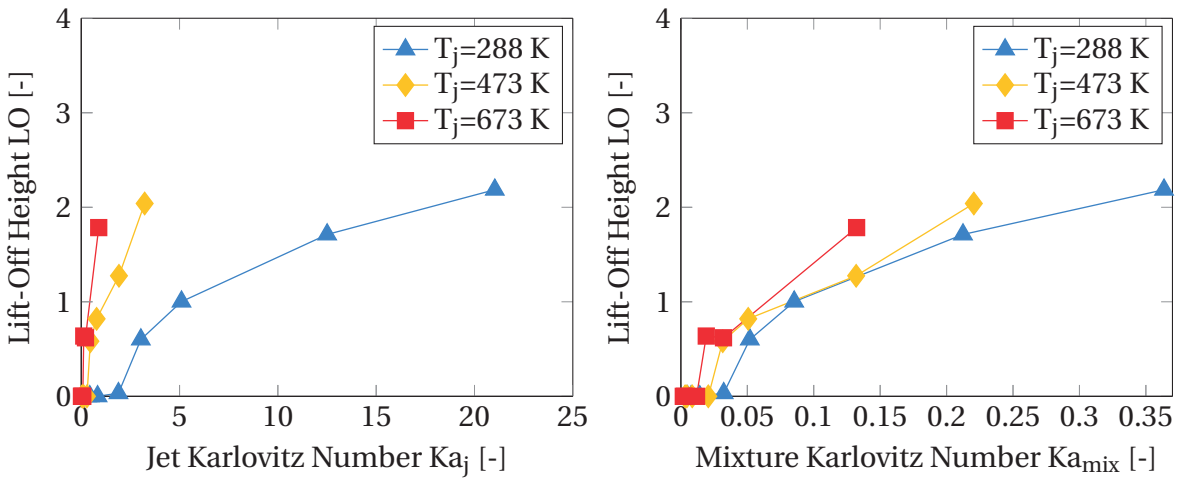

Figure 6.9: Left: Influence of the jet preheating temperature in the jet Karlovitz number is too high. Right: The lift-off heights coincide for the mixture Karlovitz number for ϕ_j = 0.82, T_X = 1643 K, 288 < T_j < 673 K, 6 < J < 210.

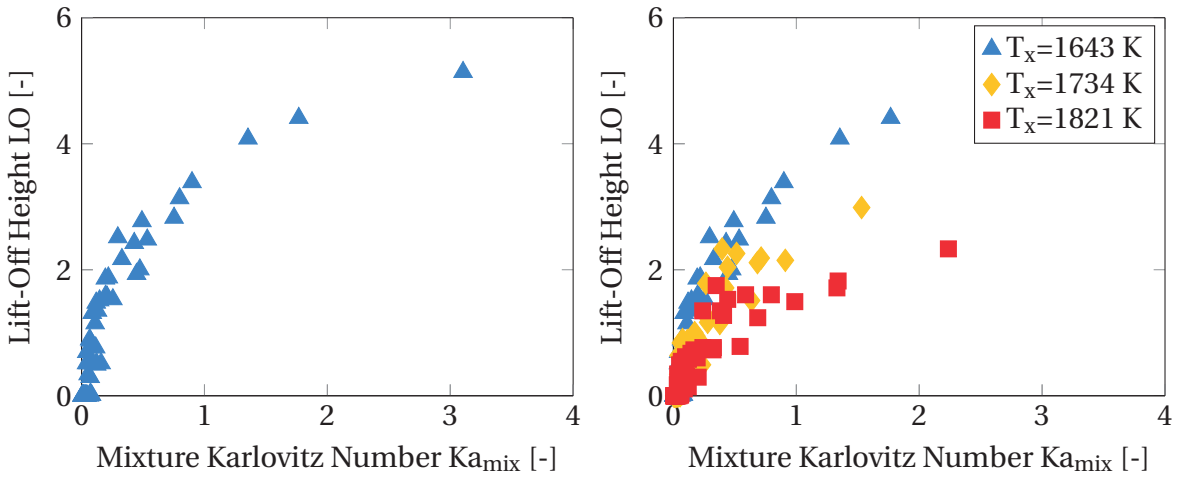

Figure 6.10: Left: Lift-off heights of cases with equal cross flow temperature coincide onto one curve. Right: Lift-off heights of cases with different cross flow temperatures 1643 < T_x < 1821 K do not lie on top of each other. 0.66 < ϕ_j < 0.82, 288 < T_j < 673 K, 6 < J < 210.

higher laminar flame speeds result in a reduction of the Karlovitz number range. Furthermore, the laminar flame speed of colder jets is increased more by mixing than the laminar flame speed of hotter jets. As a consequence, the lift-off data points of cases with different jet temperatures lie on one curve.

It can further be seen in figure 6.10 on the left that all measured lift-off heights of one cross flow temperature coincide onto one curve. However, the plot on the right shows that lift-off heights of operation points with different cross

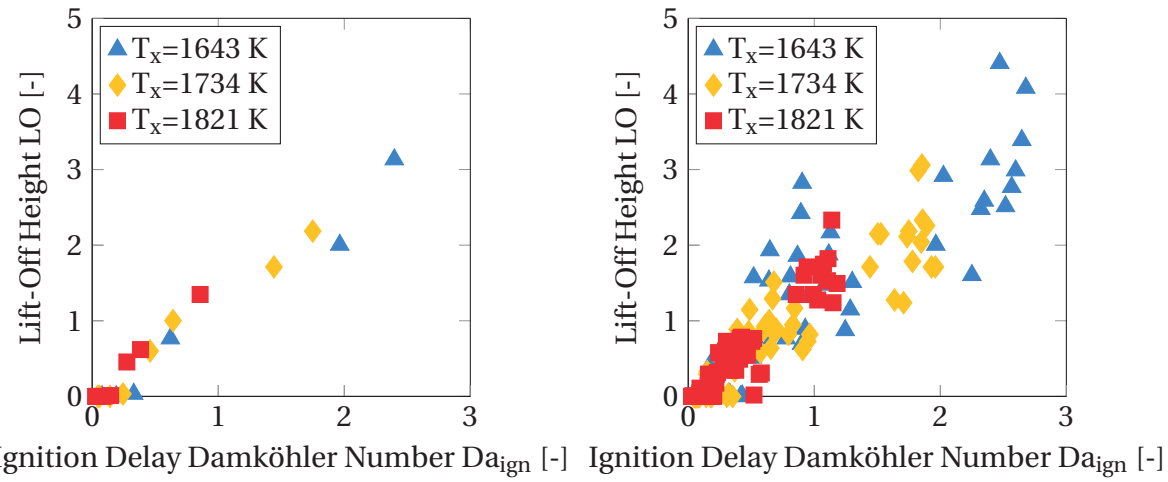

Figure 6.11: Left: The ignition delay Damköhler number correlates with lift-off heights cases with different cross flow temperatures. Right: For varying jet condition, $0.66 < \phi_j < 0.82$ and $288 < T_j < 673$ K, the ignition delay Damköhler number does not correlate with the lift-off heights..

flow temperatures do not lie on top of each other. Each cross flow temperature results in a separate curve. As already found in section 6.4, the influence of the cross flow temperature on lift-off height is much higher compared to jet temperature.

Since the chemical timescale based on the laminar flame speed is not able to capture this influence, an additional timescale is needed. The ignition delay τ_{ign} is the dominant parameter for auto-ignition dominated experiments. In the past, this parameter has been successfully used to correlate auto-ignition data [11, 60, 75, 92].

The ignition delay Damköhler number Da_{ign} which was introduced in the theory section 2.2.3, equation 2.25, is be used to calculate the ignition delay in dimensionless form. The ignition delay, however, is not calculated for the jet composition as there is no physically useful ignition delay for methane mixtures below 873 K. According to literature [11, 60, 75, 92], the ignition delay is calculated for the most reactive mixture fraction (MRMF). To get the MRMF, the ignition delays of all mixtures of jet and cross flow for $0 < f < 1$ are calculated using a zero-dimensional plug flow reactor in the software Cantera [35] with the chemical mechanism GRI 3.0 [103]. The mixture with the lowest ignition delay time τ_{ign} is the MRMF which is used to calculate the ignition delay Damköhler number.

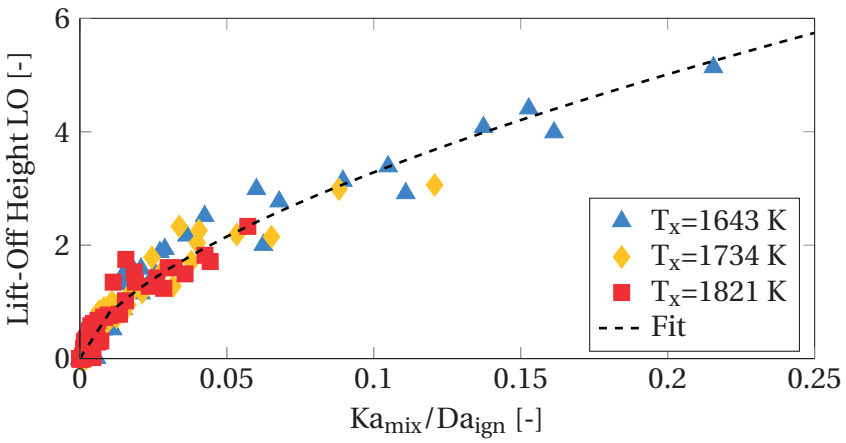

Figure 6.12: Lift-off heights of all investigated operation points correlate well with the model based on the ratio Ka_{mix}/Da_{ign}.

This additional dimensionless number correlates lift-off heights of operation points with different cross flow temperatures very well, see figure 6.11 on the left. However, the model does not work for different jet temperatures and equivalence ratios, see figure 6.11 on the right.

Obviously, neither the model based on the mixture Karlovitz number Ka_{mix} nor the approach based on the ignition Damköhler number Da_{ign} have the potential for correlating the entire lift-off data for premixed jets in hot cross flows.

The solution is a combination of the two dimensionless numbers. The mixture Karlovitz number Ka_{mix} is extended by the ignition delay Damköhler number Da_{ign} which leads to

$$Ka_{mix}/Da_{ign} = \frac{\tau_c}{\tau_\eta}\frac{\tau_{ign}}{\tau_t} = \frac{u_t'^{1.5}a(f)^{0.5}}{D_j^{0.5}S_l(f)^2}\frac{u_t'\tau_{ign}}{D_j}. \tag{6.11}$$

The combination of these two dimensionless numbers includes the influence of auto-ignition time scales due to different cross flow temperatures and the influence of the jet composition and temperature on the laminar flame speed. Figure 6.12 shows that the lift-off heights of all measured operation points correlate well with Ka_{mix}/Da_{ign}. Therefore the ratio of both numbers seem to capture all relevant effects.

6.6 Simplified Lift-Off Model

The application of the model based on the ratio Ka_{mix}/Da_{ign} requires knowledge concerning the mixture fraction at the onset of combustion. This mixture fraction was determined using optical measurements of many operation points so far. For technical applications these optical measurements are too expensive. Therefore, a simplification is introduced which makes the application of the model easier in practice. The mixture fraction at the onset of combustion of all operation points is assumed to be f = 0.6. In the following it is shown that this constant mixture fraction assumption hardly influences the accuracy of the predicted lift-off heights.

The results of the simplified approach are shown in figure 6.13. The data still lines up quite well. In combination with the previous results this leads to the conclusion that the mixture fraction should be considered for correct laminar flame speeds in order to achieve the optimum quality of the correlation of the data. However, the estimate based on an assumed value for the mixture fraction f already leads to good results. From the point of view of the application of the presented approach it is important that even without knowledge of the exact mixture fraction the model based on the ratio Ka_{mix}/Da_{ign} can be used for estimating lift-off heights.

Finally, the data of the simplified approach from figure 6.13 is fitted to get a lift-off correlation based on the introduced model:

$$LO = 9.7(Ka_{mix}/Da_{ign})^{0.61} \tag{6.12}$$

6.7 Scaling Rules for Lift-Off Similarity

To achieve lift-off similarity between laboratory model combustors and heavy-duty gas turbine combustors the ratio Ka_{mix}/Da_{ign} must be equal. The ratio Ka_{mix}/Da_{ign} consists of five parameters of which three are mainly influenced by the pressure assuming the same fuel for the experiment and the gas turbine combustor. Table 6.2 shows the parameters and their scaling with pressure. The thermal diffusivity a and the ignition delay τ_{ign} scale linearly inverse with pressure. The scaling of the laminar flame speed depends on the

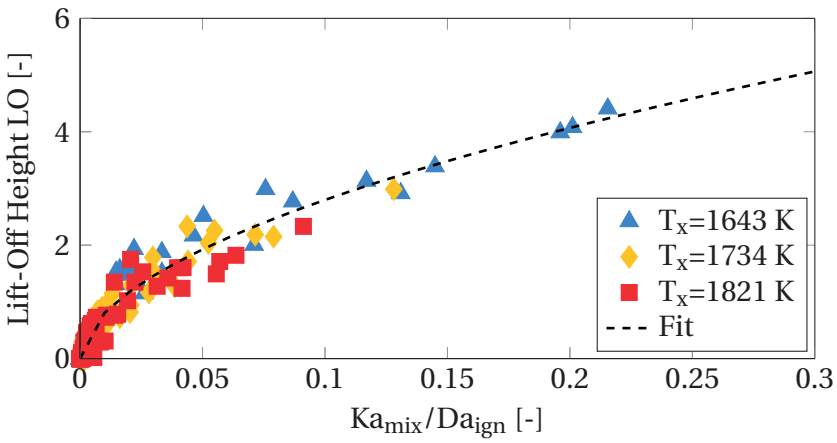

Figure 6.13: With the assumption of a constant mixture fraction at the onset of combustion f = 0.6 the lift-off heights of all investigated operation points still correlate well with the model based on the ratio Ka_{mix}/Da_{ign}.

equivalence ratio and preheating temperature. For a preheating temperature of $T_j = 673\,K$ and an equivalence ratio of $\phi_j = 0.6$ typical for a gas turbine combustor the scaling with pressure is $p^{-0.6}$. The ratio Ka_{mix}/Da_{ign} can then be written with the pressure dependencies:

$$Ka_{mix}/Da_{ign} = \frac{u_t'^{2.5} a(f)^{0.5} \tau_{ign}}{D_j^{1.5} S_l(f)^2} \sim \frac{u_t'^{2.5}}{D_j^{1.5}} \frac{p^{-0.5} p^{-1}}{p^{-0.6 \cdot 2}} = \frac{u_t'^{2.5}}{D_j^{1.5}} \frac{1}{p^{0.3}}. \tag{6.13}$$

The resulting influence of the pressure is relatively small. It can be compensated by either increasing the jet velocity or decreasing the jet nozzle diameter. For most operation points the combustion regime as specified in section 2.2.3 does not change due to the scaling, but for some cases the limits between the regimes are crossed. However, for the scaling based on the Ka_{mix}/Da_{ign} ratio the same combustion regime is assumed for the engine combustor and the laboratory model combustor.

6.8 Application to Machine Conditions

The lift-off model presented in section 6.6 can also be applied to high pressure conditions of gas turbine combustors to predict the lift-off height of jet flames in a second stage. With typical operation conditions of a gas turbine combustor shown in section 3.1, table 3.1, the lift-off height LO can be estimated. Assuming a constant mass flow split between first and second stage

Parameter	Pressure Scaling
τ_{ign}	p^{-1}
a	p^{-1}
S_l	$p^{-0.6}$
D_j	p^0
u'_t	p^0

Table 6.2: Scaling of the parameters of the lift-off model based on the ratio Ka_{mix}/Da_{ign} with pressure.

the power output of the second stage is controlled by the jet equivalence ratio ϕ_j. The lift-off height for varying jet equivalence ratios ϕ_j is shown in figure 6.14. The model based on the ratio Ka_{mix}/Da_{ign} predicts lifted flames for all equivalence ratios. For rich cases $\phi_j = 0.8$ the lift-off height decreases to $LO = 0.4D_j$. For decreasing equivalence ratios the lift-off height increases. The dominating parameter is the laminar flame speed S_l.

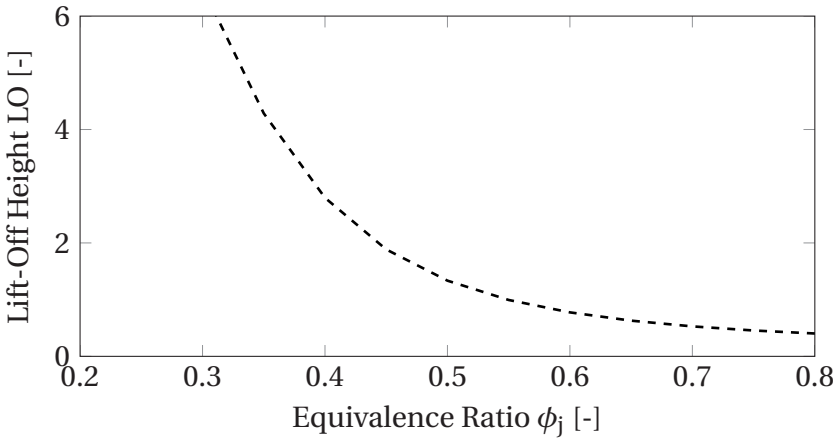

Figure 6.14: Flame lift-Off heights for heavy-duty gas turbine combustor conditions.

7 Summary and Conclusions

Future generations of heavy-duty gas turbines must be more flexible concerning power output due to the higher fluctuations in the grid, realize higher turbine inlet temperatures to increase the efficiency, and also meet higher emission standards set by the regulators. The combustion process has a big impact on all of the above mentioned requirements. Staged combustion was identified to be a promising technology in the further development of gas turbine combustors under the given requirements and is therefore subject of this work.

A large scale staged combustion test rig is set up to investigate the combustion of a premixed jet in reacting cross flow with focus on mixing, NO_x emissions and flame lift-off. While the jet nozzle geometries can enhance mixing in the near field, flame lift-off delays the combustion further downstream and increases mixing time until the onset of combustion.

In the first part of this study correlations for the length of the potential core, the jet trajectory and the concentration decay are derived for jets in cross flow based on non-reacting experimental data. Afterwards, the correlations are extended and validated for reacting jets in hot cross flow and different jet nozzle geometries. It is found that the length of the potential core depends mainly on the momentum ratio and the nozzle geometry, while the jet trajectory and concentration decay additionally depend on the alignment of the nozzle. Jets from slot nozzles aligned perpendicular to the cross flows penetrate less because of high drag. Consequently, slot nozzles aligned parallel to the cross flow show deeper penetration. The influence of reaction is successfully integrated into the correlations by adding the momentum generated by combustion. The slot nozzle configuration aligned parallel to the cross flow shows the best mixing properties and the lowest NO_x emissions.

In the second part of this study the mechanisms which control flame lift-off are investigated. It is found that premixed jets in hot cross flow are controlled

by auto-ignition and flame propagation. In literature only models are found which consider one or the other effect. A parameter study of the jet temperature, jet equivalence ratio, jet velocity and cross flow temperature reveals that the influence of the cross flow temperature on the lift-off height is strong, while the influence of the jet temperature is relatively weak and the jet equivalence ratio has moderate influence. Based on dimensionless numbers two models are derived to predict the lift-off heights. Both models are based on a Karlovitz number and a ignition delay Damköhler number. The Karlovitz number represents the influences of flame propagation and is based on the composition and temperatures of the jet and cross flow mixture at the onset of combustion. The ignition delay Damköhler number represents auto-ignition and is calculated for the most reactive mixture fraction of jet and cross flow. In the first model the mixture fraction of jet and cross flow in the flame front is determined experimentally to calculate the dimensionless numbers. This model is able to correlate all measured lift-off heights with the ratio Ka_{mix}/Da_{ign}. The second model is simplified by assuming the same mixture fraction in the flame front for all cases. This simplification makes the model easier to apply in technical design processes and still delivers good results.

Bibliography

[1] Abdel-Gayed, R. G., Bradley, D., and Lung, F. K.-K., 1989. "Combustion Regimes and the Straining of Turbulent Premixed Flames". *Combustion and Flame,* ***76***, pp. 213–218.

[2] Abramovich, G. N., 1963. *The Theory of Turbulent Jets.* MIT Press.

[3] Adachi, S., Iwamoto, A., Hayashi, S., Yamada, H., and Kaneko, S., 2007. "Emissions in Combustion of Lean Methane-Air and Biomass-Air Mixtures Supported by Primary Hot Burned Gas in a Multi-Stage Gas Turbine Combustor". *Proceedings of the Combustion Institute,* ***31***(2), pp. 3131–3138.

[4] Ahrens, D., Kolb, M., Hirsch, C., and Sattelmayer, T., 2014. "NO_x Formation in a Reacting Premixed Jet in Hot Cross Flow". In Proceedings of ASME Turbo Expo 2014, no. GT2014-26139.

[5] Ahrens, D., Kolb, M., Hirsch, C., and Sattelmayer, T., 2015. "Influences of Pre-Flame and Post-Flame Mixing on NOx Formation in a Reacting Premixed Jet in Hot Cross Flow". In Proceedings of ASME Turbo Expo 2015, no. GT2014-26139.

[6] Aida, N., Nishijima, T., Hayashi, S., Yamada, H., and Kawakami, T., 2005. "Combustion of Lean Prevaporized Fuel–Air Mixtures Mixed With Hot Burned Gas for Low-NO_x Emissions Over an Extended Range of Fuel–Air Ratios". *Proceedings of the Combustion Institute,* ***30***(2), pp. 2885–2892.

[7] Aida, N., Nishijima, T., Yamada, H., Hayashi, S., and Kawakami, T., 2003. "Injection of Lean Mixtures into Hot Burned Gas for Maintaining Low-NOx Emissions over an Extended Range of Fuel-Air Ratios in Prevaporized Combustion". *Bulletin of the Technical College of Hosei University,* ***40***(TS-142), pp. 9–16.

[8] Albertson, M. L., Dai, Y. B., Jensen, R. A., and Rouse, H., 1950. "Diffusion of Submerged Jets". *American Society of Civil Engineers,* ***115***(1), pp. 639–697.

[9] Andreopoulos, J., and Rodi, W., 1984. "Experimental Investigation of Jets in a Crossflow". *Journal of Fluid Mechanics,* ***138***(1), pp. 93–127.

[10] Andrews, G., Bradley, D., and Lwakabamba, S., 1975. "Turbulence and Turbulent Flame Propagation - a Critical Appraisal". *Combustion and Flame,* ***24***, pp. 285–304.

[11] Blouch, J. D., and Law, C. K., 2003. "Effects of Turbulence on Non-premixed Ignition of Hydrogen in Heated Counterflow". *Combustion and Flame,* ***132***(3), pp. 512–522.

[12] Bosanquet, C. H., and Pearson, J. L., 1936. "The Spread of Smoke and Gases from Chimneys". *Transactions of the Faraday Society,* ***32***, pp. 1249–1263.

[13] Bowman, C. T., 1992. "Control of Combustion-Generated Nitrogen Oxide Emissions: Technology Driven by Regulation". *Symposium (International) on Combustion,* ***24***(1), pp. 859–878.

[14] Boyce, M. P., 2012. *Gas Turbine Engineering Handbook*, 4 ed. Elsevier.

[15] Braun, J., 2010. "Kapitel 2: Thermodynamische Grundlagen". In *Stationäre Gasturbinen*, C. Lechner and J. Seume, eds. Springer Verlag, pp. 11–47.

[16] Broadwell, J. E., and Breidenthal, R. E., 1984. "Structure and Mixing of a Transverse Jet in Incompressible Flow". *Journal of Fluid Mechanics,* ***148***, pp. 405–412.

[17] Brooks, F. J., 2000. "GE Gas Turbine Performance Characteristics". *GE Power Systems,* ***10***(GER-3567H), pp. 1–16.

[18] Cai, W., 2011. Multi-Stage Axial Combustion System, Feb. 15. US Patent 7,886,539.

[19] Callaghan, E. E., and Ruggeri, R. S., 1948. Investigation of the Penetration of an Air Jet Directed Perpendicularly to an Air Stream. Tech. Rep. TN 1615, National Advisory Committee for Aeronautics.

[20] Coelho, S. L. V., and Hunt, J. C. R., 1989. "The Dynamics of the Near Field of Strong Jets in Crossflows". *Journal of Fluid Mechanics,* ***200***, pp. 95–120.

[21] Conti, R. S., and Hertzberg, M., 1988. "Thermal Autoignition Temperatures for Hydrogen-Air and Methane-Air Mixtures". *Journal of Fire Sciences,* ***6***(5), pp. 348–355.

[22] Correa, S. M., 1993. "A Review of NOx Formation Under Gas-Turbine Combustion Conditions". *Combustion Science and Technology,* ***87***(1-6), pp. 329–362.

[23] Cortelezzi, L., and Karagozian, A. R., 2001. "On the Formation of the Counter-Rotating Vortex Pair in Transverse Jets". *Journal of Fluid Mechanics,* ***446***, pp. 347–373.

[24] DeCorso, S., 1978. Hybrid Combustor with Staged Injection of Pre-Mixed Fuel, Sept. 12. US Patent 4,112,676.

[25] Delany, N. K., and Sorensen, N. E., 1953. Low-speed Drag of Cylinders of Various Shapes. Tech. Rep. TN 3038, National Advisory Committee for Aeronautics.

[26] Demayo, T. N., Leong, M. Y., and Samuelsen, G. S., 2004. Assessing Jet-Induced Spatial Mixing in a Rich, Reacting Crossflow. Tech. Rep. CR–2004-212886, NASA.

[27] Echekki, T., and Chen, J. H., 2003. "Direct Numerical Simulation of Autoignition in Non-Homogeneous Hydrogen-Air Mixtures". *Combustion and Flame,* ***134***(3), pp. 169–191.

[28] Forliti, D. J., 2012. "Trajectory and Mixing Scaling Laws for Confined and Unconfined Transverse Jets". In 42nd AIAA Fluid Dynamics Conference and Exhibit, no. 2012-3353, American Institute of Aeronautics and Astronautics.

[29] Fric, T. F., and Roshko, A., 1994. "Vortical Structure in the Wake of a Transverse Jet". *Journal of Fluid Mechanics,* ***279***, pp. 1–47.

[30] Galeazzo, F. C. C., Donnert, G., Cardenas, C., Sedlmaier, J., Habisreuther, P., Zarzalis, N., Beck, C., and Krebs, W., 2013. "Computational Modeling

of Turbulent Mixing in a Jet in Crossflow". *International Journal of Heat and Fluid Flow,* ***41***, pp. 55 – 65.

[31] Galeazzo, F. C. C., Donnert, G., Habisreuther, P., Zarzalis, N., Valdes, R., and Krebs, W., 2010. "Measurement and Simulation of Turbulent Mixing in a Jet in Crossflow". In Proceedings of ASME Turbo Expo 2010, no. GT2010-22709.

[32] Galeazzo, F. C. C., Kern, M., Habisreuther, P., Zarzalis, N., and Beck, C., 2011. "Simulation of a Lifted Flame in a Vitiated Air Environment". In Proceedings of the European Combustion Meeting.

[33] Galeazzo, F. C. C., Prathap, C., Kern, M., Habisreuther, P., and Zarzalis, N., 2012. "Investigation of a Flame Anchored in Crossflow Stream of Vitiated Air at Elevated Pressures". In Proceedings of ASME Turbo Expo 2012, no. GT2012-69632.

[34] Goertler, H., 1942. "Berechnung von Aufgaben der freien Turbulenz auf Grund eines neuen Näherungsansatzes". *ZAMM-Journal of Applied Mathematics and Mechanics/Zeitschrift für Angewandte Mathematik und Mechanik,* ***22***(5), pp. 244–254.

[35] Goodwin, D., Malaya, N., Moffat, H., and Speth, R., 2003. "Cantera: An Object-Oriented Software Toolkit for Chemical Kinetics, Thermodynamics, and Transport Processes". *Chemical Vapor Deposition XVI and EUROCVD,* ***14***(40), pp. 2003–08.

[36] Grinstein, F., 2001. "Vortex Dynamics and Entrainment in Rectangular Free Jets". *Journal of Fluid Mechanics,* ***437***, 6, pp. 69–101.

[37] Gutmark, E., Schadow, K. C., Parr, T. P., Hanson-Parr, D. M., and Wilson, K. J., 1989. "Noncircular Jets in Combustion Systems". *Experiments in Fluids,* ***7***(4), pp. 248–258.

[38] Gutmark, E. J., and Grinstein, F. F., 1999. "Flow Control with Noncircular Jets". *Annual Review of Fluid Mechanics,* ***Vol. 31***, pp. p. 239–272.

[39] Gutmark, E. J., Ibrahim, I. M., and Murugappan, S., 2008. "Circular and Noncircular Subsonic Jets in Cross Flow". *Physics of Fluids,* ***20:075110***.

[40] Habisreuther, P., Galeazzo, F. C. C., Prathap, C., and Zarzalis, N., 2013. "Structure of Laminar Premixed Flames of Methane Near the Auto-Ignition Limit". *Combustion and Flame,* ***160***(12), pp. 2770 – 2782.

[41] Hada, S., Tsukagoshi, K., Masada, J., and Ito, E., 2012. "Test Results of the World's First 1,600° J-series Gas Turbine". *Mitsubishi Heavy Industries Technical Review,* ***49***(1), p. 18.

[42] Haight, B., 2014. "New Air-Cooled H-Class". *Diesel and Gas Turbine Worldwirde*, 5, pp. 30–34.

[43] Hassa, C., Migueis, C. E., Voigt, P., and Box, P. P., 1998. "Design Principles for the Quench Zone of Rich-Quench-Lean Combustors". In 1st AVT-PPS Symposium on Design Principles and Methods for Aircraft Gas Turbine Engines, Toulouse, pp. 11–15.

[44] Hasselbrink, E. F., and Mungal, M. G., 2001. "Transverse Jets and Jet Flames. Part 1. Scaling Laws for Strong Transverse Jets". *Journal of Fluid Mechanics,* ***443***, pp. 1–25.

[45] Hatch, M. S., Sowa, W. A., Samulersen, G. S., and Holdeman, J. D., 1995. "Geometry and Flow Influences on Jet Mixing in a Cylindrical Duct". *Journal of Propulsion and Power,* ***11***(3), pp. 393–402.

[46] Haven, B. A., and Kurosaka, M., 1997. "Kidney and Anti-Kidney Vortices in Crossflow Jets". *Journal of Fluid Mechanics,* ***352***, pp. 27–64.

[47] Hinze, J., 1959. *Turbulence: An Introduction to Its Mechanism and Theory*. McGraw-Hill Series in Mechanical Engineering. McGraw-Hill.

[48] Hoferichter, V., 2013. "Pollutant Formation in a Reacting Jet in Hot Cross Flow". Master's thesis, Technical University of Munich.

[49] Holdeman, J., Srinivasan, R., and Berenfeld, A., 1984. "Experiments in Dilution Jet Mixing". *AIAA Journal,* ***22***(10), pp. 1436–1443.

[50] Holdeman, J. D., 1972. Correlation for the Temperature Profiles in the Plane of Symmetry Downstream of a Jet Injected Normal to a Crossflow. Tech. Rep. TN D-6966, NASA.

[51] Hussein, H. J., Capp, S. P., and George, W. K., 1994. "Velocity Measurements in a High-Reynolds-Number, Momentum-Conserving, Axisymmetric, Turbulent Jet". *Journal of Fluid Mechanics,* ***258***, pp. 31–75.

[52] Im, H. G., Chen, J. H., and Law, C. K., 1998. "Ignition of Hydrogen-Air Mixing Layer in Turbulent Flows". *Symposium (international) on combustion,* ***27***(1), pp. 1047–1056.

[53] Joshi, N., and Moreno, F., 1990. Staged Low NOx Premix Gas Turbine Combustor, May 29. US Patent 4,928,481.

[54] Kalghatgi, G., 1984. "Lift-off Heights and Visible Lengths of Vertical Turbulent Jet Diffusion Flames in Still Air". *Combustion Science and Technology,* ***41***(1-2), pp. 17–29.

[55] Kamotani, Y., and Greber, I., 1972. "Experiments on a Turbulent Jet in a Cross Flow". *AIAA Journal,* ***10***(11), pp. 1425–1429.

[56] Karagozian, A. R., 1986. "The Flame Structure and Vorticity Generated by a Chemically Reacting Transverse Jet". *AIAA Journal,* ***24***(9), pp. 1502–1507.

[57] Karagozian, A. R., 2010. "Transverse Jets and Their Control". *Progress in Energy and Combustion Science,* ***36***(5), pp. 531 – 553.

[58] Keffer, J. F., and Baines, W. D., 1963. "The Round Turbulent Jet in a Cross-Wind". *Journal of Fluid Mechanics,* ***15***(04), pp. 481–496.

[59] Kelso, R. M., Lim, T. T., and Perry, A. E., 1996. "An Experimental Study of Round Jets in Cross-Flow". *Journal of Fluid Mechanics,* ***306***, pp. 111–144.

[60] Kerkemeier, S. G., Frouzakis, C., Boulouchos, K., and Mastorakos, E., 2010. "Numerical Simulation of Autoignition of a Diluted Hydrogen Jet in Co-Flowing Turbulent Hot Air". *AIAA paper,* ***217***, p. 2010.

[61] Kolb, M., Ahrens, D., Hirsch, C., and Sattelmayer, T., 2013. "Quantification of Mixing of a Reacting Jet in Hot Cross Flow Using Mie Scattering". In "Lasermethoden in der Strömungsmesstechnik".

[62] Lamont, W. G., 2012. "Experimental Study of a Staged Combustion System for Stationary Gas Turbine Applications". PhD thesis, Purdue University.

[63] Lamont, W. G., Roa, M., and Lucht, R. P., 2014. "Application of Artificial Neural Networks for the Prediction of Pollutant Emissions and Outlet Temperature in a Fuel-Staged Gas Turbine Combustion Rig". In Proceedings of ASME Turbo Expo 2014, no. GT2014-25030.

[64] Lamont, W. G., Roa, M., Meyer, S. E., and Lucht, R. P., 2012. "Emission Measurements and CH* Chemiluminescence of a Staged Combustion Rig for Stationary Gas Turbine Applications". *Journal of Engineering for Gas Turbines and Power,* ***134***(8), p. 081502.

[65] Lauer, M., 2011. "Determination of the Heat Release Distribution in Turbulent Flames by Chemiluminescence Imaging". PhD thesis, Lehrstuhl für Thermodynamik, Technische Universität München.

[66] Lechner, C., and Seume, J., eds., 2009. *Stationäre Gasturbinen.* Springer.

[67] Leong, M. Y., Samuelsen, G. S., and Holdeman, J. D., 2000. "Optimization of Jet Mixing into a Rich, Reacting Crossflow". *Journal of Propulsion and Power,* ***16***(5), Sept., pp. 729–735.

[68] Liscinsky, D., True, B., and Holdeman, J. D., 1993. "Experimental Investigation of Crossflow Jet Mixing in a Rectangular Duct". In 29th Joint Propulsion Conference and Exhibit.

[69] Liscinsky, D., True, B., and Holdeman, J. D., 1995. "Effects of Initial Conditions on a Single Jet in Crossflow". In 31st Joint Propulsion Conference and Exhibit, San Diego, CA, no. AIAA-95-2998.

[70] Liscinsky, D. S., and True, B., 1994. "Planar Mie Scattering Measurements of Scalar Mixing". In Laser Applications in Combustion and Combustion Diagnostics, Vol. 2122, International Society for Optics and Photonics, pp. 153–160.

[71] Liscinsky, D. S., True, B., and Holdeman, J. D., 1996. "Crossflow Mixing of Noncircular Jets". *Journal of Propulsion and Power,* ***12***(2), pp. 225–230.

[72] Mahesh, K., 2013. "The Interaction of Jets with Crossflow". *Annual Review of Fluid Mechanics,* ***45***, pp. 379–407.

[73] Margason, R. J., 1993. "Fifty Years of Jet in Cross Flow Research". In AGARD, Computational and Experimental Assessment of Jets in Cross Flow.

[74] Markides, C. N., and Mastorakos, E., 2005. "An Experimental Study of Hydrogen Autoignition in a Turbulent Co-Flow of Heated Air". *Proceedings of the Combustion Institute,* ***30***(1), pp. 883–891.

[75] Markides, C. N., and Mastorakos, E., 2011. "Experimental Investigation of the Effects of Turbulence and Mixing on Autoignition Chemistry". *Flow, Turbulence and Combustion,* ***86***, pp. 585–608.

[76] Mi, J., and Nathan, G. J., 2010. "Statistical Properties of Turbulent Free Jets Issuing From Nine Differently-Shaped Nozzles". *Flow, Turbulence and Combustion,* ***84***, pp. 583–606.

[77] Miller, J., and Bowman, C., 1989. "Mechanism and Modeling of Nitrogen Chemistry in Combustion". *Progress in Energy and Combustion Science,* ***15***(4), pp. 287–338.

[78] Muppidi, S., and Mahesh, K., 2007. "Direct Numerical Simulation of Round Turbulent Jets in Crossflow". *Journal of Fluid Mechanics,* ***574***, pp. 59–84.

[79] New, T. H., Lim, T. T., and Luo, S. C., 2003. "Elliptic Jets in Cross-Flow". *Journal of Fluid Mechanics,* ***494***, 10, pp. 119–140.

[80] Nori, V., and Seitzman, J., 2008. "Evaluation of Chemiluminescence as a Combustion Diagnostic under Varying Operating Conditions". In 46th AIAA Aerospace Sciences Meeting and Exhibit, Reno, NV, January, pp. 7–10.

[81] Norster, E. R., 1964. Second Report on Jet Penetration and Mixing Studies. Tech. Rep. PD/JP 2, The College of Aeronautics Cranfield.

[82] Papadopoulos, G., and Pitts, W. M., 1998. "Scaling the Near-Field Centerline Mixing Behavior of Axisymmetric Turbulent Jets". *AIAA Journal,* ***36***(9), pp. 1635–1642.

[83] Peters, N., 1986. "Laminar Flamelet Concepts in Turbulent Combustion". *21st (International) Symposium on Combustion*, pp. pp 1231 – 1250.

[84] Peters, N., 1994. Turbulente Brenngeschwindigkeit. Tech. rep., Abschlussbericht zum Forschungsvorhaben Pe 241/9-2.

[85] Peters, N., 2000. *Turbulent Combustion*. Cambridge University Press.

[86] Poinsot, T., and Veynante, D., 2005. *Theoretical and Numerical Combustion*. R. T. Edwards Incorporated.

[87] Pope, S. B., 2000. *Turbulent Flows*. Cambridge University Press.

[88] Pratte B. D., B. W. D., 1967. "Profiles of the Round Turbulent Jet in a Cross Flow". *Journal of the Hydraulics Division ASCE,* ***92***(-), pp. 53–64.

[89] Rajaratnam, N., 1976. *Turbulent Jets*. Elsevier.

[90] Ricou, F. P., and Spalding, D. B., 1961. "Measurements of Entrainment by Axisymmetrical Turbulent Jets". *Journal of Fluid Mechanics,* ***11***(1), pp. 21–32.

[91] Roberts, P. J., and Webster, D. R., 2002. "Turbulent Diffusion". *ASCE Press, Reston, Viginia*.

[92] Robinson, C., and Smith, D. B., 1984. "The Auto-Ignition Temperature of Methane". *Journal of Hazardous Materials,* ***8***(3), pp. 199 – 203.

[93] Ruck, B., 1990. "Einfluss der Tracerteilchengroesse auf die Signalinformation in der Laser-Doppler-Anemometrie". *Technisches Messen,* ***57***, pp. 284–295.

[94] Salewski, M., Stankovic, D., and Fuchs, L., 2008. "Mixing in Circular and Non-circular Jets in Crossflow". *Flow, Turbulence and Combustion,* ***80***(2), pp. 255–283.

[95] Sattelmayer, T., 2010. "Kapitel 9 Grundlagen der Verbrennung in stationären Gasturbinen". In *Stationäre Gasturbinen*, C. Lechner and J. Seume, eds. Springer Verlag, pp. 397–452.

[96] Sau, R., and Mahesh, K., 2008. "Dynamics and Mixing of Vortex Rings in Crossflow". *Journal of fluid Mechanics,* ***604***, pp. 389–409.

[97] Sautet, J., and Stepowski, D., 1994. "Single-Shot Laser Mie Scattering Measurements of the Scalar Profiles in the Near Field of Turbulent Jets with Variable Densities". *Experiments in Fluids,* ***16***, pp. 353–367.

[98] Schefer, R., and Dibble, R., 2001. "Mixture Fraction Field in a Turbulent Nonreacting Propane Jet". *AIAA Journal,* ***39***(1), pp. 64–72.

[99] Schlichting, H., 1982. *Grenzschicht-Theorie.* G. Braun, Karlsruhe.

[100] Schmid, H., 1995. "Ein Verbrennungsmodell zur Beschreibung der Wärmefreisetzung von vorgemischten turbulenten Flammen". PhD thesis, Universität Karlsruhe.

[101] Sforza, P. M., Steiger, M. H., and Trentacoste, N., 1966. "Studies on Three-Dimensional Viscous Jets". *AIAA Journal,* ***4***(5), pp. 800–806.

[102] Shan, J. W., and Dimotakis, P. E., 2006. "Reynolds-Number Effects and Anisotropy in Transverse-Jet Mixing". *Journal of Fluid Mechanics,* ***566***, pp. 47–96.

[103] Smith, G., Golden, D. M., Frenklach, M., Moriarty, N. W., Eiteneer, B., Goldenberg, M., Bowman, C. T., Hanson, R. K., Song, S., Gardiner Jr, W. C., et al., 1999. "GRI 3.0 Mechanism". *Gas Research Institute (http://www. me. berkeley. edu/gri_mech).*

[104] Smith, S. H., and Mungal, M. G., 1998. "Mixing, Structure and Scaling of the Jet in Crossflow". *Journal of Fluid Mechanics,* ***357***, pp. 83–122.

[105] Smyth, K. C., and Bryner, N. P., 1997. "Short-Duration Autoignition Temperature Measurements for Hydrocarbon Fuels Near Heated Metal Surfaces". *Combustion Science and Technology,* ***126***(1-6), pp. 225–253.

[106] Spadaccini, L. J., and Colket III, M. B., 1994. "Ignition Delay Characteristics of Methane Fuels". *Progress in Energy and Combustion Science,* ***20***, pp. 431–460.

[107] Squire, H. B., and Trouncer, J., 1944. Round Jets in a General Stream. Tech. Rep. ADB039248, Aeronautical Research Concil London.

[108] Stepowski, D., and Cabot, G., 1988. "Laser Mie Scattering Measurement of Mean Mixture Fraction Density and Temperature by Conditional Seeding in a Turbulent Diffusion Flame". *Symposium (International) on Combustion,* ***22***, pp. 619–625.

[109] Su, L. K., and Mungal, M. G., 2004. "Simultaneous Measurements of Scalar and Velocity Field Evolution in Turbulent Crossflowing Jets". *Journal of Fluid Mechanics,* ***513***, pp. 1–45.

[110] Sutton, O. G., 1932. "A Theory of Eddy Diffusion in the Atmosphere". *Proceedings of the Royal Society of London. Series A,* ***135***(826), pp. 143–165.

[111] SWM SERVICES GMBH, 2012. *Erdgasqualität im Verteilungsnetz des Grossraumes München.* http://www.swm.de/dms/swm/dokumente/schulen/downloads/erdgas-qualitaet.pdf, January.

[112] Tennekes, H., and Lumley, J. L., 1987. *A First Course in Turbulence*, 11 ed. MIT Press.

[113] Tollmien, W., 1926. "Berechnung Turbulenter Ausbreitungsvorgänge". *ZAMM-Journal of Applied Mathematics and Mechanics/Zeitschrift für Angewandte Mathematik und Mechanik,* ***6***(6), pp. 468–478.

[114] Toon, I., O'Dell, S., Currin, J., and Willis, J., 1994. Staged Gas Turbine Combustion Chamber with Counter Swirling Arrays of Radial Vanes having Interjacent Fuel Injection, June 14. US Patent 5,319,935.

[115] Turns, S. R., 2000. *An Introduction to Combustion.* McGraw-Hill, Boston.

[116] Venkataraman, K., Terry, J., Velkur, C., and Karim, H., 2014. Late Lean Injection Fuel Staging Configurations, Apr. 28. US Patent 8,707,707.

[117] Vogel, H., 1995. *Gerthsen Physik*, 18th ed. Springer Berlin.

[118] Voigt, P., 1999. "Entwicklung und Einsatz eines Laserlichtschnittverfahrens zur quantitativen Konzentrationsmessung bei Mischungsprozessen". PhD thesis, Institut für Antriebstechnik des DLR, Köln.

[119] Yuan, L. L., Street, R. L., and Ferziger, J. H., 1999. "Large-Eddy Simulations of a Round Jet in Crossflow". *Journal of Fluid Mechanics,* ***379***, pp. 71–104.

[120] Zaman, K. B., and Foss, J., 1997. "The Effect of Vortex Generators on a Jet in a Cross-Flow". *Physics of Fluids,* ***9***(1), pp. 106–114.